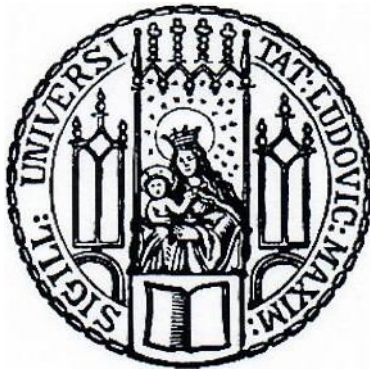

Optically Induced Forces on Anisotropic Plasmonic Nanoparticles

Christoph Maier



München 2020

Optically Induced Forces on Anisotropic Plasmonic Nanoparticles

Christoph Maier

Dissertation
an der Fakultät für Physik
der Ludwig-Maximilians-Universität
München

vorgelegt von
Christoph Matthias Maier
aus München

München, den 01. Februar 2020

Erstgutachter: PD Dr. Theobald Lohmüller

Zweitgutachter: Prof. Dr. Tim Liedl

Tag der mündlichen Prüfung: 07. Juli 2021

Kurzfassung

Die Verleihung des Nobelpreises für Physik im Jahr 2018 für Arthur Ashkins bahnbrechende Arbeit über optische Pinzetten hat dem Forschungsfeld der optischen Manipulation zu breiter Anerkennung verholfen. Im Laufe der letzten vier Jahrzehnte hat dieses Forschungsgebiet Anwendungen auf vielen Gebieten ermöglicht. Die Bandbreite erstreckt sich dabei von Einzelzellmikroskopie bis zu Nanolithographie. In jüngerer Vergangenheit war vor allem die Manipulation plasmonischer Nanopartikel von besonderem Interesse, da diese als optische Sensoren auf der Nanoskala verwendet werden können. Das genaue Verhalten derartiger Partikel ist jedoch ein komplexes Zusammenspiel vieler Parameter, die von der Geometrie und Beschaffenheit der Partikel und deren umgebendes Medium sowie der Laserstrahlung zur resonanten Anregung der plasmonischen Eigenschaften abhängen. Der Fokus dieser Arbeit liegt insbesondere auf nicht-sphärischen, also anisotropen, Goldnanopartikeln und dem Einfluss dieser Anisotropie auf die resultierenden optisch-induzierten Kräfte.

Zunächst wurden optische Streukräfte dazu benutzt, einzelne plasmonische Nanopartikel nach ihrer Form und damit auch ihrer Plasmonenresonanz zu sortieren, indem sie auf ein Substrat gedruckt wurden. Dabei wurde für jede Partikelspezies ein Laser verwendet, der resonant zur jeweiligen Plasmonenresonanz war. Dieser neuentwickelte Ansatz nutzt die Abhängigkeit der Plasmonenresonanz und damit auch der Streukräfte von der Form des Partikels aus. Als erste Anwendung wurde die Dynamik der Nanopartikelsynthese durch die Reduktion von Au(III) durch Natriumsulfid aufgeklärt, die Gegenstand einer langanhaltenden Debatte in der Literatur war. Es war möglich einen spektralen Peak im Nahinfrarotbereich der Bildung dreieckiger Nanopartikel zuzuschreiben, was im Gegensatz zu früheren Studien steht, die dies Kern-Schale Partikel oder Partikelaggregate zurückgeführt hatten.

Durch Erhöhung der Laserintensität nimmt plasmonisches Heizen derart zu, dass das Deformieren von Partikeln möglich wird. Normalerweise verformen sich anisotrope Partikel wie Nanostäbe zu sphärischen Partikeln um ihre Oberflächenenergie zu verringern. In dieser Arbeit wurde jedoch gezeigt, dass das Anlegen sehr starker Laserintensitäten zu einer Aufspaltung des Nanostäbchens in ein Dimer aus zwei sphärischen Nanopartikeln gleicher Größe führt. Mittels einer Analyse der optischen Eigenschaften konnte ein Partikelabstand im Subnanometerbereich abgeschätzt werden. Durch computergestützte Modellierung wurde ein Modell entwickelt, das die Aufspaltung einer Kombination von oberflächenspannungsinduzierter Deformation sowie inhomogen wirkender optischer und hydrodynamischer Kräfte zuschreibt. All diese Beiträge sind optisch induziert. Die Herstellung von Dimeren mit derart kleinen Partikelabständen ist üblicherweise herausfordernd. Daher kann dieser neu entwickelte Ansatz in Zukunft für Anwendungen wie oberflächenverstärkte Raman Streuung oder das induzieren chemischer Reaktionen mittels heißer Elektronen Bedeutung erlangen.

Dehnt man die Anisotropie der Partikel auf die Materialzusammensetzung aus, indem man plasmonisch-dielektrische Janus Nanopartikel erzeugt, tritt eine weitere Kraft unter Laserbestrahlung, Thermophorese, auf. Wird die Laserintensität erhöht wird dadurch der Partikel in vertikaler Richtung aus der optischen Ebene gedrückt. Im Rahmen dieser Dissertation wurde dieses Verhalten zum ersten Mal für Nanopartikel berichtet. Dies wurde angewandt, um DNS-funktionalisierte Janus Nanopartikel auf lebende Zellen zu heben und anschließend durch die Zellmembran zu injizieren. Es wurde gezeigt, dass die DNS diesen Vorgang übersteht, da die Wärme ausschließlich an der plasmonischen Spitze des Partikels erzeugt wird. Dies bereitet den Weg für biotechnische Anwendungen wie Zelltransfektion.

Diese Arbeit trägt zu einem besseren Verständnis der Vielzahl an Kräften bei, die auf plasmonische Nanopartikel in einem fokussierten Laserstrahl wirken. Insgesamt konnten für alle Grundlagenexperimente potentielle Anwendungen gezeigt werden, was das große Potential dieses Forschungsfeldes für zukünftige Technologien demonstriert.

Abstract

With the award of the noble prize in physics in 2018 for Arthur Ashkin's seminal work on optical tweezers, great honor has been brought to the field of optical manipulation. Over the past four decades, this field has developed applications in numerous fields ranging from single cell microscopy to nanolithography. Recently, the manipulation of plasmonic nanoparticles has been the subject of particular interest, since they offer an all optical handle at the nanoscale. However, the exact behavior of such particles is a complex interplay of many parameters of the the incident laser light, the particle itself and its surrounding. This thesis puts its focus especially on nonspherical, hence anisotropic, gold nanoparticles and the impact of this anisotropism on the optically induced forces.

First, optical scattering forces were used to sort single plasmonic nanoparticles according to their shape and therefore plasmon resonance by printing them on a substrate using a laser tuned to this particular resonance. This newly developed approach makes use of the shape dependence of the plasmon resonance and therefore the optical force exerted on the particles. It was first applied to shed light on the temporal dynamics of the nanoparticle synthesis via the reduction of Au(III) with sodium sulfide that has been a longstanding matter of debate. It was possible to assign a spectral near infrared peak to the formation of triangular nanoparticles, which is in contrast to previous reports that claimed core-shell particles or particle clusters.

When increasing the incident laser intensity, plasmonic heating contributes in a way that particle deformation becomes possible. Anisotropic particles such as nanorods usually converge to spherical particles upon heating to decrease surface energy. However, here it was found that applying very strong laser power densities on single gold nanorods lead to a split-up of the particle and the formation of a dimer consisting of two equally sized spheres. Optical analysis revealed the particles to have subnanometer gap distances. A model was conceived through computational modelling attributing the split-up to a combination of surface tension driven deformation, inhomogeneous optical forces and hydrodynamic forces. All those forces are in the end optically induced. Dimers with such small gap distances are usually challenging to produce. Therefore, this newly developed approach could be important for applications such as surface enhanced Raman scattering or hot electron driven chemical reactions.

Upon extending the anisotropy of the particles to their material composition thus creating plasmonic dielectric Janus nanoparticles, another force, namely thermophoresis, occurs when increasing the laser intensity thus pushing the particle out of the focal plane in vertical direction. Here, this behavior was found for the first time for a particle on the nanoscale. This was applied by lifting DNA functionalized Janus nanoparticles on top of living cells and injecting them through the cell membrane. It was shown that the DNA survives this treatment as the heat generation is concentrated at the plasmonic side of the particle, thus paving the way for biotechnical applications such as transfection.

This work helps to further understand the multitude of forces acting on plasmonic nanoparticles when subject to a focused laser beam. Overall, all fundamental experiments could be brought to applications, hence showcasing the great potential of the field for future technology.

List of Publications

Scientific publications presented in this work

- **Optical and Thermophoretic Control of Janus Nanoparticle Injection into Living Cells**
C. M. Maier, M. A. Huergo, S. Milosevic, C. Pernpeintner, M. Li, D. P. Singh, D. Walker, P. Fischer, J. Feldmann, T. Lohmüller*, *Nano Letters* 18 (12), 7935–7941 (2018)
DOI: 10.1021/acs.nanolett.8bo3885
- **Optical Nanoparticle Sorting Elucidates Synthesis of Plasmonic Nanotriangles**
M.A. Huergo# *, C. M. Maier#, M. F. Castez, C. Vericat, S. Nedev, R. C. Salvarezza, A. S. Urban*, and J. Feldmann, *ACS Nano* 10 (3), 3614-3621 (2016)
DOI: 10.1021/acs.nano.5bo8095
- **Splitting Gold Nanorods with Light**
C. M. Maier, F. Schuknecht, V. Hintermayr, T. Lohmüller*, *in preparation*

Additional publications in the course of this thesis

- **Optofluidic Transport and Manipulation of Plasmonic Nanoparticles by Thermocapillary Convection**
F. Winterer, C. M. Maier, C. Pernpeintner, T. Lohmüller*, *Soft Matter* 14, 628-634 (2018)
DOI: 10.1039/C7SM01863K
- **New Insight into the Chemical Nature of the Plasmonic Nanostructures Synthesized by the Reduction of Au (III) with Sulfide Species**
M. A. Huergo, L. Giovanetti, M. S. Moreno, C. M. Maier, F. G. Requejo, R. C. Salvarezza, C. Vericat*, *Langmuir* 33 (27), 6785-6793 (2017)
DOI: 10.1021/acs.langmuir.7bo1168

- **Reversible Plasmon Tuning of Individual Gold Nanoparticles Using Plasmonic Heating**

J. Lenz, C. M. Maier, T. Lohmüller*, J. Feldmann, *in preparation*

- **Internal Grain Boundary Plasmon Dephasing at optically Bent Gold Nanorods**

F. Schuknecht, C.M. Maier, M. Döblinger, T. Lohmüller*, *in preparation*

– equal contributions; * – corresponding author

Contributions to workshops and conferences

- **Nanolithography by optothermal manipulation of gold nanoparticles**

Christoph M. Maier, Michael Fedoruk, Marco Meixner, Sol Carretero-Palacios, Theobald Lohmüller, Jochen Feldmann

Nanosciences: Great Adventures on Small Scales, Venice, 2013

- **Nanolithography by optothermal manipulation of gold nanoparticles**

Christoph M. Maier

Workshop on Photonics and Optoelectronics, Riezlern, September 2014.

- **Optical nanoparticle sorting elucidates synthesis of plasmonic nanotriangles**

Christoph M. Maier, María A. Huergo, Marcos F. Castez, Carolina Vericat, Spas Nedev, Roberto C. Salvarezza, Alexander S. Urban, Jochen Feldmann

DPG spring meeting, Regensburg, March 2016.

- **Manipulation of Gold Nanoparticles with thermal forces**

Christoph M. Maier

Photonics and Optoelectronics with New Materials, Lenggries, July 2016.

- **Optothermal manipulation of gold nanostructures**

Christoph M. Maier

Photonics and Optoelectronics with New Materials, Syracuse/Sicily, March 2017.

- **Bending and Splitting Gold Nanorods with Light**

Christoph M. Maier, Anastasia Babynina, Verena Hintermayr, Theobald Lohmüller

Material Research Society (MRS) Fall Meeting, Boston, USA, December 2017.

Contents

Abstract	III
1 Introduction: Optical manipulation of nanoparticles in nanotechnology	1
2 Fundamentals: Optical and thermal properties of plasmonic nanoparticles	5
2.1 Optical forces on gold nanoparticles	6
2.1.1 The particle plasmon	6
2.1.2 Optical forces on plasmonic nanoparticles	11
2.1.3 Optically induced drag forces	14
2.2 Anisotropic plasmonic particles	15
2.3 Optical properties of gold nanoparticle dimers	18
2.4 Plasmonic heating	22
2.5 Melting of gold nanorods	24
2.6 Optically induced thermophoresis of plasmonic Janus particles	25
3 Methods: From microscopy over numerical modeling to cell culture	33
3.1 Nanoparticle characterization and manipulation	34
3.1.1 Dark field microscopy and laser manipulation	34
3.1.2 Epifluorescence microscopy	36
3.1.3 UV-Vis spectroscopy	37
3.1.4 Scanning electron microscopy	37
3.2 Numerical modeling	39
3.2.1 Electrodynamic calculations with the finite-difference time-domain method	40
3.2.2 Calculation of optical forces and load	42
3.2.3 Simulations of heat transport and hydrodynamic forces	47
3.3 Cell culture and fixation	49

4	Spectral sorting of single plasmonic nanoparticles using optical forces	51
4.1	Context: The Reduction of Au (III) with sulfide species	52
4.2	Properties of the synthesis	53
4.3	Strategy: Use optical force to sort particles by their plasmon resonance . . .	55
4.4	Optical and numerical analysis	59
5	Laser induced splitting of single gold nanorods into plasmonic dimers	69
5.1	Context: Fabrication methods and applications of plasmonic dimers	70
5.2	Optical splitting of gold nanorods into dimers and their optical properties .	70
5.3	Why do gold nanorods split?	75
6	DNA delivery into cells using optical and thermophoretic forces on Janus nanopens	83
6.1	Context: Gold nanoparticles for biotechnological applications	84
6.2	Optical properties of Janus nanopens	86
6.3	Moving JNPs within an optical trap by plasmonic heating induced ther- mophoresis	92
6.4	JNPs as carriers for the optical injection of biomolecules into cells	96
7	Conclusion: Applying forces on anisotropic plasmonic nanoparticles for nanotech- nological applications	105
	Bibliography	109
	Acknowledgments	125

Chapter I

Introduction: Optical manipulation of nanoparticles in nanotechnology

Within the last decades, using light as a tool for manipulation on the micro- and nanoscale has become increasingly popular, a development that culminated very recently in the winter of 2018, when Arthur Ashkin was awarded the Nobel Prize in Physics for his seminal work starting in 1970 that led to the invention of optical tweezers.^{1,2,3} Here, the momentum transfer from deflected photons leads to colloidal particles being pulled to the zone of higher light intensity. Hence, if an intensity distribution exhibits a local maximum, like in a focused laser beam, particles can be trapped in this region. This enables the facile manipulation of a variety of dielectric objects, such as viruses or bacteria and paved the way for numerous studies on single objects.⁴

Svoboda and Block extended the applicability of optical tweezers to plasmonic nanoparticles in 1994 reporting for the first time trapping of these nanoparticles by using a laser far redshifted from the plasmon resonance.⁵ In contrast to dielectric nanoparticles that are too small to strongly interact with light on a single particle basis, plasmonic nanoparticles are extremely susceptible to electromagnetic irradiation in the visible regime. They owe this behavior to the occurrence of so-called *particle plasmons*, *i.e.* collective charge oscillations at the surface of the particles that act as dipole antennas. In contrast to dielectric particles, where the wavelength of an incident laser does not influence the nature of the force field around the particle, plasmonic particles can either experience attractive or repulsive forces, depending on whether the incident laser is redshifted from the plasmon resonance or tuned to it. This yields a powerful handle to manipulate nanoparticles in a purely optical way.⁶

At the same time plasmonic particles are furthermore subject to strong plasmonic heating which can be harnessed for numerous applications, such as nanolithography⁷ or cell injection.⁸ This is of particular interest in the case of plasmonic-dielectric hybrid particles, so called

Janus particles. Here, the emerging temperature gradient leads to an additional force, namely thermophoresis.^{9,10,11}

In general, adding anisotropy to a system results in additional experimental degrees of freedom. Exploiting and exploring the forces resulting from this additional complexity will be the focal point of this thesis, as the shape and composition of plasmonic particles has a strong influence on their optical and thermal properties.

This thesis is structured as follows. In Chapter 2, the theoretical principles of the conducted experiments are given. In particular, the optical and thermal properties of plasmonic nanoparticles are discussed. First and foremost, particle plasmons that are the physical origin of optical forces in the case of noble metal nanoparticles are introduced. Since nanoparticles are immersed in water during the optical experiments, their hydrodynamic interaction is discussed at this point as well. The influences of shape and electrodynamic coupling of the particles are presented in the following sections. Plasmonic heating that stems from the incoherent plasmon decay, is introduced subsequently. This effect can lead to melting of nanoparticles, which is discussed in particular for nanorods. As mentioned above, anisotropy with regards to the material composition can lead to the particles becoming subject to thermophoresis, where a comprehensive summary is given.

Chapter 3 presents the microscopic and spectroscopic methods relevant for these studies, as well as the modeling techniques used for the interpretation of the experimental observations. Furthermore, the protocols for cell growth and fixation are given.

In Chapter 4 it will be shown how optical forces can be used to sort differently shaped plasmonic particles by their plasmon resonance. In particular, this approach is applied to elucidate the origin of a near-infrared (NIR) peak in the extinction spectrum of a particular nanoparticle synthesis, which has been the matter of a longstanding debate. By printing particles of a particular resonance on a substrate, their geometrical shape was determined to be triangular. Additionally, using computational modeling, all properties of the synthesis were successfully explained with the occurrence of triangular shaped particles.

Chapter 5 turns its focus on another anisotropic geometry, namely gold nanorods. Also here, the nanoparticles are printed onto a substrate using the repulsive radiation pressure of a laser energy matching the plasmon resonance of the particle. Interestingly, a splitting of the nanorods into dimers consisting out of two equally sized spheres separated by a sub-nanometer gap is observed. This means that additional forces have to be involved in this process. In particular, a model attributing this behavior to a combination of hydrodynamic drag, inhomogeneous optical forces and surface tension driven deformation of the nanorod is devised. Splitting up a single particle is an entirely new approach for the creation of dimers, a task that is usually quite challenging.

In Chapter 6 the anisotropy of the particle is not restricted to the morphology anymore but extended to the material composition. A new material, namely Janus nanoparticles or nanopens with a plasmonic gold tip and a dielectric alumina shaft, is introduced. When manipulated with optical tweezers, the enhanced absorption of the plasmonic tip leads to the occurrence of a temperature gradient and hence a thermophoretic force. This allows to lift particles over three-dimensional obstacles such as living cells. This elevator effect is reported for the first time for a particle on the nanoscale here. Furthermore, the inhomogeneous heating of the particle is exploited, using the Janus nanoparticles as a biomolecular shuttle by injecting DNA functionalized nanopens into living cells. Since the dielectric end of the particle is not subject to strong heating, the DNA molecules survive this treatment.

To emphasize the relevancy of the findings of this thesis, each results chapter starts with a short overview about the state of research in literature. At the end of each these chapters, a short summary is given as a bridge to the current state of research. Chapter 7 summarizes the main findings of this thesis and gives an outlook for potential future developments and applications based on the presented results.

Chapter 2

Fundamentals: Optical and thermal properties of plasmonic nanoparticles

The forces that act on plasmonic nanoparticles, and on which the focus of this thesis lies originate in their distinct optical and thermal properties. Hence, this chapter starts with an introduction to particle plasmons whose distinct physical effects form the basis for all the observations described within this thesis. Moreover, the influence of anisotropy and plasmonic coupling effects on the optical properties are discussed. Furthermore, irradiating gold nanoparticles with visible light also leads to strong plasmonic heating, which initiates various effects that have also been subject of investigation during this work. On the one hand it can lead to the melting of particles and on the other hand to the formation of a temperature gradient and a consequential thermophoretic force.

2.1 Optical forces on gold nanoparticles

The physical phenomena discussed within this thesis involve optical forces on and heating of gold nanoparticles *via* laser irradiation. The physical basis for the high susceptibility of noble metal nanoparticles to light is the occurrence of collective electron excitations within the particle called particle plasmons. This section gives a short introduction on plasmons in noble metal nanoparticles and their connection to optical forces. Since plasmonic nanoparticles are typically immersed in fluidic solutions, also hydrodynamic forces from the surrounding need to be considered.

2.1.1 The particle plasmon

In a simplistic picture, particle plasmons are standing waves of conduction band electrons confined by the physical dimensions of the nanoparticle. Hence, in order to understand the interaction of plasmonic nanoparticles with light, one has to understand the motion of these electrons when driven by an external electromagnetic field. The response of electrons to an external field can be described by the displacement field $D(\omega)$, which in turn can be expressed through the total field $E(\omega)$ and the frequency dependent dielectric function $\varepsilon(\omega)$:¹²

$$D(\omega) = \varepsilon(\omega)E(\omega) \quad (2.1)$$

For a bulk material with negligible surface effects, the dielectric function provides all the necessary input to describe the electron motion. In a noble metal like gold, $\varepsilon(\omega)$ is dominated by the conduction band electrons, which leads to very low damping of the electron motion. In the most simple model, the classical *Drude*-model, electrons are described as an ideal gas. The equation of motion of an electron is given by:¹²

$$m_{\text{eff}} \frac{\partial^2 \mathbf{x}}{\partial t^2} = -\frac{m_{\text{eff}}}{\tau} \frac{\partial \mathbf{x}}{\partial t} - eE_{\text{tot}}(t) \quad (2.2)$$

Here, e and m_{eff} are the electron charge and effective mass. The characteristic scattering time τ of the electrons is introduced to account for macroscopic electron scattering. The incident electromagnetic field $E_{\text{tot}}(t) = E_0 e^{-i\omega t}$ leads to a displacement of the electrons oscillating with the same frequency ω . Using the Ansatz $\mathbf{x}(t) = \mathbf{x}_0 E_0 E(t)$, one obtains:

$$\mathbf{x}(\omega) = \frac{eE_{\text{tot}}(\omega)}{m_{\text{eff}}(\omega^2 + i\omega/\tau)} \quad (2.3)$$

Macroscopically, the collective displacement of conduction band electrons induces a polarization $P(\omega) = -e\mathbf{x}(\omega)n$, with n being the electron density in the conduction band. The

displacement field $D(\omega)$ can be written in terms of the polarization:

$$D(\omega) = \varepsilon(\omega)E_{\text{tot}}(\omega) \equiv \varepsilon_0(\omega)E_{\text{tot}}(\omega) + P(\omega). \quad (2.4)$$

From Equation 2.3 one can derive the dielectric function:

$$\varepsilon(\omega) = \varepsilon_0(\omega) \left(1 - \frac{\omega_p^2}{\omega^2 + i\omega\tau^{-1}} \right) = \varepsilon_0(\omega)\varepsilon_{\text{Drude}}(\omega), \quad (2.5)$$

with the vacuum permittivity ε_0 and the bulk plasmon frequency

$$\omega_p = \sqrt{\frac{ne^2}{\varepsilon_0 m_{\text{eff}}}}, \quad (2.6)$$

which was measured to be 8.45 eV for gold.¹³ However, this description does not yet take into account the positive ionic background from the metal lattice, since $\varepsilon_{\text{Drude}}(\omega)$ is just valid under the assumption of a free electron gas. To account for the positive ionic background, a background polarization term $P_\infty = \varepsilon_0(\varepsilon_\infty - 1)$ is added to Equation 2.4 with the background permittivity ε_∞ .¹⁴ This yields for the dielectric function:

$$\varepsilon(\omega) = \varepsilon_\infty - \frac{\omega_p^2}{\omega^2 + i\omega\tau^{-1}} \quad (2.7)$$

Figure 2.1 compares the dielectric function obtained from Equation 2.7 by fitting the parameters ε_∞ , ω_p and τ with measured data.¹⁵ One can see that for wavelengths below 800 nm, theory and experimental data diverge significantly. This is due to interband excitations from

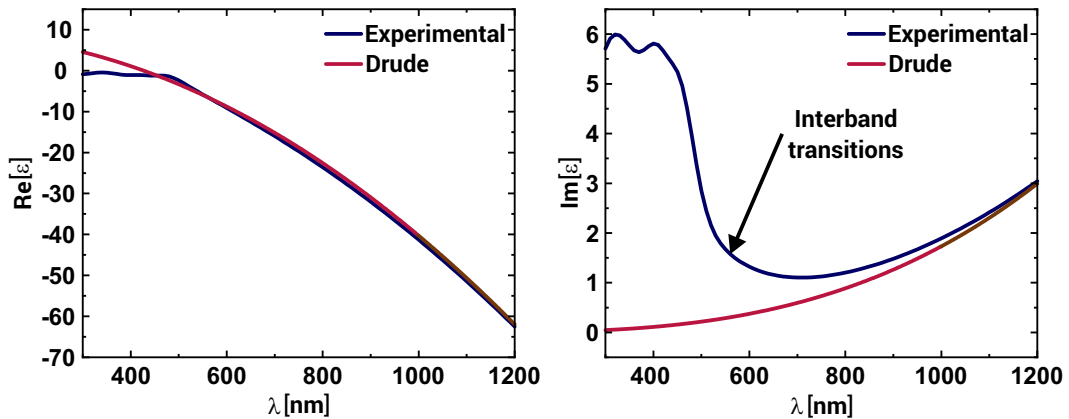


Figure 2.1 – Comparison of the dielectric function obtained from the free electron model (red) with experimentally measured values (blue) for monocrystalline gold.¹³ The fitting parameters for the free electron model are $\varepsilon_\infty = 9$, $\omega_p = 13.2$ PHz and $\tau = 15.1$ fs. Below 800 nm interband transitions lead to a deviation of the measured values from the free electron model.

the d-band into the sp-conduction band that start to occur here. The *Drude-Lorentz* model is an extension of the *Drude* model, correcting for interband transitions by empirically fitting Lorentzian-oscillator terms to the dielectric function.^{14,16} This yields an analytic model for the dielectric function of gold over the entire visible spectrum. For calculations though, it is more feasible to use interpolated or fitted measured data.^{15,13}

Up to this point all considerations still assume an infinite crystal, thus neglecting boundary effects. However, the properties of a plasmonic nanoparticle are dominated by the spatial confinement of the electron movement since the plasmon propagation is limited by the particle geometry and thus localized to the incident field, leading to a standing wave within the particle.

In the simplest case, the plasmon oscillation is confined in an isotropic spherical particles with a diameter much smaller than the incident wavelength. Here, the electromagnetic response can be approximated as a point shaped dipole, thus neglecting any variations of the incident field phase. Hence, in this so called *quasi-static approximation*, the incident plane wave is assumed to be a constant field, leading to a coherent excitation of the conduction band electrons. Analogous to radio antennas, gold nanoparticles can be considered as dipole antennas absorbing and emitting electromagnetic radiation.¹⁸ Like for an antenna, absorption and scattering of the incident wave greatly exceeds the physical dimensions of the particle (Figure 2.2).

The electric potential of a particle, with the dielectric function ε and radius R , located at the origin of a uniform static incident field $E_0 = E_0 \cdot e_z$, in a dielectric medium of permittivity

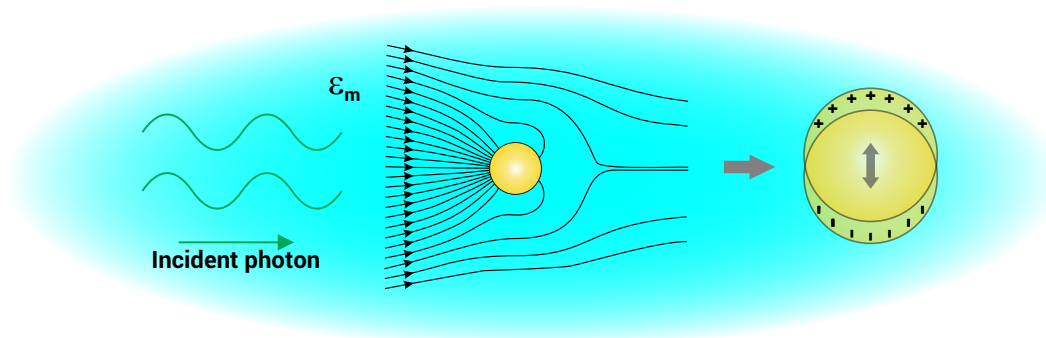


Figure 2.2 – Exposure of a gold nanoparticle to an electromagnetic field. An electromagnetic wave resonant to the plasmon is propagating towards a gold nanoparticle (left) and exciting a plasmon that leads to a polarization of the particle (right). This induces a strong electric field that redirects the Poynting vector of subsequent photons towards the particle (center). This leads to drastically enhanced interaction cross sections of plasmonic particles at resonance. The field lines of the Poynting vector were adapted from Bohren.¹⁷

ε_m , can be written in cylindrical coordinates in terms of Legendre polynomials $P_l(\theta)$:¹⁴

$$\Phi(r, \theta) = \begin{cases} \sum_{l=1}^{\infty} A_l r^l P_l(\cos(\theta)) & \text{for } r \leq R \quad := \Phi_{in}(r, \theta) \\ \sum_{l=0}^{\infty} [B_l r^l C_l r^{-(l+1)}] P_l(\cos(\theta)) - Er \cos(\theta) & \text{for } r \geq R \quad := \Phi_{ex}(r, \theta) \end{cases} \quad (2.8)$$

Imposing continuity at $r = R$ for the potential and the field then yields:¹⁴

$$\Phi_{in}(r, \theta) = -\frac{3\varepsilon_m}{\varepsilon + 2\varepsilon_m} E_0 r \cos(\theta), \quad (2.9)$$

$$\Phi_{ex}(r, \theta) = \underbrace{E_0 r \cos(\theta)}_{\text{Incident field}} + \underbrace{\frac{\varepsilon - \varepsilon_m}{\varepsilon + 2\varepsilon_m} E_0 R^3 \frac{\cos(\theta)}{r^2}}_{\text{Dipole contribution}}. \quad (2.10)$$

The external potential Φ_{ex} consists of a superposition of the incident field and a contribution of a dipole located at the center of the particle.¹⁴ Therefore, one can rewrite Equation 2.10 in terms of a dipolar moment \mathbf{p} :

$$\Phi_{ex}(r, \theta) = E_0 r \cos(\theta) + \frac{\mathbf{p} \cdot \mathbf{r}}{4\pi\varepsilon_0 + 2\varepsilon_m r^3}, \quad (2.11)$$

$$\mathbf{p} = 4\pi\varepsilon_0\varepsilon_m R^3 \frac{\varepsilon - \varepsilon_m}{\varepsilon + 2\varepsilon_m} \mathbf{E}_0.$$

Thus, a plasmonic nanoparticle acts like a dipole when exposed to an external field, since the field induces a dipole moment within the particle. The polarizability α , defined through $\mathbf{p} = \varepsilon_0\varepsilon_m\alpha\mathbf{E}_0$, then reads:

$$\alpha = 4\pi R^3 \frac{\varepsilon - \varepsilon_m}{\varepsilon + 2\varepsilon_m} \quad (2.12)$$

From Equation 2.12, the *Clausius-Mossotti* relation, one can deduce the wavelength dependent effects of plasmonic nanoparticles directly from the wavelength dependence of the dielectric function. Furthermore, Equation 2.12 reveals that α becomes maximal for $|\varepsilon + 2\varepsilon_m| \rightarrow 0$. For the case of negligible damping and thus $\text{Im}[\varepsilon] = 0$, the resonance condition can be written as:¹⁴

$$\text{Re}[\varepsilon] = -2\varepsilon_m \quad (2.13)$$

This relation is called the *Fröhlich condition*. Hence, the resonance of a point shaped spherical particle depends on the dielectric function of the material and the surrounding medium. From the complex polarizability in Equation 2.12, one can deduce a scattering and an absorption cross section that are defined by the ratio of scattered and absorbed power to the incident

intensity:

$$\sigma_{\text{scat}} = \frac{P_{\text{scat}}}{I_{\text{inc}}} = \frac{k^4}{6\pi} |\alpha^2|, \quad (2.14)$$

$$\sigma_{\text{abs}} = \sigma_{\text{ext}} - \sigma_{\text{scat}} = k\text{Im}[\alpha] - \sigma_{\text{scat}}. \quad (2.15)$$

The picture introduced up to this point serves well to understand the physical origin of particle plasmons. However, the particles are assumed to be point shaped here which is actually not the case and hence multipolar and retardation effects¹⁹ are neglected here. These effects already start to become relevant for particles as small as 10% of the incident wavelength in the surrounding medium λ_m .¹² Since the particle diameters discussed in this thesis are in the order of 100 nm, this is significant to take into account for. Due to the finiteness of the speed of light, inducing a charge on one side of the particle leads to a reaction on the other end of the particle with a phase delay of $4\pi R\lambda_m$.¹⁹ As a result, the resonance peak both redshifts and broadens with increasing particle size. Furthermore, multipolar modes become increasingly important for larger particles leading to further redshifting and broadening of the spectrum.¹⁹

An analytic solution for non-vanishingly small particles was given by Gustav Mie in 1908.²⁰ Briefly, the incident and scattered field are expanded into transversal magnetic and transversal electric fields, which can be solved in terms of Bessel and Hankel functions.¹² In the case of a homogeneous sphere, those functions are analytically solvable. For anisotropic geometries, which are the focal point of this thesis however, numerical approaches have to be applied to obtain scattering and absorption cross sections (cf. Section 3.2.1). By calculating scattering and extinction cross sections either through analytic Mie theory or numerically, one can then deduce the complex polarizability $\alpha(\omega) = \alpha'(\omega) + i\alpha''(\omega)$ from Equation 2.14

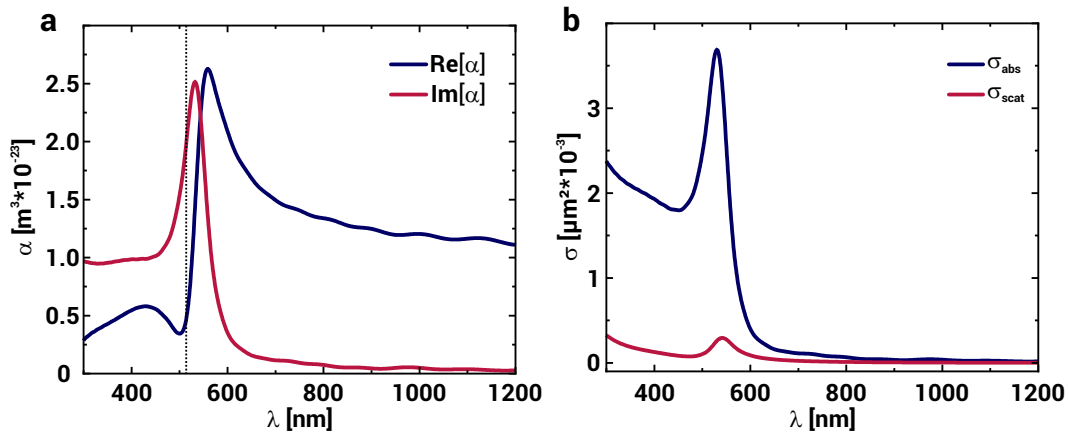


Figure 2.3 – Optical properties of spherical gold nanoparticles. (a) Polarizability of a 40 nm gold sphere in water using the cross sections obtained from FDTD calculus (b) with Equation 2.16 and the dielectric function from literature.¹³ The Fröhlich condition (Equation 2.13), which is met at 514 nm in water is marked as a dotted line.

and Equation 2.15 as:

$$\alpha' = \sqrt{\frac{\sigma_{\text{scat}} 6\pi}{k^4} - \frac{\sigma_{\text{scat}}^2}{k^2}}, \quad \alpha'' = \frac{\sigma_{\text{ext}}}{k} \quad (2.16)$$

Figure 2.3 shows the complex polarizability and the scattering and absorption cross sections for a spherical gold particle with a diameter of 80 nm. As one can see, the peak in the complex polarizability induces the peak in the cross sections, which in turn correspond to the particle plasmon resonance, typically observed in the visible for noble metal nanoparticles. It follows from Equation 2.12 and Equation 2.14 that $\sigma_{\text{scat}} \propto R^6$. This drastically increased interaction cross section with light (cf. Figure 2.2) is a necessity and fundamental for both imaging and manipulation (cf. Section 3.1.1) of plasmonic nanoparticles below the diffraction limit.

2.1.2 Optical forces on plasmonic nanoparticles

The basis for optical manipulation of nanoparticles is the momentum conservation of the incident photons interacting with nanoparticles. Literature distinguishes three size regimes to explain the fundamentals of optical forces.²¹ Atoms, molecules or very small particles with $R \ll \lambda$ can be described as point shaped dipoles as discussed before and span the so called *Rayleigh* regime. For particles larger than the incident wavelength, a very descriptive geometrical optics picture can be applied: A light ray entering a dielectric particle is refracted in a way that a momentum transfer pulls the particle to the region of higher intensity.³ Particles with sizes in between these, hence $R \approx \lambda$ are allocated to the *Mie* regime. As described before, Mie theory takes into account retardation and multipole effects, which are not considered in the Rayleigh regime. Those effects are represented in the polarizability (Equation 2.12), which can be obtained from Mie calculus or numerically. However, a dipolar approach can still be used to calculate optical forces for particles much larger than the dipolar limit by using the correct polarizability.²²

The classical approach to determine optical forces is based on the Lorentz force acting on a dipole, with a dipole moment $\mathbf{p} = q(\mathbf{r}_1 - \mathbf{r}_2)$. \mathbf{r}_1 and \mathbf{r}_2 are the respective position vectors of the opposing charges q . In this case, the Lorentz force reads:²³

$$\mathbf{F} = (\mathbf{p} \cdot \nabla)\mathbf{E} + \dot{\mathbf{p}} \times \mathbf{B} + \dot{\mathbf{r}} \times (\mathbf{p} \cdot \nabla)\mathbf{B}, \quad (2.17)$$

which in the time-averaged case simplifies to:²³

$$\langle \mathbf{F} \rangle = \sum_i \langle p_i(t) \nabla E_i(t) \rangle. \quad (2.18)$$

The manipulation experiments within this thesis were all performed with monochromatic lasers. Hence, the incident wave is represented by:

$$\mathbf{E}(\mathbf{r}, t) = \text{Re} [\mathbf{E}(\mathbf{r})e^{-i\omega t}], \quad (2.19)$$

$$\mathbf{B}(\mathbf{r}, t) = \text{Re} [\mathbf{B}(\mathbf{r})e^{-i\omega t}]$$

As introduced before, the dipole moment can be expressed as $\mathbf{p} = \alpha(\omega)\mathbf{E}(\mathbf{r})$ for a linear response. Thus, the average force over one optical period $T = 2\pi/\omega$ can be written in terms of the complex polarizability α :

$$\langle \mathbf{F} \rangle = \underbrace{\frac{\alpha'}{2} \sum_i \text{Re}[E_i^* \nabla E_i]}_{\langle \mathbf{F}_{\text{grad}} \rangle} + \underbrace{\frac{\alpha''}{2} \sum_i \text{Im}[E_i^* \nabla E_i]}_{\langle \mathbf{F}_{\text{scat}} \rangle} \quad (2.20)$$

Here, the two terms are identified as gradient and scattering force. In SI units they read:

$$\langle \mathbf{F}_{\text{grad}} \rangle = \frac{1}{4} \varepsilon_0 \varepsilon_m \alpha' \nabla (E * E) \quad (2.21)$$

$$\langle \mathbf{F}_{\text{scat}} \rangle = \frac{1}{2} \varepsilon_0 \varepsilon_m \alpha'' \text{Im} \left\{ \sum_j E_j^* \nabla E_j \right\} \quad (2.22)$$

The term *gradient force* originates from its proportionality to the intensity gradient. Hence, assuming a positive polarizability, it acts as an attractive force field towards the region of highest intensity, which coincides with the the laser focus. The term scattering force, albeit a little misleading since it also depends on absorption, stems from its proportionality to the scattering and absorption cross sections. In terms of the Poynting vector \mathbf{S} , it is given by:

$$\langle \mathbf{F}_{\text{scat}} \rangle = \frac{\varepsilon_m^2}{c} (\sigma_{\text{scat}} + \sigma_{\text{abs}}) \langle \mathbf{S} \rangle \quad (2.23)$$

This contribution corresponds to the direct momentum transfer from the photons to the particle by scattering and absorption. It is further always pointing in the direction of the Poynting vector and acts as a repulsive force field that pushes the particle out of the laser focus.

F_{grad} depends on the real part and F_{scat} on the imaginary part of the polarizability. Consequently the applied wavelength defines, whether an attractive or a repulsive force fields are generated on the metallic nanoparticle. Close to the plasmon resonance, where extinction has its maximum, repulsive scattering forces become dominant. Redshifted from the plasmon resonance, the real part of the complex polarizability outweighs the imaginary part as

illustrated in Figure 2.3a. Hence, attractive gradient forces dominate in this case. For the case of dielectric particles, gradient forces always dominate throughout the visible spectrum due to their negligible absorption. Focusing the laser beam with a microscope objective induces strong intensity gradients and thus gradient forces that overcome Brownian motion. This is the requirement for stable trapping of particles. Figure 2.4 compares the experimental outcome of resonant and off-resonant laser illumination with focused laser beams.

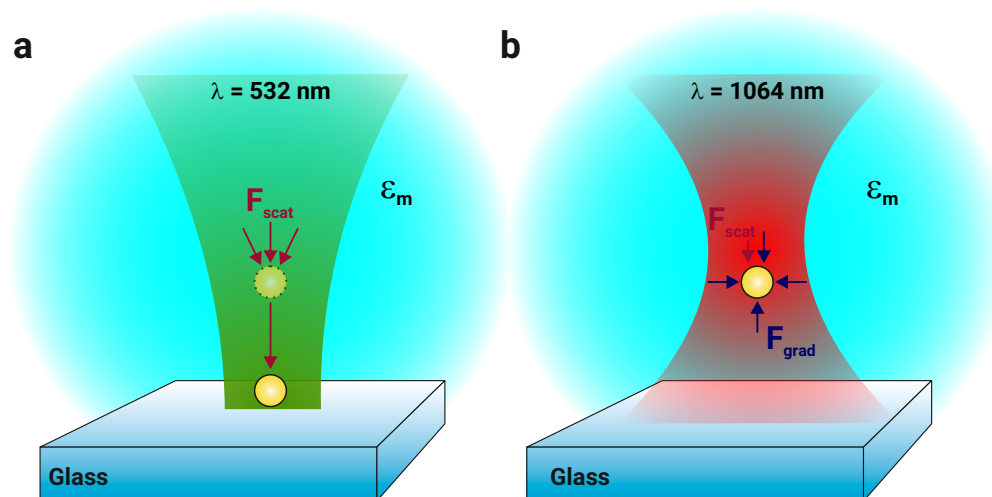


Figure 2.4 – Optical forces acting on a gold nanoparticle under laser irradiation close to the plasmon resonance (a) and redshifted from the resonance (b). Under resonant illumination (532 nm) the repulsive forces dominate and push the particles onto the substrate, which is referred to as printing. Redshifted from the plasmon resonance, the gradient forces dominate in a focused laser beam leading to a stable particle position, referred to as trapping. Due to the non-negligible scattering force, this position is slightly below the focal plane.

Applying optical forces for the manipulation of plasmonic particles - from theory to reality

Optical manipulation of colloidal objects has come a long way since optical tweezers have been first introduced by Ashkin *et al.* for dielectric beads, viruses and bacteria.^{2,24} Svoboda *et al.* were the first to optically tweeze spherical plasmonic nanoparticles showcasing their potential for nanoscience.⁵ This technique was subsequently extended for bigger and nonspherical particles.^{25,26} Since then, the chair where this particular thesis was conducted was at the forefront of nanoparticle tweezing with numerous studies including force measurements at the nanoscale^{27,28} among others.

Lately, also the repulsive scattering forces acting on plasmonic nanoparticles, when irradiated with a focused laser beam close to their plasmon resonance was exploited for nanostructuring below the diffractive limit. In particular, Urban *et al.* were the first to show the feasibility of this approach by *printing* plasmonic particles on a glass substrate at arbitrary positions with high precision using a tightly focused laser beam.^{29,30} Based on this work, a

combination of trapping and printing using two different lasers has been applied to align individual gold nanorods on a substrate.³¹

Again at this particular chair, it was shown that shape transformations in gold nanorods can be induced during the laser printing process,³² which was attributed to the inhomogeneity of the viscous drag. This work was picked up more recently, by Liaw *et al.*, who showed that also the inhomogeneity of the optical force contributes roughly at the same magnitude to the bending.³³ This stems from the fact that gold nanorods cannot be approximated anymore as a point shaped dipole, but the coupling of the internal electric field to the electromagnetic wave has to be resolved spatially. A more detailed description of this formalism is given in Section 3.2.2.

This thesis further extends the understanding and the applicability of optical printing of plasmonic nanoparticles. In Chapter 4 the spectral selectivity of optical printing is revealed by sorting particles by their shape and therefore plasmon resonance. Chapter 5 shows for the first time that optical forces can be used to induce a controlled breakup of a single gold nanorod into a dimer. These advances allow to elucidate the complex effects behind optical printing and nanoparticle reshaping. The latter experiment in particular is a complex interplay between optical forces and hydrodynamic effects between the particles and the surrounding medium that become significant at high photon flux.³²

2.1.3 Optically induced drag forces

It was shown by *Babynina et al.* that single nanorods could be controllably bent during the printing process, an effect they attributed to inhomogeneous drag the nanorod experiences. This emphasizes that the viscous drag acting on nanoparticles when propagating through water is of significant amplitude, especially when considering anisotropic particles. Therefore, when analyzing the breakup of nanorods which will be discussed in more detail in Chapter 5, drag forces play an even more critical role.

A gold nanoparticle is relatively big compared to the surrounding molecules and the applied forces during printing are several orders of magnitude larger compared to Brownian forces.^{29,32} Hence, microscopic models can be omitted and hydrodynamics have to be applied instead. In this regime, the theoretical foundation is given by the *Navier-Stokes* equation,³⁴ which for a viscous incompressible laminar fluid in the static case reads:

$$\underbrace{-\nabla p}_{\text{Pressure gradient}} + \underbrace{\mu(T)\nabla^2 \mathbf{u}}_{\text{Internal Stress}} + \underbrace{\rho(T)\mathbf{F}_{\text{ext}}}_{\text{External Force}} = \underbrace{\rho(T)}_{\text{Mass}} \underbrace{(\dot{\mathbf{u}} + (\mathbf{u} \cdot \nabla)\mathbf{u})}_{\text{Acceleration}} \quad (2.24)$$

Here, \mathbf{u} is the fluid velocity field, p the pressure and $\rho(T)$ and $\mu(T)$ the temperature dependent density and viscosity of the fluid, respectively. Essentially the *Navier-Stokes* equation depicts Newton's second law $\mathbf{F} = m \cdot \dot{\mathbf{u}}$. The force terms on the left hand side can be identified as the pressure gradient, the internal stress and the externally applied force. Solving this set of equations under the assumption of mass conservation ($\rho(T)\nabla \cdot (\mathbf{u}) = 0$), one obtains the pressure and velocity fields. For the case of optical printing, F_{ext} is the optical force pushing the particle through the liquid and thus the main input parameter, apart from the temperature of the nanoparticle and the material constants of water. To date, there is no analytic solution for the *Navier-Stokes* equation, which is in fact one of the seven *Millennium Prize Problems* of mathematics.³⁵ Therefore, numerical methods have to be used to solve hydrodynamic systems. The calculations in the realm of this thesis were carried out using the *Finite-element* method, implemented in COMSOL and will be described in detail in Section 3.2.3.

2.2 Anisotropic plasmonic particles

Up to now, the optical properties of solid spherical particles have been discussed as they are important to understand every more complex system. This thesis, places its focus on anisotropic plasmonic nanoparticles. Any anisotropy has a strong influence on the optical properties as it changes the main plasmon resonance as well and introduces a polarization dependency.

One of the simplest non-spherical geometries is an ellipsoid, where, in contrast to a sphere, the three radii a_1 , a_2 and a_3 corresponding to the coordinate axes are not of the same length anymore. Its shape is defined by:

$$\frac{x^2}{a_1^2} + \frac{y^2}{a_2^2} + \frac{z^2}{a_3^2} := 1. \quad (2.25)$$

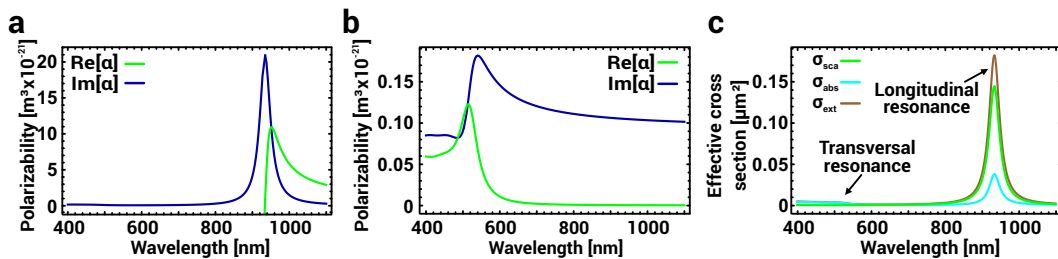


Figure 2.5 – Optical properties of a gold spheroid. Longitudinal (a) and transversal (b) polarizability of a gold spheroid with radii, $a_1 = 68.5$ nm, $a_2 = 12.5$ nm, $a_3 = 12.5$ nm as calculated from Equation 2.26. Since the polarizabilities have their maxima at different wavelengths, the total effective cross sections (c), calculated from Equation 2.14 and Equation 2.15, exhibit two resonances.

In analogy to Equation 2.12, one can derive an expression for the polarizability along a principal axis i :¹²

$$\alpha_i = 4\pi a_1 a_2 a_3 \frac{\varepsilon(\omega) - \varepsilon_m}{3\varepsilon_m + 3L_i(\varepsilon(\omega) - \varepsilon_m)}, \quad (2.26)$$

where L_i defines the degree of ellipticity satisfying the boundary condition $L_1 + L_2 + L_3 = 1$. It is defined by:¹²

$$L_i = \frac{a_1 a_2 a_3}{2} \int_0^\infty \frac{dq}{(a_i^2 + q)\sqrt{(q + a_1^2)(q + a_2^2)(q + a_3^2)}}. \quad (2.27)$$

A special case of ellipsoids are spheroids, in particular prolate spheroids, where $a_2 = a_3$ holds. One can follow from Equation 2.26 that the polarizability has two maxima, one along a_1 commonly referred to as longitudinal mode and another one along a_2 and a_3 commonly called transversal mode.

Solving Equation 2.26 for a gold spheroid, where $a_1 = 67.5$ nm and $a_{2,3} = 12.5$ nm, leads to the polarizability shown in Figure 2.5. While the transversal polarizability resembles the one of a spherical particle as shown in Figure 2.3, the spectral position of the longitudinal polarizability is redshifted. This characteristic becomes stronger for higher aspect ratios of spheroids.¹² The spheroid provides a good analytic approximation for gold nanorods like the ones used in Chapter 5. Their transversal and longitudinal resonances lie at similar spectral positions. However nanorods are made up of a cylinder with spherical end caps that makes an analytic solution impossible. In order to achieve exact solutions for the spectra of gold nanorods, numerical FDTD calculations are employed (cf. Section 3.2.1).

Rods or spheroids are not the only shapes that lead to a redshift away from the rigid sphere plasmon resonance. Essentially any shape diverging from the perfect sphere leads to a redshift,³⁶ due to charge accumulation at the extremes of the particle. In turn, this leads to a reduction of the plasmon driving restoring force, which reduces the resonance frequency.³⁷ Chemical synthesis has given access to a large variety of shapes for plasmonic nanoparticles such as shells,³⁸ stars,³⁹ cubes⁴⁰ or triangles⁴¹ providing systems with plasmon resonances far into the near infrared (NIR) region of the electromagnetic spectrum. For comparison, Figure 2.6 shows the charge distributions and scattering spectra of several differently shaped gold nanoparticles, namely a truncated nanotriangle, a nanorod, a nanoshell and a solid spherical gold nanoparticle. Albeit the first three have fundamentally different shapes, the scattering spectra that correspond to their appearances in the dark field microscope look fairly similar. All three particles exhibit a main plasmon peak at around 750 nm. In contrast, the solid spherical gold particle has a resonance at 550 nm. As one can see, the different shapes lead to an increase in charge density of around an order of magnitude compared to the nanosphere, which results in the redshift. When choosing their geometrical parameters appropriately (cf.

Figure 2.6), those three fundamentally differently shaped plasmonic particles exhibit the same spectrum. Therefore, a distinct assignment of spectral peaks to a certain particle species is challenging. Within this thesis it is shown for the first time how optical forces can be used to identify particle species within a polydisperse solution through wavelength selective optical printing and will be presented in detail in Chapter 4.

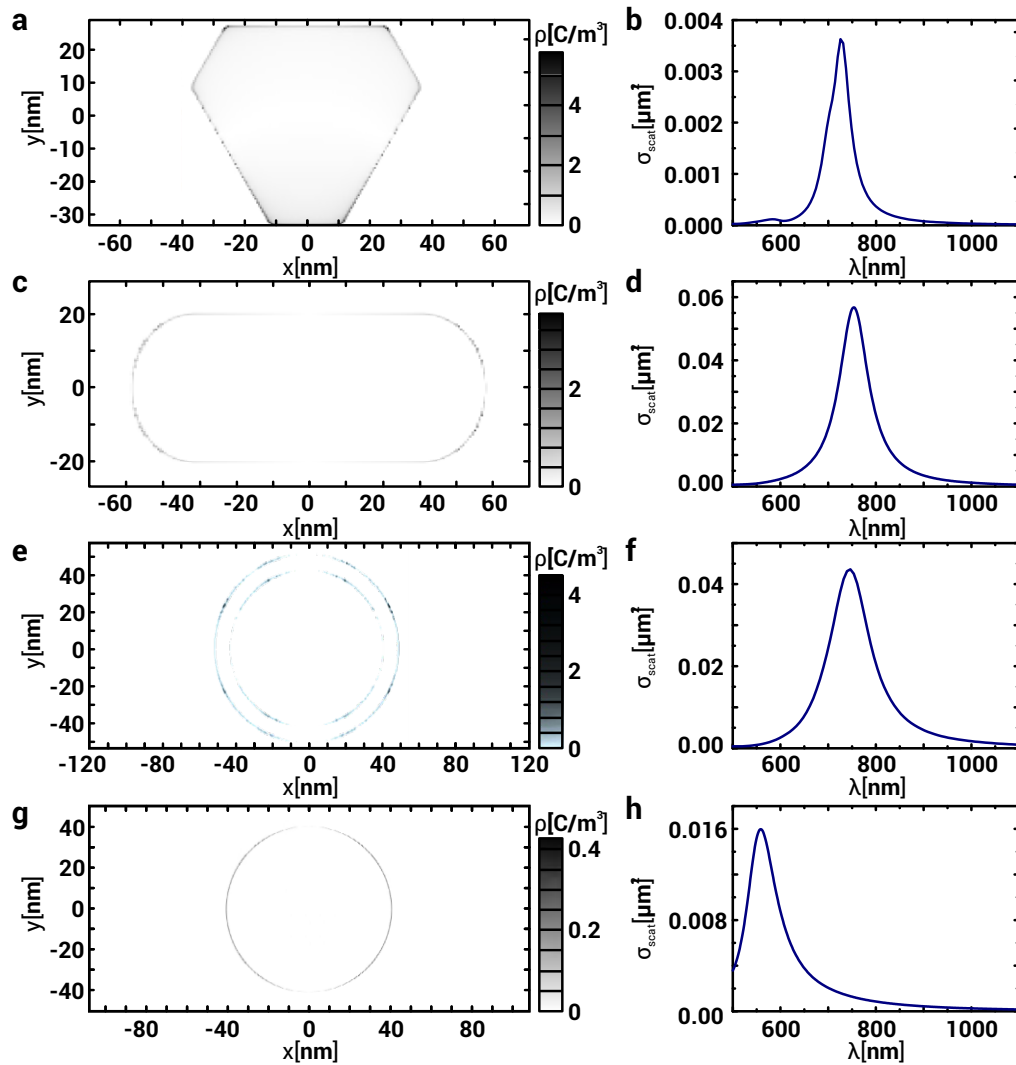


Figure 2.6 – Charge distribution at the plasmon resonance and scattering spectra of different plasmonic particles. (a, c, e, g) Charge distributions of a truncated nanotriangle, a nanorod, a core-shell nanoparticle and a solid nanosphere at their respective plasmon resonances. The material of all particles is gold. The core of the core-shell particle is silica. (b, d, f, h) Scattering cross section of the respective particles. The dimensions of the triangle, the nanorod and the core-shell particle were chosen to have their respective resonances at 750 nm. The solid spherical particle with its resonance at around 550 nm is shown for comparison. The charge density is much higher for the first three particles which leads to the redshift of the plasmon.

2.3 Optical properties of gold nanoparticle dimers

As described in Section 2.1, the dielectric surrounding of a plasmonic nanoparticle has a drastic influence on its optical properties. A very dramatic change of the dielectric environment is induced when placing two plasmonic structures in close proximity to each other. In this case, the plasmon modes can couple through the electric near fields leading to changes in the resonance as well as the occurrence of new modes.¹² In Chapter 5, the optical properties of dimers are used to estimate their separation distance. In the following a short introduction to coupling of plasmonic particles and their underlying physical principals is given.

Upon placing two plasmonic nanoparticles close enough to each other that their respective near fields overlap, the plasmon oscillations in both particles start to interact, thus changing the optical response of the structure. The simplest case for such a structure, commonly referred to as dimer, is made up of two rotationally symmetric particles, *i.e.* spheres or disks.

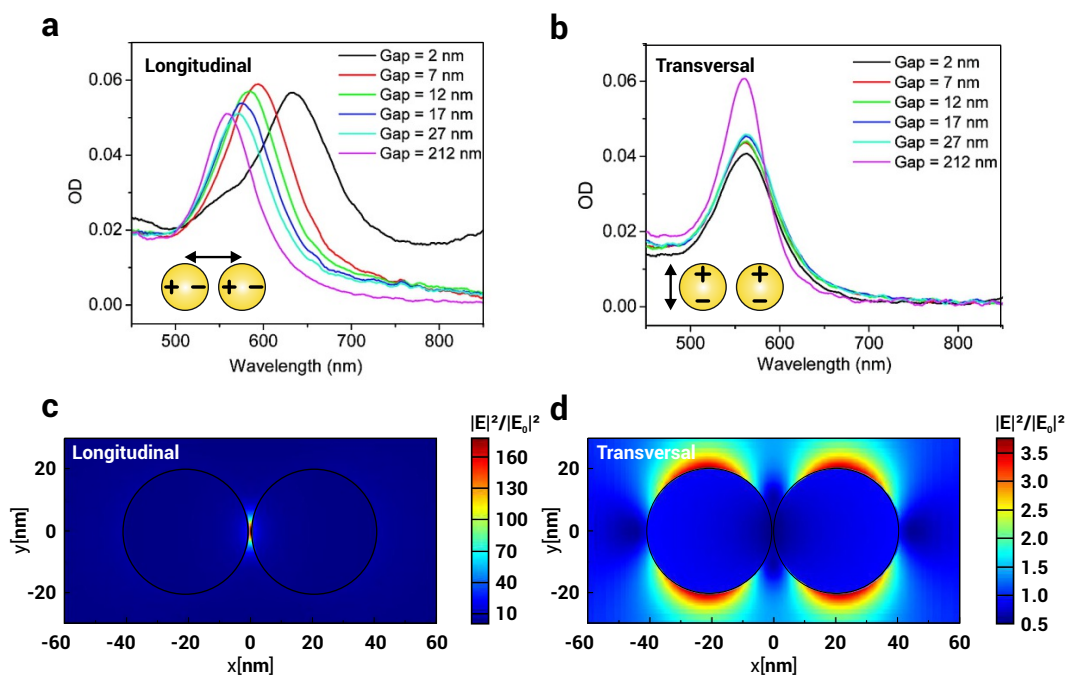


Figure 2.7 – Plasmonic coupling. Plasmon resonance of a nanodisk dimer with different gap distances for (a) longitudinal and (b) transversal excitation. E-field enhancement for a dimer of two 40 nm spheres with a gap of 10 nm for longitudinal (c) and transversal (d) excitation at their respective resonances. Whereas for longitudinal excitation, the peaks shift strongly to the red, under transversal illumination, only a small blueshift is observed. This can be explained when looking at the E-field enhancement. The amplitude of the scale bar of $|E|^2/|E_0|^2$ shows that strong coupling is observed under longitudinal excitation but almost none under transversal illumination. Figures a and b were adapted from Jain *et al.*⁴²

The second particle breaks the rotational symmetry of the first particle, which induces a polarization dependence to the system. A quantitative study of the influence of the interparticle distance has been performed by Jain *et al.* for the case of two gold nanodisks.⁴² Figure 2.7a

shows that upon longitudinal excitation, *i.e.* along the long axis, the plasmon resonance undergoes a major redshift with decreasing interparticle distance. However, when exciting transversally that is perpendicular to the long axis, only a mild blueshift occurs (Figure 2.7b). This can be explained by looking at the near field distributions for the respective polarizations. In the case of transversal excitation (Figure 2.7d), the electric near field has two maxima at the vertical edges of each particle. Hence, the fields do not overlap and therefore coupling is very weak. Consequently, the resonance position of a transversally excited dimer is nearly identical to the one of a single particle shifting only slightly to the blue. Upon longitudinal excitation, the near field is maximal in the gap region (Figure 2.7c). This leads to strong electromagnetic coupling and hence to the formation of a new mode redshifted from the original single particle resonance. The redshift can be fitted with a monoexponential function that depends on the gap distance making it possible to measure distances at the nanoscale.⁴²

When looking at the spectrum of the dimer with a 2 nm gap distance in Figure 2.7a, one notes a shoulder appearing at around 550 nm. This stems from the fact that once the electric field becomes strong enough, higher order modes become accessible leading to a hybridization of the plasmon.⁴³

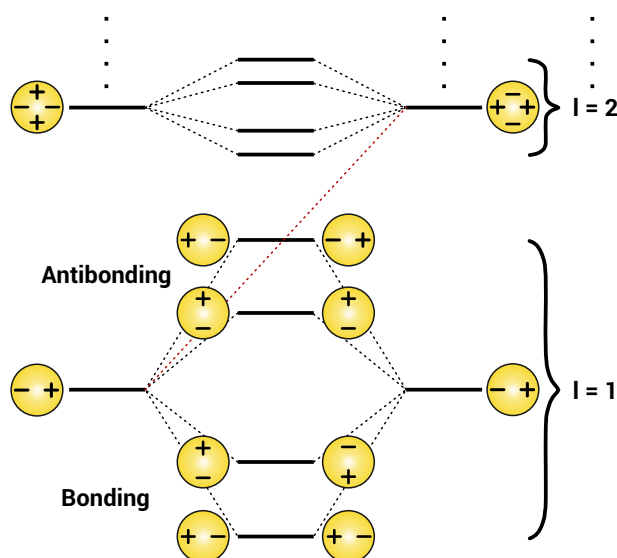


Figure 2.8 – Plasmon hybridization in dimers. When put into close proximity, the plasmon oscillations of two particles start to couple, forming a bonding and an antibonding mode for both longitudinal and transversal excitation. Since the dipole moment cancels out for the antibonding longitudinal and the bonding transversal mode, those modes are dark. For very small gap distances however, coupling to higher order modes leads to the hybridization of the plasmon.

In analogy to electronic orbitals in molecules, the fundamental modes are assigned to an orbital momentum number l with $l = 1$ being the fundamental dipolar excitation. Furthermore, both transversal and longitudinal modes form bonding and antibonding states (Figure 2.8). For the longitudinal mode, the dipole moments in the antibonding mode cancel out in case of two

equal particles. Hence, due to the lack of a dipole moment it is a so-called dark mode, which is not excited by light. The transversal excitation behaves differently, since here the dipole moments cancel out in the bonding mode and add up in the antibonding case.⁴³ Accordingly, the bright transversal mode is blueshifted from the uncoupled plasmon mode providing an explanation for both the redshift upon longitudinal coupling and the blueshift for transversal excitation, since the energetic spacing between the bonding and antibonding states increases with decreasing gap distances. The energy shift of the longitudinal mode is proportional to the gap distance D according to $1/D^3$ as to be expected for a pure dipole-dipole interaction according to the *Simpson-Peterson* approximation:^{44,45}

$$\Delta U = \frac{|\vec{\mu}|^2}{n^2 D^3} |\kappa| \quad (2.28)$$

Here, $\vec{\mu}$ is the transition dipole moment of the plasmon mode and n the refractive index of the surrounding medium. κ is an orientation factor defined as $\kappa = \cos(\theta_{12}) - 3 \cos(\theta_{1R}) \cos(\theta_{2D})$. θ_{12} is the angle between the dipole orientation in the first and the second particle. θ_{1D} and θ_{2D} are the angles between the dipole orientation in the first and second particle and the gap vector \mathbf{D} , respectively. However, for very small gap distances, the spectral shift deviates significantly from the $1/D^3$ dependence due to coupling of the $l = 1$ mode to higher order modes, which involves higher orders of $1/D$ that lead to a stronger redshift.⁴³ Additionally, the higher order modes can also couple to each other, leading to additional modes that lead to the spectral shoulder in Figure 2.7a. This second peak corresponds to the $l = 2 \leftrightarrow l = 2$ coupling of the two particle plasmons. For even smaller gaps, more peaks can be observed from higher order modes. In classical electrodynamics, the redshift as well as the number of observable modes would diverge for decreasing gap distances.

This picture of plasmon coupling is a local model, *i.e.* the interaction between the individual electrons is neglected and only a frequency dependent dielectric function is considered. Hence, the response of an electron only depends on the field applied at this particular point in space. This simplification is given up in more realistic nonlocal models. Here, the response also depends on the applied fields in the surrounding of an electron.¹² This contribution can be neglected in most cases since it is usually relatively weak. However, dimers with small gap distances show very strong charge accumulations in the gap region enhancing nonlocal effects.⁴⁷ Proper calculations that include nonlocal effects have been developed but remain very challenging.⁴⁸ For dimers, a simple rescaling approach has been reported to determine the correct position of the main plasmon peak of a dimer down to gap distances of 3.5 \AA by changing the classically calculated gap size with a correction factor,⁴⁹ which is applied to the calculations in Chapter 5.

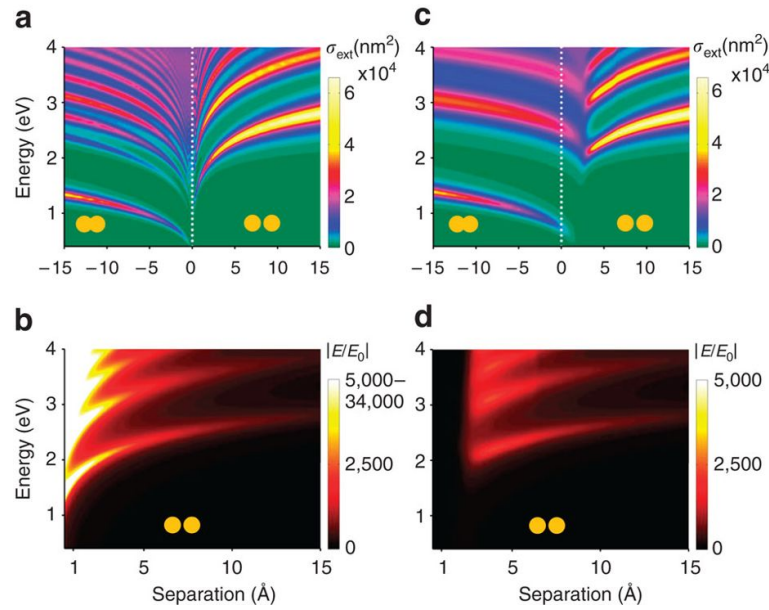


Figure 2.9 – Tunneling plasmonics. Calculation of the extinction (a,c) and the field enhancement (c,d) of dimers using both classical Maxwell calculus (a,b) as well as taking into account tunneling effects (c,d). Classical Maxwell calculus diverges for very small gap sizes leading to a discontinuity at 0 nm gap distance. This unphysical behavior disappears once quantum tunneling of electrons through the gap is taken into account. The two solutions start to diverge for gaps below 3.5 Å thus marking the border of the quantum tunneling regime. Figure adapted from Esteban *et al.*⁴⁶

When considering dimers with even smaller gaps, the E-fields become so strong that electrons can tunnel through the gap between the particles, which strongly alters the plasmon modes. This field of quantum plasmonics has reached considerable attention recently, as methods have been developed to create such small cavities.^{50,51} The tunneling effects can be modeled by introducing a spatially dependent conductivity in the gap region.^{46,52} Conduction through the gap region has a fundamental effect on the optical properties of a plasmonic dimer. The finite level of isolation between the particles does not permit infinite electric fields as expected using classical Maxwell calculus. Figure 2.9a shows the classical calculation of the extinction spectrum for a dimer consisting of two spherical gold nanoparticles of 40 nm in vacuum. In this case, the redshift of the plasmon resonance diverges when approaching a gap size of $d = 0$ Å. Progressively, more and more higher order modes gain sufficient intensity to become discernible. At $d = 0$ Å there is a discontinuity hinting to an unphysical behavior in the classical picture. Also the electric field enhancement reaches extremely high values (Figure 2.9b). By including tunneling effects, a realistic picture can be reestablished at these scales. The tunneling conductivity can be obtained using static scanning tunneling microscopy theory.⁵³ The extinction cross sections received here (Figure 2.9c), differ significantly from the classical calculations for gap distances below 3.5 Å. Here, the coupled plasmon modes start to disappear and new modes appear. Moreover, the field enhancement in the gap is much

lower than calculated classically (Figure 2.9d) since the tunneling significantly reduces the possible charge separation. Furthermore, the intensity difference of the peak between the plasmon modes becomes smaller when considering tunneling, as the effects scales with the resonance intensity.

2.4 Plasmonic heating

The scattering force used for optical printing depends linearly on both absorption and scattering cross section of the plasmonic particles. Since they are inherent properties of the particles, absorption of light cannot be avoided, thus leading to significant heating. Due to their enhanced interaction cross sections under resonant laser illumination, plasmonic particles are very efficient nanoscopic heat sources.⁵⁴ Even in the regime of optical trapping, where off-resonant laser irradiation is used, heat generation is not negligible.²⁷ This process, commonly referred to as plasmonic heating, stems from the incoherent plasmon decay.

A particle plasmon can decay either radiatively through re-emission of a photon or non-radiatively by creating electron-hole pairs, thus losing coherence. The radiative decay happens within tens of femtoseconds through emission of a photon with the same energy⁵⁵ and all electrons contributing to the plasmon oscillation lose their energy collectively. However, the individual electrons of the plasmon can also individually scatter with other electrons, the lattice or defects. This leads to a loss of the phase relationship of the plasmon electrons within around 20 fs,⁵⁶ which then thermalize to a *Fermi-Dirac* distribution in about 1 ps^{57,58} making a decay into a photon impossible. Subsequently, the high energy electrons lose their energy through coupling with interband transitions and scattering with phonons and other electrons.¹² Thus, lattice and electrons reach thermal equilibrium within picoseconds^{59,60,61} meaning the nanoparticle heats up. Figure 2.10 depicts an overview of the processes involved in the non-radiative decay. The local heating power density within the nanoparticle depends on the local electric field, which is highest in the middle of the nanoparticle.⁶² However, due to the high thermal conductivity of gold, gold nanoparticles were assumed to be homogeneous sources of heat for the temperature calculations throughout this thesis.

After the heat power density reaches equilibrium, the temperature equilibrates with the surrounding medium within less than a nanosecond.⁶³ Since convective contributions to the heat transport are negligible⁶⁴ the classical heat transfer equation can be applied:⁵⁴

$$\rho(\mathbf{r})c(\mathbf{r})\frac{\partial T(\mathbf{r}, t)}{\partial t} = \nabla k(\mathbf{r})\nabla T(\mathbf{r}, t) + Q(\mathbf{r}, t). \quad (2.29)$$

Here, \mathbf{r} and t are the spatial coordinate and time, $T(\mathbf{r}, t)$ the local temperature and $\rho(\mathbf{r})$, $c(\mathbf{r})$ and $k(\mathbf{r})$ the local temperature dependent material parameters mass density, specific heat and

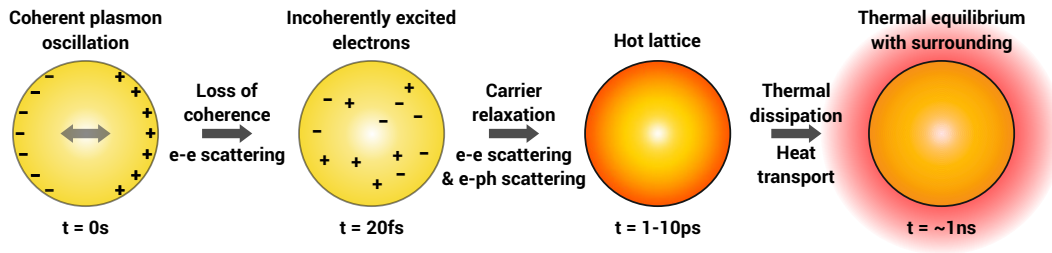


Figure 2.10 – Incoherent decay of a plasmon. Upon excitation of a plasmon ($t = 0$ s), the electrons lose their coherence by individually scattering with each other leading to high energetic incoherent electrons. The carriers relax through further electron-electron and electron-phonon scattering events until reaching thermal equilibrium with the lattice. Subsequently, the energy dissipates to the surrounding until a global thermal equilibrium is reached.

thermal conductivity, respectively. $Q(\mathbf{r}, t)$ is the heat source term that stems from plasmonic heating, which is assumed to be homogeneous ($Q(\mathbf{r}, t) = Q_0$ within the particle) as described above. Since the timescales of the effects discussed within this thesis are much slower than nanoseconds, the time dependence is neglected at this point and only the time independent case is considered. Q_0 can be obtained from the absorption cross section and the incident light intensity as described later on (Section 3.2.3). For a spherical particle in an isotropic medium, an analytic expression for the temperature distribution outside the nanoparticle in the thermal equilibrium can be derived from Equation 2.29:⁵⁴

$$\Delta T(r) = \frac{V_{NP} Q_0}{4\pi k_0 r}, \quad (2.30)$$

where r depicts the distance from the center of the nanoparticle. However, in the realm of this thesis, the isotropy of the particles is broken either by their shape, their composition or both. Thus, Equation 2.29 has to be solved numerically, which is done with COMSOL as described in Section 3.2.3. Nonetheless, one can recognize the linear dependence of the temperature on Q_0 and the inverse dependence on r from Equation 2.30, which still hold as a rule of thumb for anisotropic systems. In many applications of both trapping and printing, plasmonic heating can be a major obstacle since the raised temperature increases Brownian motion, thereby significantly reducing trapping^{27,65} and printing accuracy.^{29,66} Furthermore, plasmonic heating leads to thermophoretic repulsion, thus making optical printing of plasmonic nanoparticles in close vicinity difficult.^{67,68}

However, the inevitable occurrence of plasmonic heating can also be used as an advantage by using the particles as nanoscopic heat sources, which has lead to numerous applications.^{7,8,38,69,70,71,72} For example, Fedoruk *et al.* introduced a new approach to either carve out structures⁷² or induce cross-linking of a polymer⁷ below the diffraction limit using a combination of plasmonic heating and optical forces, which is a completely new approach

for nanolithography. Moreover, for gold nanorods, plasmonic heating can lead to substantial morphological changes due to enhanced surface diffusion,^{32,73,74} which is exploited later in this thesis by splitting nanorods into dimers in Chapter 5.

2.5 Melting of gold nanorods

As previously described, irradiating plasmonic particles with laser light leads to significant heating due to nonradiative decay of the plasmon. If the incident laser power density is sufficient, conformational changes are induced by temperature.⁷⁵ In the case of spherical particles, no shape change is observed upon heating since they already have the thermodynamically most favorable shape. Structural changes can only be observed for the crystal structures, which have a minor effect on the optical properties.⁷⁶ Only for very high intensities Coulomb explosions, where the internal electron pressure becomes high enough, to lead to a disintegration of the particle have been reported.⁷⁷ When considering melting processes, one has to take into account that the melting point of gold is significantly decreased for nanoparticles with radii below 10 nm.^{78,79} Publications suggest the disappearance of a sharp melting point and propose curvature driven surface diffusion that becomes gradually stronger for increasing temperatures.⁸⁰

For non-spherical particles, plasmonic heating can induce shape changes. Since a sphere is always the energetically most favorable shape a particle can obtain, non-spherical particles are trapped in a metastable state. At room temperature however, the activation energy is too high to induce conformational changes.⁸¹ Two seminal publications from Link *et al.* investigated both the time scale⁷⁵ and the morphology change⁷³ of the melting process of gold nanorods. The increased temperature induces point crystal defects in the center of the rod that form the nuclei for eventual twinning and stacking boundaries. Subsequently, the outermost atoms move towards the rod center by surface diffusion reducing the particle surface. The complete reshaping of a nanorod to a sphere was determined to take at least 30-35 ps.⁷⁵

For metal nanowires that feature, in contrast to nanorods, much higher aspect ratios both conventional⁸² and plasmonic laser heating⁸³ have been reported to lead to the formation of chains of equally sized spherical particles. This effect can be attributed to Rayleigh instability that occurs upon melting of the nanowires. This theory was initially introduced for cylindrically shaped liquid droplets of infinite length by Plateau and Lord Rayleigh.^{84,85} It states that such droplets break up leading to the formation of equally sized spherical droplets. The driving force behind this process are chemical potential gradients along the surface which are induced by perturbations in the rod radius. Such perturbations are always present due to friction with the surrounding or temperature. Due to the cylindrical shape, one can assume a sinusoidal

shape of the perturbation with a wavelength λ . Depending on the diameter of the cylinder at a certain λ , the perturbation grows exponentially over time leading to an eventual breakup of the cylinder.⁸² This theory was later extended to cylinders of finite length,⁸⁶ where a critical aspect ratio of 7.2 was found, above which the droplet splits up into two equally sized spheres. This model only takes surface diffusion as the driving force into account and is in good agreement with the findings described before for the melting of nanorods. In Chapter 5, it is shown for the first time that by applying additional forces to a nanorod during its melting process, splitting can indeed be induced on single nanorods of aspect ratios below 7.2.

2.6 Optically induced thermophoresis of plasmonic Janus particles

Till now, only homogeneous gold particles have been described. However, breaking the isotropy with regards to the material composition leads to more complex effects. Such particles featuring two sides of different physical properties have been reported before.⁸⁷ Due to their physical bifunctionality they are commonly referred to as Janus particles, a term coined by C. Casagrande and M. Veyssié,⁸⁸ relating to the ancient roman god, *Janus*, who is usually depicted with two faces, one looking into the future and the other one into the past.

The two sides of such a Janus particle can differ in surface chemistry, magnetic properties or optical behavior among others.⁸⁷ One application for Janus particles that has emerged in recent years is their use as optically controlled microswimmers.⁸⁹ Here, systems are found, where the anisotropic character of the Janus particles leads to phoretic effects such as self-diffusophoresis⁹⁰ or self-thermophoresis⁹¹ inducing a force on the particle from a concentration or a temperature gradient, respectively. Thermal gradients can be created through laser irradiation of metal-dielectric Janus particles.⁹² In this case, the metal side was created by evaporating a thin gold film on a self assembled monolayer of silica spheres. Subsequent sonication released the particles into a solvent of choice. When irradiated, photons are only absorbed by the gold film that covers one half of the particle but not by the dielectric part of the sphere. Hence, it is an asymmetric heat source that leads to a temperature gradient over the whole particle. The phoretic effects of metal dielectric Janus particles in an optical trap were investigated in numerous publications^{9,10,11} and form the foundation for the findings in Chapter 6, where such particles are introduced for the first time at the nanoscale.

Thermophoresis

Colloidal particles or molecules exposed to a temperature gradient are subject to thermophoretic forces.⁹³ When dispersed in a solvent, the particles move away from the heat

source. This effect, known as thermodiffusion or *Ludwig-Soret* effect stems from the inhomogeneous Brownian motion present in any medium with a thermal gradient, since the magnitude of Brownian motion scales directly proportional with temperature. The diffusion of a particle can be expressed by the *Einstein-equation*:⁹⁴

$$D = \mu k_B T \quad (2.31)$$

Here, D is the diffusion constant, a measure of the diffusivity in the units m^2/s . μ is the mobility of the particle given as the ratio of its drift velocity v_D to an external Force F_{ext} . In the low Reynolds number regime, *i.e.* $\text{Re} < 1$ that is maintained throughout this thesis due to the small length scales (nm) and the moderate velocities involved (m/s),⁹⁵ one can apply Stokes law for a spherical particle, yielding the *Stokes-Einstein-relation*:

$$D = \frac{k_B T}{6\pi\eta r} \quad (2.32)$$

In a microscopic picture, Brownian motion can be seen as a random force exerted by an individual object on its surrounding.⁹⁶ For a spherical object of radius r in a medium of dynamic viscosity μ_f , this force can be expressed using:⁹⁶

$$F_{\text{Brownian}} = \mathbf{R} \sqrt{\frac{12\pi r \mu_f k_B T}{\Delta t}}. \quad (2.33)$$

Here, \mathbf{R} is a vector with Gaussian distributed number components of zero mean and unit variance, to take into account the stochastic nature of the force. Δt is the duration of force transmission. According to Equation 2.33, the Brownian force is stronger for higher temperatures. Hence, particles or molecules dispersed in a solvent experience a net time-averaged force away from the higher temperature, which is referred to as thermophoretic force (Figure 2.11).

A critical parameter when considering thermophoresis is the *Knudsen-number* Kn . In fluid dynamics it is a measure to determine whether a system has to be treated within the realm of continuum mechanics or statistical physics. It is defined as,⁹⁷

$$\text{Kn} := \frac{\lambda}{l}, \quad (2.34)$$

with λ being the mean free path and l the representative physical length scale that equals the particle diameter here. In literature, three different regimes are distinguished, namely the *near-continuum regime* for $\text{Kn} \rightarrow 0$, the *free-molecule regime* for $\text{Kn} \rightarrow \infty$ and the *transition regime* in between.⁹⁷ Within this thesis, only thermophoresis of nanometer to micron sized particles in water is treated. In liquids, λ is on the scale of the molecular diameter ($\lambda \approx 0.3 \text{ nm}$)⁹⁸

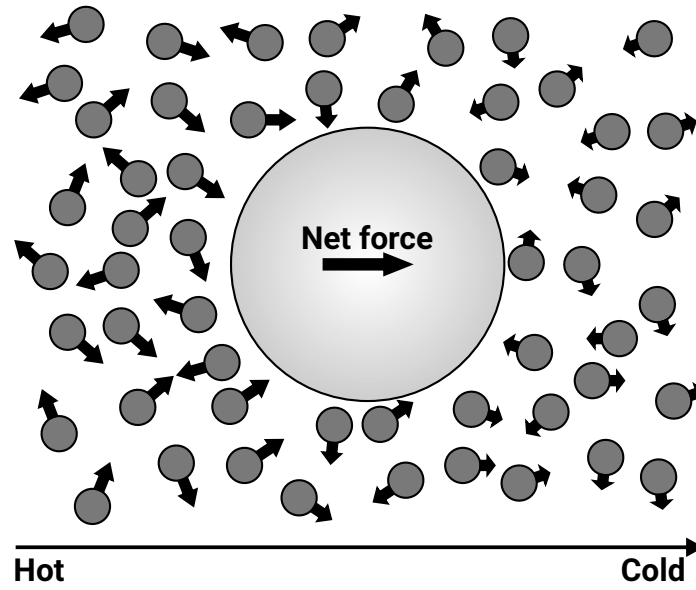


Figure 2.11 – Thermophoresis of a colloidal particle (light grey) in a solvent (dark grey). The momentum (black arrows) the solvent molecules carry due to Brownian motion on the hot side is higher than on the cold side. Brownian motion is undirected, but on average, the colloidal particle experiences more momentum transfer on its hot side than on the cold side, leading to a net force pushing it from the hot to the cold region.

and hence $\text{Kn} \rightarrow 0$. Therefore, the following derivations equations are all derived under the assumption of a *near-continuum regime*.

An analytical model for the thermophoresis of spherical particles was developed by Epstein with an expression for the thermophoretic velocity of a sphere embedded in a hydrodynamic medium \mathbf{v}_{tp} using a continuum mechanics approach:⁹⁹

$$\mathbf{v}_{\text{tp}} = -\frac{3}{2} \frac{k_f}{2k_f + k_p} \frac{\mu_f}{\rho_f} \frac{\nabla T}{T_0}. \quad (2.35)$$

k_f and k_p are the thermal conductivities of the fluid and the particle material, respectively. ρ_f is the fluid density and T_0 the average temperature in the vicinity of the particle. Assuming Stokesian drag ($\mathbf{F}_{\text{drag}} = -6\pi\mu_f r \mathbf{v}$) as the restoring force, one can describe the thermophoretic force \mathbf{F}_{tp} according to:

$$\mathbf{F}_{\text{tp}} = 6\pi\mu_f r \mathbf{v}_{\text{tp}} = -6\pi\mu_f r \frac{3}{2} \frac{k_f}{2k_f + k_p} \frac{\mu_f}{\rho_f} \frac{\nabla T}{T_0} \quad (2.36)$$

This equation only holds for the case of a spherical particle of radius r . However, this thesis focuses on anisotropic particles, in particular rod-shaped ones which will be presented in more detail in Chapter 6. As already discussed in Section 2.2, a good approximation for a rod is a prolate spheroid. Here, the thermophoretic force was found to be:¹⁰⁰

$$F_{\text{tp-spheroid}} = -\frac{6\pi\mu_f^2 \tau_o + (1 - \tau_o^2) \coth^{-1}(\tau_o)}{\rho_f T_o (1 + \tau_o^2) \coth^{-1}(\tau_o) - \tau_o} \times \frac{\nabla(T)c\tau_o k_f}{k_p(1 - \tau_o^2)(\tau_o \coth^{-1}(\tau_o) - 1) + k_f \tau_o((\tau_o^2 - 1) \coth^{-1}(\tau_o) - \tau_o)} \quad (2.37)$$

τ_o is defined as $\tau_o = [1 - (a/b)^2]^{-1/2}$ and $c = (b^2 - a^2)^{1/2}$ with a and b being the two radii of the spheroid.

While in the continuum regime, the assumptions made for Equation 2.36 and Equation 2.37 are only entirely true for a particle in a gaseous environment. When dispersed in a fluid, as it is the case for the experiments discussed in this thesis, the physical circumstances the particle is exposed to are different. While this is not discussed in detail here, MacNab and Meisen have empirically determined a correction factor of 0.17 from the Epstein model for thermophoresis in liquids.¹⁰¹

Self-thermophoresis of metal dielectric Janus particles

A metal-dielectric Janus particle irradiated by a laser is subject to a self induced temperature gradient and hence a thermophoretic force leading to a movement of the particle.⁹¹ However, since the movement of the particle depends on its orientation which is subject to rotation, this movement is not directed leading to enhanced diffusion⁹² unless a feedback mechanism is applied.^{102,103}

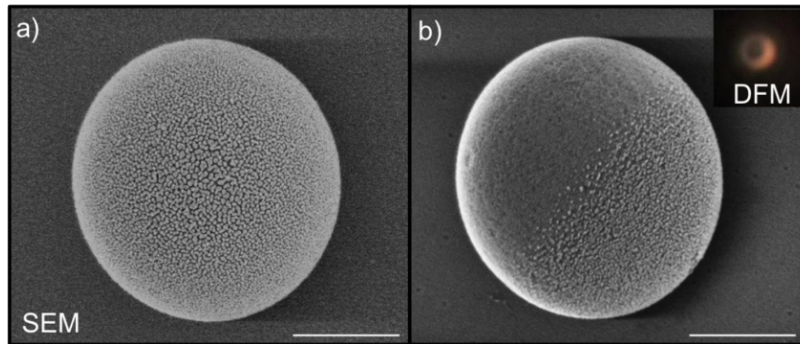


Figure 2.12 – Spherical gold-silica Janus particle. Top (a) and side (b) view of the Janus particles used by Nedev *et al.*. The inset shows a single Janus particle in the dark field microscope. The scale bars are 500 nm. Figure adapted from Nedev *et al.*⁹

Nedev *et al.* exploited the thermophoretic force in a different way, by trapping metal-dielectric Janus particles using optical tweezers and thus directing the force.⁹ This was made possible by evaporating only a very thin (5 nm) gold film on top of the microspheres. At such film thicknesses, the gold does not form a continuous film, but rather small unconnected gold islands (Figure 2.12). In case of a continuous film scattering and absorption is enhanced and

thus the scattering force would dominate over the entire spectrum. The gold islands on the other hand can be seen as small gold nanoparticles and gradient forces dominate in the near infrared.

Upon trapping a Janus particle a movement along the optical axis of the optical trap oppositely directed to the Poynting vector was observed. In this case, the main restoring force for the thermophoretic force is the optical force from the tweezer rather than the Stokes drag. The gold side points away from the incident light as here the scattering is higher than on the dielectric side. Further smaller contributions are gravity (F_{grav}) and buoyancy (F_{buo}) (Figure 2.13). The particle stabilized in the trap at a fixed position, where the force contributions equilibrate according to:

$$|F_{\text{grav}}| + |F_{\text{scat}}| + |F_{\text{grad}}| = |F_{\text{buo}}| + |F_{\text{tp}}|. \quad (2.38)$$

Since ∇T in Equation 2.36 increases for higher laser intensities, the thermophoretic force becomes stronger by increasing the incident laser power. Hence, the particle moves upwards in the configuration of Figure 2.13. Therefore, this effect can be exploited to tune the vertical position of a trapped Janus particle over several microns by just changing the laser intensity.

When moving along the z -axis, the course of the electric field intensity is not monotonic. Figure 2.14a shows the intensity distribution of a laser trap with $NA = 1.0$ and $\lambda = 1064 \text{ nm}$. Position 1 marks the intensity in the focal plane, where the main maximum of light intensity is located. Due to self-interference, the intensity undergoes a minimum (position 2) before entering another maximum of intensity at position 3. As a consequence, there is no stable

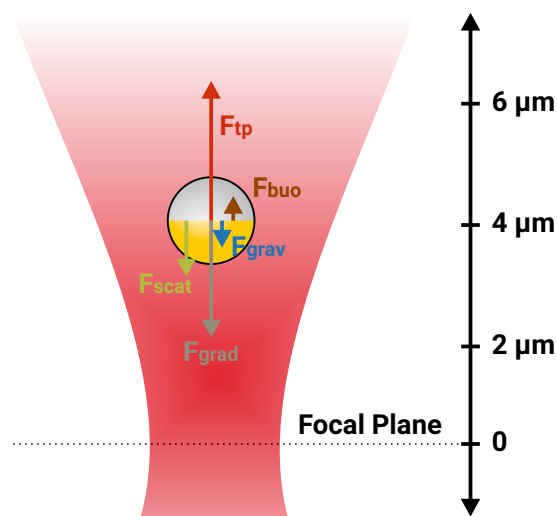


Figure 2.13 – Forces in the Janus particle elevator. Thermophoretic and buoyancy forces push the Janus particle upwards, whereas gravity, gradient and scattering forces push it downwards until a force equilibrium is reached. Figure adapted from Nedev *et al.*⁹

trapping at position 2 leading to the particle undergoing a jump in z -direction to position 3. This leads to a hysteresis in the vertical movement when cycling the laser intensity (Figure 2.14b, c). In upwards direction, the thermophoretic force has to be strong enough to overcome this potential optical force minimum, whereas in downward direction it has to be weak enough to be pulled down by the gradient forces into the primary trap.⁹

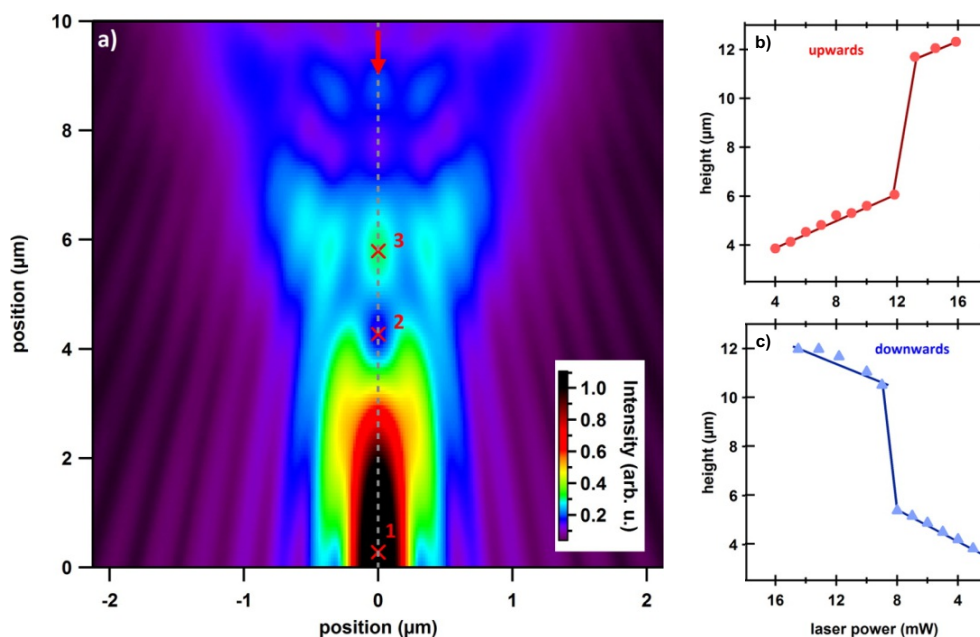


Figure 2.14 – Vertical movement of a Janus particle in a laser trap. (a) Intensity profile of the laser trap showing maxima (1,3) surrounding a minimum (2) in vertical direction. Vertical position of a Janus particle for increasing (b) and decreasing (c) laser power exhibiting a hysteresis. Figure adapted from Nedev *et al.*⁹

Ionic effects

All of the above observations assume a particle dispersed in a homogeneous medium. However, when adding ions to the solution, the whole situation becomes much more complex as thermo-osmotic as well as thermo-electric effects are induced under certain circumstances.

Thermo-osmotic effects arise due to the ions distributing inhomogeneously in a temperature gradient. In an ionic liquid, the ions form layers around dispersed particles screening the inherent surface charges. In equilibrium, the thickness of such layers around a spherical particle is determined by the *Debye-length*:¹⁰⁴

$$\lambda_D = \sqrt{\frac{\varepsilon k_B T}{8\pi c v e^2}}. \quad (2.39)$$

Here, ε describes the solvent refractive index, and c and $v \cdot e$ the concentration and charge of the ions, the latter of which is taken as +1 in the following for the sake of simplicity. Due

to the temperature dependence of Equation 2.39, the layers lose their spatial symmetry and are distorted. This leads to an increase of the ion concentration on the cold side of the particle and therefore to a pressure acting against the temperature gradient. Hence, a flow close to the surface of the particle of ionic liquid arises, directed from the cold to the hot side, which can be described as:¹⁰⁵

$$\mathbf{v}_{\text{thermo-osmo}} = \frac{\varepsilon\zeta^2}{3\eta} \frac{\nabla T}{T} \quad (2.40)$$

η and ζ are the solvent viscosity and the surface potential of the particle, respectively. The latter can be expressed in terms of λ_D as:¹⁰⁵

$$\zeta = \frac{2k_B T}{e} \operatorname{arsinh}(2\pi\sigma l_B \lambda_D) \quad (2.41)$$

Here, σ is the number density of elementary charges. According to equations 2.39 to 2.41 the amplitude of the thermo-osmotic effect depends on λ_D and hence on the salinity of the medium. As the area hyperbolic sine is a monotonically increasing function, $\mathbf{v}_{\text{thermo-osmo}}$ increases with temperature.

Another contribution in ionic media stems from the *thermo-electric* effect.¹⁰⁵ This effect can both enhance or counteract the thermo-osmotic effect, depending on the size and solvation energy of the ions.¹⁰⁶ Different ions absorb different amounts of heat upon an increase of temperature, a quantity referred to as heat of transport Q_i . This leads to a non-uniform diffusion of the different ions (e.g. cations and anions) in the vicinity of the particle and hence, the occurrence of an electric field around the particle. Very much as *thermo-osmosis*, this effect distorts the ion cloud around the colloid and therefore adds another contribution to the phoretic velocity that can be expressed as:¹⁰⁵

$$\mathbf{v}_{\text{thermo-elec}} = \frac{\varepsilon\zeta}{\eta} \frac{(Q_- - Q_+)}{2e} \frac{\nabla T}{T}. \quad (2.42)$$

From Equation 2.42 follows that the direction of this contribution depends on the difference of the heats of transport ($Q_- - Q_+$), which can be both negative or positive depending on the electrolyte.

Both effects strongly influence the amplitude of the elevation of Janus particles. This leads to an attenuation or even an inversion of the elevator effect for increasing salt concentrations.¹⁰ By using different electrolytes with a negative, a neutral and a positive thermo-electric effect, it is possible to discern the magnitudes of both effects and add another chemically controlled degree of freedom to particle manipulation.

A first application of the optical Janus particle elevator has been shown by stretching DNA molecules that were connected to the gold side of a Janus particle and the substrate by

lifting the particle with a force of 0.1 to 7 pN.¹¹ However, one major drawback is the significant size of the Janus particle since they feature a diameter of 1.3 μm . Furthermore, the hot region of the particle is relatively broad. Both properties can cause problems when working with biological cells, since they are of a similar size. This renders micron sized particles unsuitable for many experiments, where specific sites of the cell are targeted. Furthermore, a localization of the heat source is important in order to keep thermal damage of cells at a minimum level. In Chapter 6, these issues are tackled by the introduction of Janus nanoparticles that feature similar properties at the nanoscale and are successfully applied for biomolecular transport into living cells.

Chapter 3

Methods: From microscopy over numerical modeling to cell culture

For experiments and their analysis, a variety of spectroscopic and microscopic techniques as well as computational methods have been used. This chapter starts with a short introduction to the most important methods used during the course of this thesis, such as dark field microscopy, epifluorescence microscopy, UV-Vis spectroscopy and scanning electron microscopy. Subsequently, the numerical methods applied to calculate the electrodynamic response of plasmonic nanoparticles, optical forces, thermal conductance and hydrodynamics are presented. The chapter closes with the protocols for biological cell growth and fixation.

3.1 Nanoparticle characterization and manipulation

Manipulating and characterizing nanoparticles requires specialized methods, which are presented in the following. First an introduction to dark field microscopy is given, with the optional extensions for laser manipulation and single particle spectroscopy. This universal tool was applied to all plasmonic particles investigated in this work. Furthermore, epifluorescence microscopy, used for imaging of the dye functionalized nanopens is introduced as well as UV-Vis spectroscopy for the bulk characterization of plasmonic nanoparticles. The chapter ends with a brief summary of scanning electron microscopy, the technique applied to identify the exact morphologies of the nanoparticles.

3.1.1 Dark field microscopy and laser manipulation

As described in Section 2.1, gold nanoparticles feature a drastically enhanced scattering cross section with respect to their actual physical dimensions. In a dark field microscope (DFM), the central beam is blocked out in such a way that only light scattered by the sample is collected through the objective. This leads to objects appearing as bright spots on a dark background. This imaging technique can be realized with a transmission light microscope by putting a dark field condenser into the light path thus creating a hollow light cone when the focal plane is aligned to the focal plane of the objective. An overview of this configuration is depicted in Figure 3.1 a. Furthermore, for a successful dark field illumination the numerical aperture (NA), which is defined as $NA = n \cdot \sin(\alpha)$ of the inner light cone of the condenser, has to be higher than the NA of the objective. Otherwise, light from the illumination source would enter the objective directly, thus outshining the scattering objects. Here, n is the refractive index of the immersion medium and α the half angle of the focused cone of light. Therefore, only scattering or luminescent objects are visible under dark field conditions making this microscopy method an ideal tool to examine strong light scatterers like plasmonic nanoparticles. Since only the scattered light is imaged directly, plasmonic particles appear in the color of their plasmon resonance. A comparison of a blue spherical silver particle ($\lambda_{\text{res}} = 450 \text{ nm}$), a green spherical gold particle ($\lambda_{\text{res}} = 550 \text{ nm}$) and a red gold nanotriangle ($\lambda_{\text{res}} = 800 \text{ nm}$) is shown in Figure 3.1 c-e.

By putting beam splitters or dichroic mirrors into the optical axis of the microscope above the objective, laser beams can be coupled into the microscope and be focused onto the substrate simultaneously as shown in Figure 3.1 b. As described previously in Section 2.1.1, tightly focused laser beams have proven to exert attractive as well as repulsive forces, commonly referred to as trapping and printing of plasmonic nanoparticles. Moreover, by using a laser

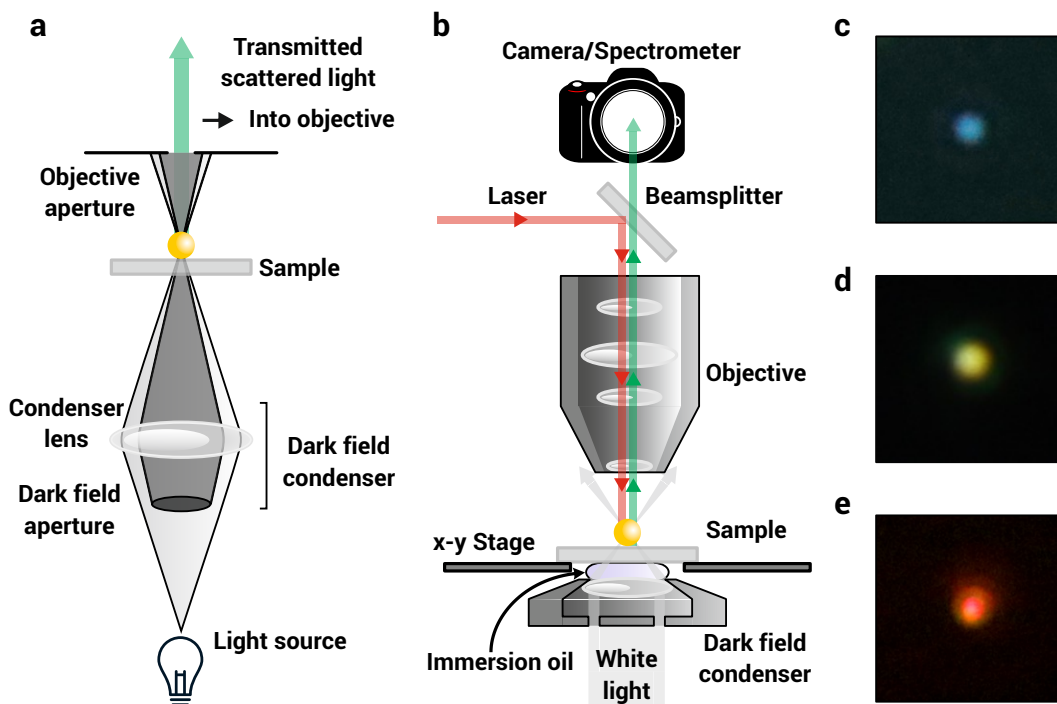


Figure 3.1 – Dark field microscopy. (a) Detailed scheme of a transmission dark field microscopy configuration. The dark field condenser creates a hollow light cone, which is focused in the optical plane and later blocked by the objective aperture. This way, only scattered light enters the objective. (b) Scheme of the dark field configuration including laser coupling and spectrometer/camera. Dark field images of spherical 80 nm (c) silver and (d) gold particles as well as a (e) gold nanotriangle. Due to their shape and material properties, they appear in the colors blue, green and red, respectively.

of a wavelength close to the particle plasmon resonance, substantial plasmonic heating can be induced in individual nanoparticles (cf. Section 2.4).

In this work, two different DFMs were used, both based on a conventional upright microscope, namely a Zeiss Axio.tech 100 and a Zeiss Axio.Scope.A1 (Carl Zeiss AG, Germany), illuminated by a 100 W halogen white light source. To obtain dark field conditions a Zeiss ultra condenser with numerical apertures of 1.2 and 1.4 for the inner and outer light cone was put into the white light beam. Immersion oil that matched the refractive index of the glass cover slides ($n = 1.531$) was used to avoid reflections from the glass cover slide. For manipulation experiments a Zeiss Achroplan 100x/1,0 W (Carl Zeiss AG, Germany) water dipping objective was used. Imaging was performed using a commercial DSLR camera (Canon EOS 6D, Canon, Japan) connected to the microscope. Three different lasers were coupled into the optical axis of the microscope in the realm of this thesis, namely a 532 nm Coherent Verdi V10 (Coherent, USA) laser, a 808 nm Ti:Sapphire oscillator operated in *cw*-mode (Spectra Physics Tsunami, Spectra Physics, USA) and a 1064 nm Cobolt Rumba (Cobolt, Sweden) laser. Positioning of the sample was realized using a computer controlled *x-y* piezo stage.

Dark field spectroscopy has proven to be a powerful tool to investigate the optical properties of individual plasmonic particles.¹⁰⁷ Therefore, grating spectrographs (Princeton Instruments SP300i and SP2300, Teledyne Princeton Instruments, USA) were implemented to the output port of the microscope. The entrance slit was aligned to the center of the field of view of the microscope allowing for easy targeting of individual nanoparticles. The spectrographs expanded the light onto liquid nitrogen cooled CCDs (Princeton Instruments MicroMAX or Spec-10, respectively, Teledyne Princeton Instruments, USA). As mentioned before, the particle coloring matches their scattering spectrum in dark field microscopy. Hence, the spectrum of individual particles can be recorded.

3.1.2 Epifluorescence microscopy

Epifluorescence microscopy is commonly used to image photoluminescent materials. The main principle is to use an excitation light source that does not overlap with the emission wavelength of a photoluminescent material. By using a correct filter configuration, this allows to detect only the emitted photoluminescent light without any background. Here, as illustrated in Figure 3.2, a filter is put between the sample and the excitation light source, which cuts off the wavelength region that overlaps with the emission of the photoluminescent material. Hence, the photoluminescent emission can be separated from the excitation light by using a dichroic mirror that has its reflectance edge right between excitation and emission wavelength in combination with an additional filter that blocks out the remaining excitation light. Hence, only light emitted *via* photoluminescence reaches the detector leading to photoluminescent structures appearing bright in front of a dark background. In the realm of this thesis, an inverted microscope (Olympus IX81, Olympus, Japan) in combination

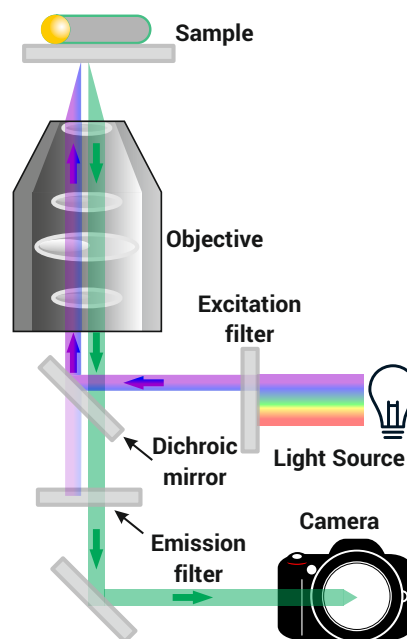


Figure 3.2 – Epifluorescence microscopy. The excitation light is filtered with a short pass filter with an edge wavelength at the absorption maximum of the sample. The excitation and emission light beams are separated by a suitable dichroic beam splitter. Any remaining scattered excitation light is filtered by a long pass emission filter. Hence, photoluminescence only is detected.

with a mercury arc lamp (HBO 103/W) was used. The filter set used (Olympus U_MNB2, Olympus, Japan) was chosen to match the absorption (495 nm) and emission peaks (517 nm), of the dye used in the later experiments (6-FAM, cf. Chapter 4).

3.1.3 UV-Vis spectroscopy

UV-Vis spectroscopy is a standard tool to measure the wavelength dependent extinction of colloidal nanoparticles in bulk. Here, the light of a Xenon arc lamp is dispersed within a monochromator. A prism scans the desired spectral range through a slit and a detector measures the transmitted attenuated signal of the sample (I) while a second detector reads out a reference beam without any sample (I_0) simultaneously (Figure 3.3). The signal is then corrected with a previously measured baseline to account for absorption of both cuvette and solvent. The UV-Vis measurements in this thesis were carried out using an Agilent Cary 60 (Agilent, USA) spectrophotometer. The transmittance of a gold nanoparticle dispersion can be expressed as a function of σ_{ext} , the cuvette thickness d and the particle concentration n (Beer-Lambert Law):¹²

$$T = \exp \left[-\frac{\sigma_{\text{ext}} d}{n} \right], \quad \sigma_{\text{ext}} = -n \cdot \frac{1}{d} \ln \left(\frac{I}{I_0} \right). \quad (3.1)$$

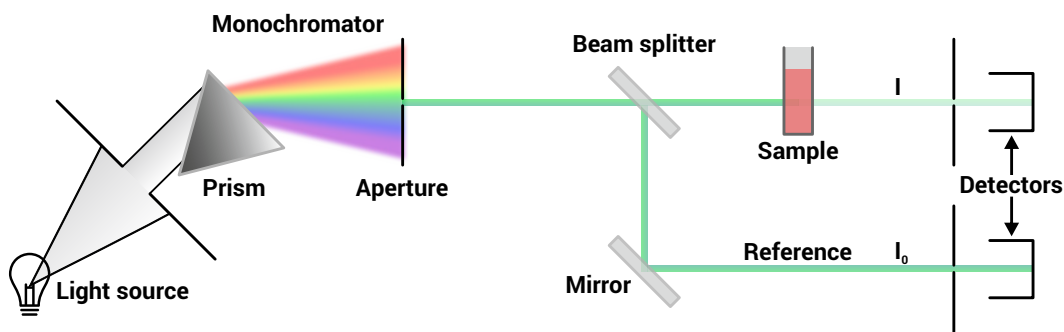


Figure 3.3 – UV-Vis spectroscopy. White light passes a monochromator and is then split up into a primary beam passing the sample and a secondary beam used as reference. The ratio between both beams yields the relative absorption.

3.1.4 Scanning electron microscopy

The nanoparticles investigated in this thesis have sizes well below the optical diffraction limit. Spectral properties of individual particles can be measured with dark field microscopy as described in Section 3.1.1. However, this information does not yield any information about the morphology of the nanoparticle since many shapes can result in very similar optical properties (cf. Section 2.2). Therefore, in order to investigate the particle morphology, scanning electron

microscopy (SEM) was applied. Here, an electron beam is focused on the substrate *via* electron lenses and scanned over the sample. An image is then calculated from the signal of several detectors measuring the scattered electron current.

The maximum resolution is limited by the *de Broglie* relation, which depends on the momentum p of the electron:¹⁰⁸

$$\lambda_e = \frac{h}{p} \quad (3.2)$$

Since the acceleration voltages U used here ranged from 1 kV to 5 kV that yield non-relativistic electron energies one can assume classical electrodynamics. Therefore, it holds:

$$\lambda_e = \frac{h}{\sqrt{2eUm_e}} \quad (3.3)$$

Here, h is the Planck constant and e and m_e the electron charge and mass, respectively. This yields wavelengths of several tens of picometers, thus providing the required resolution to image also smaller features of nanoparticles.

Figure 3.4a shows the electron beam path of a field emission SEM as used in this thesis.¹⁰⁹ Here, electrons are extracted by applying a strong field to a tip-shaped cathode which leads to the electrons tunneling out of the material thus yielding a very narrow energy distribution in contrast to conventional thermal electron emitters, where electron energies follow a broad Maxwell-Boltzmann distribution. This greatly reduces chromatic aberration. Furthermore, since the electrons are all emitted from a sharp tip, the spot diameter and hence the resolution is much finer.¹⁰⁹

The scattering of the incident primary electrons on the specimen can take place elastically and inelastically, thus without and with energy transfer to the sample. The respective scattered electrons are called primary and secondary electrons. Depending on the position and the energy of the detected electrons, different informations like topography or composition can be gained.¹⁰⁹ The Zeiss 55 Ultra Plus SEM (Carl Zeiss AG, Germany) used in the realm of this thesis features three

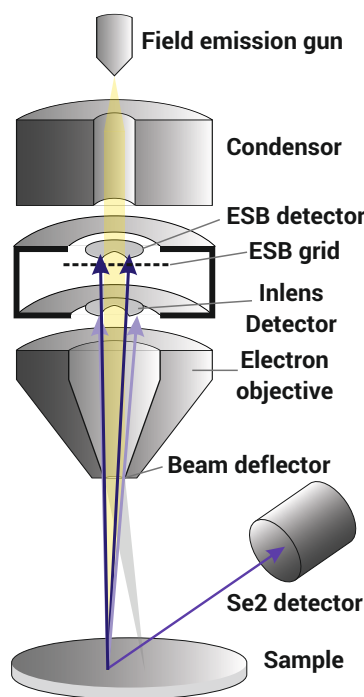


Figure 3.4 – Scanning electron microscope. Sketch of the electron beam path within an SEM and the three different detectors.

detectors, namely the **Inlens** and the **SE2** for secondary electrons and the **ESB** detector for primary backscattered electrons.

- The **Inlens** detector is a ring shaped detector that is placed directly inside the electron lens column.^{109,110} Therefore, it has a very small distance to the sample, making it the detector with the highest spatial resolution.¹¹⁰
- A very common detector, present in almost all commercially available SEMs, is the **SE2** (secondary electron 2) detector also known as Everhart-Thornley detector.^{111,110} It consists of a scintillator inside a Faraday cage connected by a waveguide to a photomultiplier outside of the chamber. The Faraday cage attracts low energy electrons and accelerates them to the scintillator, where they are converted to photons. Those light pulses are subsequently coupled into the waveguide and detected in a photomultiplier outside the chamber. The low energy of the detected electrons means that they were scattered close to the surface of the sample.¹⁰⁹ It is mounted with a certain angle to the electron gun, which makes it a good tool for topological measurements.¹⁰⁹
- A very useful detector when imaging hybrid structures is the **ESB** (energy selective backscattered) detector due to its capability to image material contrasts.¹¹² Here, backscattered electrons are filtered out by a voltage grid from the less energetic secondary electrons. Backscattered electrons emerge from elastic scattering processes with the specimen atoms, which is more probable for heavy elements. Thus, structures consisting of heavy elements appear brighter than those composed of lighter atoms.¹¹² Due to the poor spatial resolution of backscattered electrons, the compositional signal is mixed with a topological signal obtained from secondary electron detection.

3.2 Numerical modeling

Many of the results obtained in this thesis were verified up by numerical calculations. Due to the diversity of the involved effects different methods were required. This chapter starts off with the finite-difference time-domain (FDTD) method, a wide spread approach to calculate the electrodynamic response and thus the scattering and absorption spectra of plasmonic nanoparticles. Furthermore, three different approaches to calculate optical forces, all suitable for different situations are introduced. Finally, the finite elements method (FEM) is presented as a tool to calculate heat transfer and convection.

3.2.1 Electrodynamics calculations with the finite-difference time-domain method

The finite-difference time-domain method is a major tool to solve Maxwell's differential equations for complex geometries. In particular it has become one of the standard methods to calculate absorption and scattering coefficients as well as field enhancements of plasmonic nanoparticles.¹¹³ Here, after defining an electromagnetic wave source, a spatial grid is calculated yielding $E(\mathbf{r}, t)$ and $H(\mathbf{r}, t)$. The choice of source and grid properties is crucial for a successful and realistic calculation. The field distributions are calculated by dividing the simulation volume into a grid of rectangular so-called *Yee-cells* named after the inventor of the method Kane S. Yee.¹¹⁴ Here, the electric and magnetic field cells are interleaved in a way that the electric field components form the normals to the faces of the magnetic field cell and vice versa (Figure 3.5a), which are calculated alternatingly. The only input information is provided by assigning a wavelength dependent dielectric function to each cell, which is usually sourced by fitting to measured values from literature for a given material. As a time-domain method, one simulation run provides the solution for the entire input spectrum at once by Fourier transforming the time-dependent electric fields. Furthermore, this allows for the observation of the temporal evolution of the electric field, which can be advantageous for many applications. For steady state solutions the simulations run until convergence is achieved. Both near- and far-field are obtained as the final result.

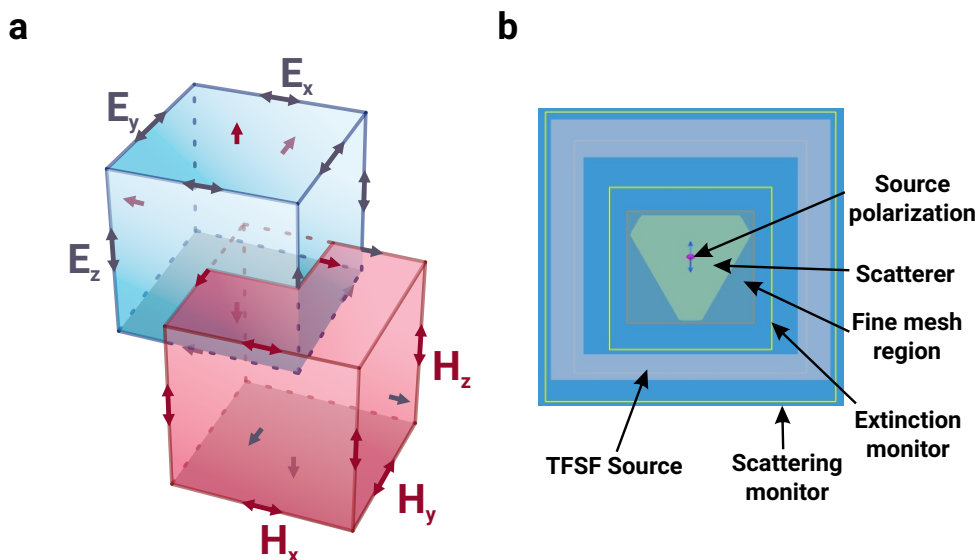


Figure 3.5 – Simulation of plasmonic particles with the FDTD method. (a) Interleaved rectangular three dimensional grid for E- and H-field components. (b) Typical setup of the TFSF approach in Lumerical FDTD solutions. The nanoparticle of interest (scatterer) is surrounded by the TFSF-source. Placing field monitors inside and outside of the source box gives extinction and scattering cross sections, respectively. A mesh refinement around the plane of the scatterer is required in order to avoid artifacts. Here, the initial wave propagates out of the plane with a vertical polarization.

In the realm of this thesis, absorption and scattering cross sections as well as near-field distributions of plasmonic nanoparticles were calculated using a variant of FDTD, the *Total-field scattered-field* (TFSE) approach, which is implemented in Lumerical FDTD Solutions (Lumerical Solutions Inc., Canada). Here, the simulation volume is separated into two distinct regions containing the total (*i.e.* the sum of incident and scattered field) and the scattered field, respectively. An incident plane wave propagating perpendicular to the injection surface Λ_{in} is used as the incident field, which is subsequently subtracted at the end surface Λ_{end} . This yields the region in between the planes that contain both scattered and incident field, when a scatterer is present within this volume. The outside of this region only contains the scattered light. The electric field can be monitored using power monitors at a given position. Putting such a box inside the source yields the extinction coefficient of the scatterer after normalization with the incident field. A box of power monitors in the outer region features the scattering coefficient, respectively. An overview of the simulation regions is given in Figure 3.5b. Here, the plane wave propagates out of the plane.

Furthermore, the near-field of nanostructures can be visualized by putting power monitors inside the plasmonic structure of interest. This allows to spatially resolve the electric field amplitude, data which is commonly used to calculate near-field enhancement factors.¹¹⁵ Within the realm of this thesis, the E- and H-field amplitudes within the particles were used to calculate the *Maxwell Stress tensor* as described in Section 3.2.2.

In reality, the waves would propagate and decay to infinity. However, the simulation volume has to be limited to ensure convergence. Therefore, this decay is modelled by surrounding the simulation volume with a number of *Perfectly matched layers* (PML) featuring an extremely low reflectivity among them. A main advantage of this method is that it gives quantitative results and thus allows to compare the scattering and extinction cross sections of different particles.

When implementing a new geometry, several parameters have to be taken into account in order to attain trustworthy results. Like in any mesh based numerical method, the choice of a sufficiently fine mesh size is the most important. Otherwise, artifacts can occur in both field distributions and calculated spectra. Here, the mesh is refined around the scatterer to cover the interface more accurately. The mesh size is reduced until convergence, *i.e.* until the result does not change anymore, is obtained. It is also important to ensure realistic structural input parameters. For example, when simulating nanotriangles (*cf.* Chapter 4), a curvature radius at the edges had to be implemented, since just drawing a triangle leads to infinitely sharp tips that would cause unrealistic field enhancements and thus alter the spectral properties. Further critical parameters are the fitting parameters of the dielectric functions, the size of

the simulation volume, the number of PMLs, which can all lead to artifacts in the calculated spectra and near-field distributions if not respected properly.

3.2.2 Calculation of optical forces and load

Within the realm of this thesis, quantifying the optical forces exerted by focused laser beams on nanoparticles was crucial to analyze the experiments. Depending on the system, different computational methods had to be applied to calculate optical forces. This section starts with the *dipole approximation*, where nanoparticles are assumed to be point shaped dipoles leading to a computationally undemanding analytic solution. For larger anisotropic structures, the *T-Matrix method* is applied, where the scattering properties of an object are put as coefficients into a matrix. This method is non-analytic and therefore much more demanding. Finally, the *Maxwell Stress tensor* can be evaluated locally to determine local differences in the forces acting on the particle.

Dipole approximation

The most common and straightforward approach to calculate the optical forces that act on a plasmonic nanoparticle in a focused laser beam is by assuming the nanoparticle as an individual dipole. Using Equation 2.21 and Equation 2.22 derived in Section 2.1, one sees that gradient and scattering force depend on the complex polarizability α and the electric field from the laser beam. Using Equation 2.16, α can be expressed as a function of the scattering and extinction cross sections and the wave number k .

σ_{sca} and σ_{ext} are quantities relatively easily to determine, either by analytic Mie calculation in the case of spherical particles or FDTD calculations for complex geometries as described in Section 2.1.1 and Section 3.2.1, respectively. The electric field in a focused Gaussian laser beam, as it was used throughout the experiments performed in this thesis can be expressed in cylindrical coordinates as follows:²²

$$E(r, z) = E_0 \sqrt{\frac{2}{\pi}} \frac{\omega_0}{\omega} \exp\left[-\frac{r^2}{\omega^2}\right] \exp\left[i\left(k\left(\frac{r^2}{2R} + z\right) + \eta\right)\right]. \quad (3.4)$$

Here, E_0 denotes the maximum electric field in the laser focus, which can be calculated by

$$E_0 = \frac{\sqrt{2\mu_0 c_0 P}}{\omega_0}, \quad (3.5)$$

where P is the total laser power, μ_0 the permeability of free space and c_0 the speed of light in vacuum. ω_0 , the width of the beam in the focal plane and the width of the beam along the

z -axis $\omega(z)$ for a Gaussian beam are defined as follows:

$$\omega_0 = \frac{\lambda}{\pi NA}, \quad \omega(z) = \omega_0 \sqrt{1 + (z/z_0)}. \quad (3.6)$$

NA denotes the numerical aperture of the objective used to focus the laser as described before in Section 3.1.1 and z_0 the length, where the beam cross section doubles which is defined as $z_0 = (\pi\omega_0^2 n)/\lambda$. $R(z)$ and $\eta(z)$ are the radius of curvature of the wavefronts and the beam divergence parameter, respectively and can be written as

$$R(z) = z \left(1 + \left(\frac{z_0}{z} \right)^2 \right), \quad \eta(z) = \arctan \left(\frac{z_0}{z} \right). \quad (3.7)$$

Now, by putting Equation 3.4 into Equation 2.21 and Equation 2.22, one can calculate the gradient and scattering force fields. For the gradient force in z -direction $\mathbf{e}_z \cdot \langle \mathbf{F}_{\text{grad}}(r, z) \rangle$ and radial direction $\mathbf{e}_R \cdot \langle \mathbf{F}_{\text{grad}}(r, z) \rangle$, one obtains

$$\mathbf{e}_z \cdot \langle \mathbf{F}_{\text{grad}}(r, z) \rangle = -\frac{\varepsilon_0}{\pi} \alpha' E_0^2 \frac{z\omega_0^4}{z_0^2} \left(\frac{1}{\omega^4} - \frac{2r^2}{\omega^6} \right) \exp \left[-\frac{2r^2}{\omega^2} \right], \quad (3.8)$$

and

$$\mathbf{e}_R \cdot \langle \mathbf{F}_{\text{grad}}(r, z) \rangle = -\frac{2\varepsilon_0}{\pi} \alpha' E_0^2 \frac{r\omega_0^2}{\omega^4} \exp \left[-\frac{2r^2}{\omega^2} \right]. \quad (3.9)$$

The scattering force reads:

$$\mathbf{e}_z \cdot \langle \mathbf{F}_{\text{scat}}(r, z) \rangle = \frac{\varepsilon_0}{\pi} \alpha'' E_0^2 \frac{\omega_0^2}{\omega^2} \left(k \left(1 - \frac{r^2(z^2 - z_0^2)}{2(z^2 + z_0^2)} \right) + \frac{\omega_0^2}{z_0\omega_0^2} \right) \exp \left[-\frac{2r^2}{\omega^2} \right], \quad (3.10)$$

and

$$\mathbf{e}_R \cdot \langle \mathbf{F}_{\text{scat}}(r, z) \rangle = \frac{\varepsilon_0}{\pi} \alpha'' E_0^2 \frac{r\omega_0^2}{\omega^2} \frac{k}{R} \exp \left[-\frac{2r^2}{\omega^2} \right]. \quad (3.11)$$

This set of equations was implemented in Wolfram Mathematica 10.3 (Wolfram Research Inc., USA). It should be noted that this solution represents an idealistic case neglecting lens errors, effects of the gold nanoparticle itself on the electric field distribution and inhomogeneities in the medium, which would alter the Gaussian distribution. Also, since the beam is truncated by the back aperture of the objective, diffraction patterns appear in experiments that are not considered here.¹¹⁶ Furthermore, for increasing particle diameters, the assumptions made for the dipolar polarizability do not hold anymore. Nevertheless, the dipole approach provides a computationally inexpensive tool to calculate optical forces on spherical plasmonic nanoparticles up to diameters below 100 nm¹¹⁷ and can even be used to approximate the forces on nonspherical particles.^{32,22}

T-Matrix Method

Another widely used tool to calculate scattering, and hence optical forces on colloidal particles is the so called T-matrix, or transition Matrix approach introduced in 1965 by P.C. Waterman.^{118,119,120} A major advantage of this method is its universal applicability to any star domain shaped geometry. It can also be applied to arbitrary sized particles, where the dipolar approximation does not hold anymore.

The relation between the scattered field E_{out} and the incident field E_{in} is defined through the T-Matrix where the scatterer is placed at the origin of the coordinate system. Within the T-matrix approach, these fields are expressed in vector spherical wave functions $\mathbf{M}_{mn}^{1,2}$ and $\mathbf{N}_{mn}^{1,2,121}$:

$$E_{\text{out}} = \sum_{n=1}^{\infty} \sum_{m=-n}^n p_{nm} \mathbf{M}_{mn}^1(k\mathbf{r}) + q_{nm} \mathbf{N}_{mn}^1(k\mathbf{r}), \quad (3.12)$$

$$E_{\text{in}} = \sum_{n=1}^{\infty} \sum_{m=-n}^n a_{nm} \mathbf{M}_{mn}^2(k\mathbf{r}) + b_{nm} \mathbf{N}_{mn}^2(k\mathbf{r}), \quad (3.13)$$

This set of basis functions fulfills the requirement of spanning the space of solutions of the Maxwell equations. The exact definitions of $\mathbf{M}_{mn}^{1,2}$ and $\mathbf{N}_{mn}^{1,2}$ can be looked up in literature.^{121,122} The incident and scattered fields are then related through their expansion coefficients a_{nm} , b_{nm} , p_{nm} and q_{nm} by means of the T-Matrix in compact matrix notation:

$$\begin{bmatrix} \mathbf{p} \\ \mathbf{q} \end{bmatrix} = \begin{bmatrix} T_{11} & T_{12} \\ T_{21} & T_{22} \end{bmatrix} \begin{bmatrix} \mathbf{a} \\ \mathbf{b} \end{bmatrix} \quad (3.14)$$

In practice, for the calculations, the sums have to be truncated at a finite n_{max} , thus marking the number of expansion coefficients. Within the realm of this thesis, convergence was found for 30 expansion coefficients in the case of spherical particles, and 40 expansion coefficients in the case of nonspherical particles. The values of the T-Matrix depend on the size and shape of the nanoparticle and the incident wavelength. For spherical particles, the T-matrix is diagonal, which corresponds to the generalized Lorenz-Mie theory. For nonspherical particles, the T-Matrix becomes nondiagonal, leading to more expensive calculations. However, once calculated for a given particle at a given wavelength, the T-Matrix is universally applicable to calculate the scattered field for any incident field. This is in particular useful for the calculation of optical force fields, since the force has to be calculated for each position in a focused laser beam. The elements of the T-Matrix as well as the expansion coefficients were calculated according to Nieminen *et al.*^{123,124} using a least-squares overdetermined point-matching method.

Hence, by calculating the expansion coefficients of the incident field and the T-Matrix the entire scattering problem can be solved. From the relationship between incident and scattered field one can deduce the optical force, which is given for a beam propagating in z-direction

at the focal plane ($z = 0$):^{122,125}

$$F_z = \frac{2n_{\text{med}}}{c_0} \sum_{n=1}^{\infty} \sum_{m=-n}^n \frac{m}{n(n+1)} \text{Re} (a_{nm}^* b_{nm} - p_{nm}^* q_{nm}) - \frac{1}{n+1} \left[\frac{n(n+2)(n-m+1)(n+m+1)}{(2n+1)(2n+3)} \right]^{\frac{1}{2}} \times \text{Re} (a_{nm} a_{n+1,m}^* + b_{nm} b_{n+1,m}^* - p_{nm} p_{n+1,m}^* - q_{nm} q_{n+1,m}^*).$$
(3.15)

Here, n_{med} denotes the refractive index of the surrounding medium. In order to calculate the optical force for different points in space, one has to transform either the beam centered or the particle centered coordinate system. Usually, the beam centered coordinate system is transformed, since here only a vector rather than a Matrix has to be transformed. The linear transformation is split into a rotation followed by a translation. The rotation reads:¹²⁵

$$\mathbf{a} = \mathbf{R}\mathbf{a}_o, \quad \mathbf{b} = \mathbf{R}\mathbf{b}_o, \quad (3.16)$$

where \mathbf{R} is the rotation matrix and \mathbf{a}_o and \mathbf{b}_o the initial expansion coefficients. \mathbf{R} is calculated using the algorithm from Choi *et al.*¹²⁶ The subsequent translational transformation can be written as follows:

$$\mathbf{a} = \mathbf{A}\mathbf{a}_o + \mathbf{B}\mathbf{b}_o, \quad \mathbf{b} = \mathbf{B}\mathbf{a}_o + \mathbf{A}\mathbf{b}_o. \quad (3.17)$$

The translation matrices \mathbf{A} and \mathbf{B} are calculated using an algorithm developed by Videen.¹²⁷ All above mentioned calculations are implemented in the *Optical forces toolbox* in MATLAB 2014b (The MathWorks Inc., USA) as published by Nieminen *et al.*¹²² Using Equation 3.16 Equation 3.17 and Equation 3.15 the entire force field around a particle in a focused laser beam can be calculated. The required input parameters are n_{med} , the size and shape of the particle, its dielectric function, the laser wavelength and polarization as well as the NA . In the case of nonspherical dielectric particles, the calculation precision had to be increased to 80 digits in order to obtain convergence. This was implemented in MATLAB using the *Advanpix Multiprecision Computing Toolbox* (Advanpix LLC, Japan).¹²⁸ To showcase the capability of the *Optical forces toolbox*, several exemplary force field calculations are shown in Figure 3.6, namely a 1 μm silica sphere, a 125 nm diameter gold sphere and a 100 \times 1000 nm silica cylinder. All three shapes are calculated for a laser power of 100 mW and an NA of one in water for two different wavelengths that are 532 nm and 1064 nm. While the force field of the dielectric particles does not change significantly with the laser wavelength, the gold nanoparticle behaves completely different at 532 nm and at 1064 nm, as described in Section 2.1.

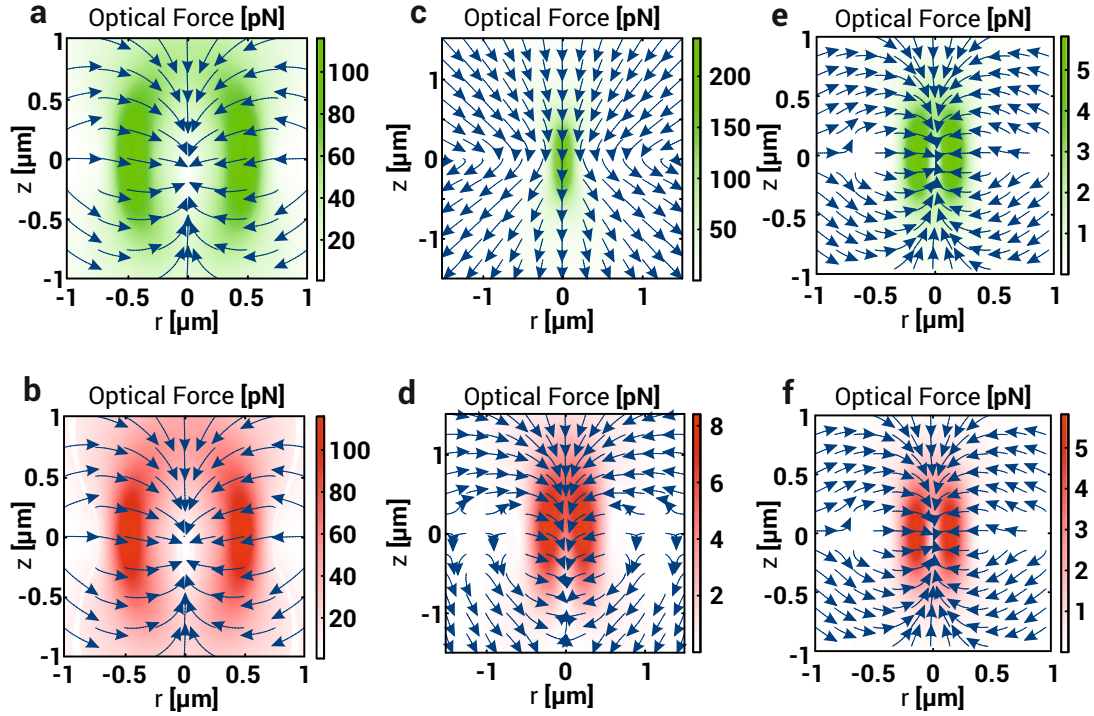


Figure 3.6 – Optical forces calculated with the T-Matrix method. Optical forces acting on a silica sphere ($d = 1 \mu\text{m}$) at a laser power of 100 mW and $NA = 1$ at (a) 532 nm and (b) 1064 nm. Optical forces acting on a gold nanoparticle ($d = 150 \text{ nm}$) at a laser power of 100 mW and $NA = 1$ at (c) 532 nm and (d) 1064 nm. Optical forces acting on a silica cylinder ($h = 1000 \text{ nm}$, $d = 100 \text{ nm}$) at a laser power of 100 mW and $NA = 1$ at (e) 532 nm and (f) 1064 nm.

Maxwell stress tensor method

The numerical methods described in the previous sections are useful tools to calculate the total force impacting nanoparticles in a focused laser beam. However, the optical force does not act isotropically on a nanoparticle. Especially for nonspherical particles, this anisotropy can be quite significant. The local optical force acting on a volume element of a nanoparticle depends on the amplitude of the electric field \mathbf{E} and the magnetic field \mathbf{B} within the particle.³³ As described before, FDTD provides relatively easy access to the field distributions within a nanoparticle. The relation between mechanical forces and the electromagnetic field is governed through the *Maxwell stress tensor* that describes the force per unit area on the surface. In this formalism, the total force acting on a nanoparticle is given for the static case as:¹²⁹

$$\mathbf{F}_{opt} = \int_S \mathbf{T} \cdot \mathbf{n} \, dS, \quad (3.18)$$

where S is the particle surface and \mathbf{n} the unit outward normal vector. The Maxwell stress tensor itself is defined as:¹²⁹

$$T_{ij} \equiv \varepsilon_0 \left(E_i E_j - \frac{1}{2} \delta_{ij} E^2 \right) + \frac{1}{\mu_0} \left(B_i B_j - \frac{1}{2} \delta_{ij} B^2 \right). \quad (3.19)$$

Since the field distribution data from FDTD is spatially resolved, one can calculate an optical load $q(x)$ by integrating around slices of the nanoparticle. For a nanorod exposed to light propagating in z -direction this reads due to cylindrical symmetry:³³

$$q(x) = \int_0^{2\pi} \mathbf{e}_z \cdot \mathbf{T} \cdot \mathbf{n} r d\theta. \quad (3.20)$$

The optical load in x and y direction are calculated accordingly. Hence, one can calculate the effective force per nanometer acting on a nanorod for all three spatial directions. In this work, the Maxwell stress tensor was calculated using the built in module in Lumerical FDTD with a lateral resolution of 0.25 nm. Here, a built-in Gaussian shaped light source was used, which allowed to use the correct input parameters for the incident field distribution by choosing the NA and field amplitude used in the experiments. However, the main disadvantage of this method is that calculating force fields is computationally extremely demanding, since each spatial position has to be calculated independently unlike in the methods presented previously. Hence, this method is only used to evaluate the optical load acting on particles in the laser focus and not for force fields.

3.2.3 Simulations of heat transport and hydrodynamic forces

As introduced in Equation 2.30, the temperature increase around an individual spherical nanoparticle in an isotropic environment can be easily calculated. However, in the realm of this thesis, either the environment is anisotropic or the particles are nonspherical or even both. Additionally, the temperature dependence of the relevant material parameters make an analytic calculation impossible in most cases. However, there are numerous methods to solve Equation 2.29, the heat transfer equation, numerically. Here the *Finite-elements method* implemented in COMSOL Multiphysics 5.2a (COMSOL, Sweden) was applied, a common solver for complex differential equations. Briefly, the method divides the simulation volume into many small objects, the finite elements, of simple shape (Figure 3.7a). Here, the element size is the smallest at the interface between the heat source and the surrounding medium. The differential equations for those elements can then be integrated numerically and their solutions linked through boundary conditions.¹³⁰

Since a nanoparticle reaches its thermal equilibrium within nanoseconds (cf. Section 2.4), the time dependence was neglected and only the static case of the heat transfer equation was solved. Apart from the material parameters and the geometry, the only input parameter used is the volumetric heat power density Q_0 , which is assumed to be constant within the boundaries of the plasmonic particles. Since Q_0 depends on the amount of absorbed light it can be calculated from the absorption cross section σ_{abs} , the laser intensity I_L and the beam diameter, which is determined by the NA . In particular, the absorbed laser power is calculated by integrating the Gaussian distribution of the focused laser spot within the boundaries of σ_{abs} and then divided through the volume of the nanoparticle in order to obtain Q_0 .

As an example, Figure 3.7b shows the heat distribution of an 80 nm spherical gold nanoparticle illuminated with a focused 532 nm laser at 1 mW using a $NA = 1$ water immersion objective on a glass substrate calculated with COMSOL Multiphysics.

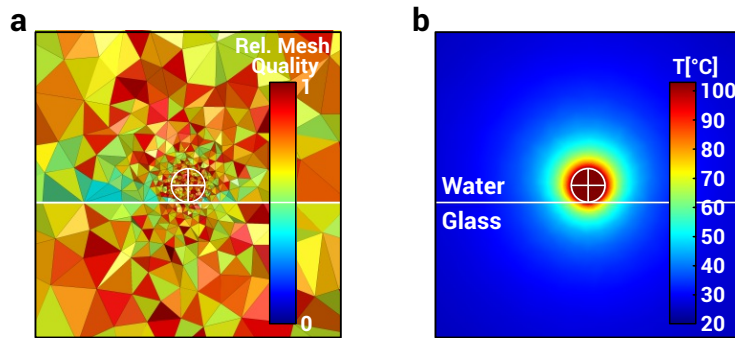


Figure 3.7 – Calculation of the temperature increase due to plasmonic heating. (a) Mesh grid used for the simulation calculated by COMSOL. The grid gets finer at the gold-water interface to account for the change in thermal conductivity. (b) Temperature distribution around a spherical gold nanoparticle ($d = 80$ nm) in water on a glass substrate heated with a 532 nm laser at 1 mW.

Calculation of hydrodynamic forces

Within the realm of optical printing, plasmonic nanoparticles not only experience heating but also hydrodynamic drag forces while traveling through the liquid. Those forces are governed by the Navier Stokes equation (Equation 2.24) under the assumption of mass conservation as introduced in Section 2.1.1. As the case for the heat transfer equations they are a set of coupled partial differential equations. Hence, also here FEM is a feasible tool to solve such problems. Furthermore, since the density $\rho(T)$ and the viscosity $\mu(T)$ from Equation 2.24 are temperature dependent, an iterative approach is applied to couple heat transfer and hydrodynamics in order to obtain solutions as realistic as possible. Here, to attain convergence, the temperature of the plasmonic structure was fixed to the value obtained beforehand from pure heat conduction. Furthermore, an uniform time-independent laminar fluid flow was assumed. Hence, by solving the differential equation system, one can obtain the pressure acting on the surface of the

nanostructure at a given fluid flow velocity. Integrating the pressure over the surface of the entire nanostructure then yields the total fluidic force acting on the particle. By comparing this to the optical force calculated previously, one can deduce the propagation velocity of the nanoparticle during optical printing assuming a force equilibrium between optical and fluidic forces. Furthermore, by analyzing the pressure distribution in different spatial directions, shear forces can be discovered.

3.3 Cell culture and fixation

For nanoparticle injection experiments (cf. Chapter 6), Chinese hamster ovary (CHO) cells were cultivated. Their high yield for protein expression in combination with their relatively facile handling made them the most used mammalian cell line in biomanufacturing.¹³¹ Furthermore, they are growing while being attached to a glass dish, which makes them ideal samples for microscopy experiments.

The cell line (ATCC® CCL-61™) used within the experiments of this thesis was purchased from ATCC, USA and stored in the liquid nitrogen vapor phase before usage. To prepare them for subculture, they were thawed by placing the vial containing the cells into a 37 °C water bath under gentle swirling. Before opening the vial it was sterilized with 70% ethanol. Subsequently, the cells were dropped on a 75 cm² culture flask containing 14 ml of Ham's F-12 medium with 10% fetal calf serum (FCS) and incubated over night in a humidified 5% CO₂ atmosphere at 37 °C. Afterwards, the medium was replaced by fresh warm growth medium and incubated for another 48 h. Sub culturing was then conducted, once the cell confluence reached 80%.

For this purpose, the old medium was discarded and the cell layer washed with 1 ml phosphate buffered saline (PBS) to remove the serum residues. Subsequently, 3 ml of a 0.25% Trypsin / 0.53 mM Ethylenediaminetetraacetic acid (EDTA) mixture were added to detach the cells from the surface. After 3 to 5 min, 7 ml of growth medium were added. The cell suspension was then centrifuged at 1000 rpm for 3 min and the supernatant containing the Trypsin/EDTA removed subsequently. 5 ml of prewarmed growth medium were then added to re-suspend the cells. For cell maintenance, 3 ml of the cell suspension were diluted with 12 ml of complete growth medium, transferred into a culture flask and put in the incubator. In order to prepare the cells for experiments, they were passaged 48 h before into a glass bottom dish with an imprinted 50 µm relocation grid (µ-Dish 35 mm, High Grid-50 Glass Bottom, ibidi GmbH, Germany) diluted with cell medium at a ratio of 1:5. The medium was then changed to Leibovitz's L-15 medium (LM) with L-Glutamine.

Cell fixation

For electron microscopy the cells had to be prepared, in a way to cope with the ultra high vacuum inside the microscopy chamber. In this thesis, a fixation protocol published by Bray *et al.*¹³² was applied. This treatment prevents decomposition of the cells preserving the morphology of the cell. The protocol was executed as follows:

The sample was washed in Sorensen buffer (72.6 ml of 0.133 M Na_2HPO_4 + 27.4 ml of 0.133 M KH_2PO_4) for 2 min. Subsequently, the cells were washed with a 2.5% Glutaraldehyde solution (1 ml Glutaraldehyde + 40 ml Sorensen buffer) for 30 min. This step killed the cells and thus prevented any changes of the sample structure. Then the sample was washed first in Sorensen buffer and ultrapure water for 10 min each and three more times in ultrapure water for 5 min. Afterwards, the cells were washed in a series of ethanol concentrations (30%, 50%, 75%, 95%, 100%) for 10 min each to gradually replace the water inside the cells. Finally, the sample was washed two times with Hexamethyldisilazane (HDMS) for 15 min. After removing the HDMS and letting the sample dry over night, it was ready to be investigated by electron microscopy. All chemicals were purchased from Sigma-Aldrich Chemie GmbH, Germany. Washing was performed by adding 1 ml of the respective chemical to the cell sample.

Chapter 4

Spectral sorting of single plasmonic nanoparticles using optical forces

As introduced in Section 2.1.1 and Section 2.2, plasmonic nanoparticles are highly susceptible to electromagnetic radiation in the visible and NIR regime. By acting as antennas their absorption and scattering interaction cross section is much larger than their actual physical size. The resonance frequency of these antennas is determined by their material and shape. Absorption as well as scattering of light leads to a momentum transfer from the photons to the particle. This momentum transfer, also termed scattering force, is proportional to the extinction cross section (cf. Equation 2.23). In this chapter, this feature is exploited to optically sort plasmonic particles by their shape and hence their plasmon resonance. This renders it possible to elucidate the dynamics of a synthesis that has been the subject of considerable debate in the last two decades. The results presented in this chapter have been published in *ACS Nano* as "Optical Nanoparticle Sorting Elucidates Synthesis of Plasmonic Nanotriangles" by M.A. Huergo, C.M. Maier, M.F. Castez, C. Vericat, S. Nedev, R.C. Salvarezza, A.S. Urban and J. Feldmann in 2016.¹³³

4.1 Context: The Reduction of Au (III) with sulfide species

Plasmonic particles featuring resonances in the NIR region of the spectrum are of special interest for biomedical applications such as imaging or cancer therapy due to the biological window of tissue at wavelengths between 650 nm and 1400 nm where light absorption becomes minimal.^{38,134}

Several years ago a particular synthesis has drawn considerable interest, namely the reduction of Au (III) with sodium sulfide.^{135,136} In brief, 10 ml of a 1 mM HAuCl_4 solution are mixed with 12 ml of freshly prepared 1 mM Na_2S . After 2 min, another 2 ml of the Na_2S are added bringing the total molar S/Au ratio to 0.65. The extinction spectrum of this synthesis features two peaks, one around 520 nm and a second one in the NIR region. The latter peak undergoes a redshift during the first minutes. After reaching its maximum wavelength around 900 nm to 1000 nm, the peak undergoes a blueshift and eventually merges with the other peak.

Initial reports attributed this behavior to the formation of core shell particles, with an Au_2S core and a gold shell.^{135,136} This initial assumption was made upon the appearance of Bragg reflections assigned as the $\langle 111 \rangle$ and $\langle 220 \rangle$ planes of Au_2S . In this model, the dynamics of the second plasmon peak are explained by the gradual thickening of the gold shell around the gold-sulfide core. However, those studies lacked direct structural evidence of the claimed core-shell particles.

A few years later, this model was challenged by identifying gold nanoparticle aggregates as the origin of the NIR spectral peak.^{137,138} This claim was backed by X-ray data not exhibiting any features characteristic for Au_2S , as well as spectral hole burning not yielding any significant change in the nanoparticles' morphology in transmission electron microscopy (TEM) analysis. However, no optical spectral data of individual gold nanoparticle clusters was provided to unambiguously link the claimed aggregates to the NIR peak. Furthermore, this model does not provide a conclusive explanation for the blueshift.

Shortly after, this model also was challenged as other authors suggested the nanotriangles visible in TEM pictures, which were deemed insignificant by the other groups,¹³⁸ as the particle species responsible for the NIR peak.^{139,140} However no experimental proof was provided to sustain this claim. They also remained vague in explaining the red- and blueshift attributing these shifts to either morphological changes of the triangles or variations in the surface potential due to the adsorption of sulfide ions, thus lacking understanding on the mechanism. Also more recent publications did not analyze the origin of the NIR plasmon peak, albeit considering the triangular shaped particles as the responsible particle species.^{141,142}

Nevertheless, despite all the doubts presented before, the core shell model was still widely used,^{143,144,145} partly also because none of the studies mentioned could provide unambiguous proof for the origin of the NIR plasmon peak. As mentioned in Section 2.2, the emergence of a

peak in the NIR in a solution of plasmonic particles can have many different origins. Hence, an approach is needed that correlates the spectral features with a particular particle species.

4.2 Properties of the synthesis

As described, the reduction of Au(III) with sodium sulfide leads to the appearance of two extinction peaks, one at around 530 nm and another one in the NIR region of the spectrum. Figure 4.1 shows the time resolved spectrum recorded within the experiments of this thesis by letting the synthesis evolve in a cuvette within an UV-Vis spectrophotometer (cf. Section 3.1.3). Initially, the spectrum exhibits a strong signal at 527 nm with a shoulder on the short wavelength side and a very small peak at 820 nm. Over the course of the synthesis, the first peak only shifts very slightly to 533 nm while growing in intensity. The NIR peak on the other hand undergoes a much more dramatic change over time. First it shifts further into the NIR within approximately 20 min up to a maximum wavelength of 1000 nm, where the peak remains roughly the same for 10 min and then starts to shift to the blue again. At the same time, it first increases in intensity and later decreases again. Although the exact timescales and

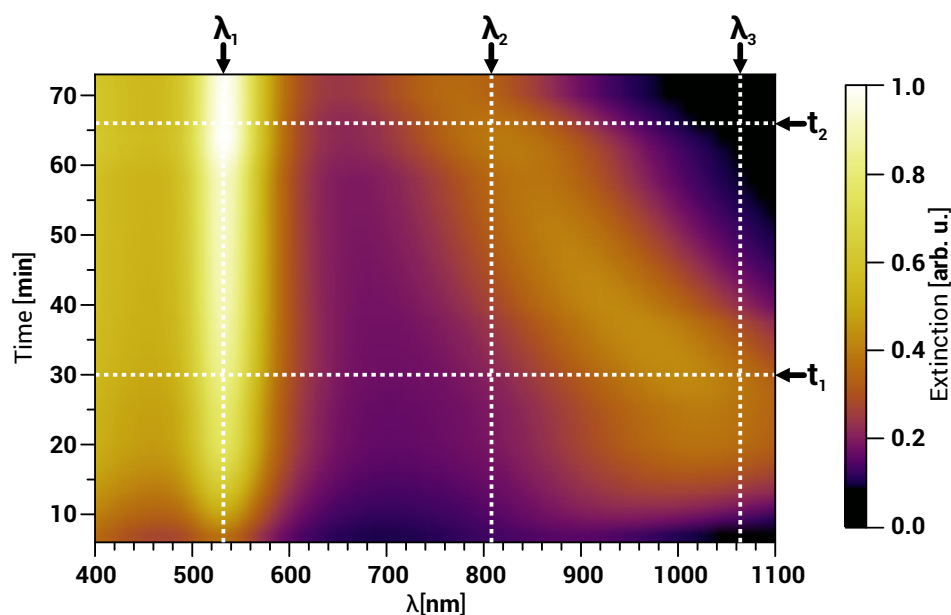


Figure 4.1 – Temporal evolution of the extinction spectrum during the reduction of gold chloride with Na_2S . The extinction spectrum features two resonances, one in the green region of the spectrum and another one in the NIR. The peak in the green region only undergoes a small redshift while growing in intensity. The NIR peak on the other hand is growing in intensity during the first 30 min while shifting to the red to a maximum wavelength of about 1000 nm. Afterwards, the spectral dynamic reverts and a blueshift is observable. The synthesis was arrested by adding Na_2S at times t_1 and t_2 , at the maximum redshift (1000 nm) and when the second peak hits the biological window of tissue at 800 nm, respectively. Laser printing was performed at wavelengths $\lambda_1 = 532$ nm, $\lambda_2 = 808$ nm and $\lambda_3 = 1064$ nm.

maximum red shift can vary when running the synthesis several times, the general behavior is very much reproducible and characteristic for this synthesis.

The synthesis can be arrested at any time by adding excess Na_2S allowing a precise tuning of the NIR plasmon peak to any desired position. To shed light on the ongoing debate on the origin of the NIR peak, the synthesis was arrested at two distinct temporal points, namely the point of the maximum redshift t_1 , and later during the blueshift at around $\lambda = 800$ nm, where the peak is at an optimal position for biological applications (t_2). The latter one was usually the point where the synthesis was discussed in literature.^{135,136,137,138,139,140,143}

Figure 4.2a and b show exemplary TEM images of the nanoparticles at synthesis times t_1 and t_2 , respectively. As one can see, the solution is relatively polydisperse. Spherical nanoparticles with diameters ranging from 15 nm to 40 nm are found as well as very small (~5 nm) spherical nanoparticles. The latter ones were subsequently removed *via* selective centrifugation, which did not change the total spectrum significantly. In the resulting sample 75% of all particles were spherical. The remaining 25% were mostly of triangular shape in both samples with some hexagonal particles and nanorods also present. At t_1 the triangles were found to be equilateral

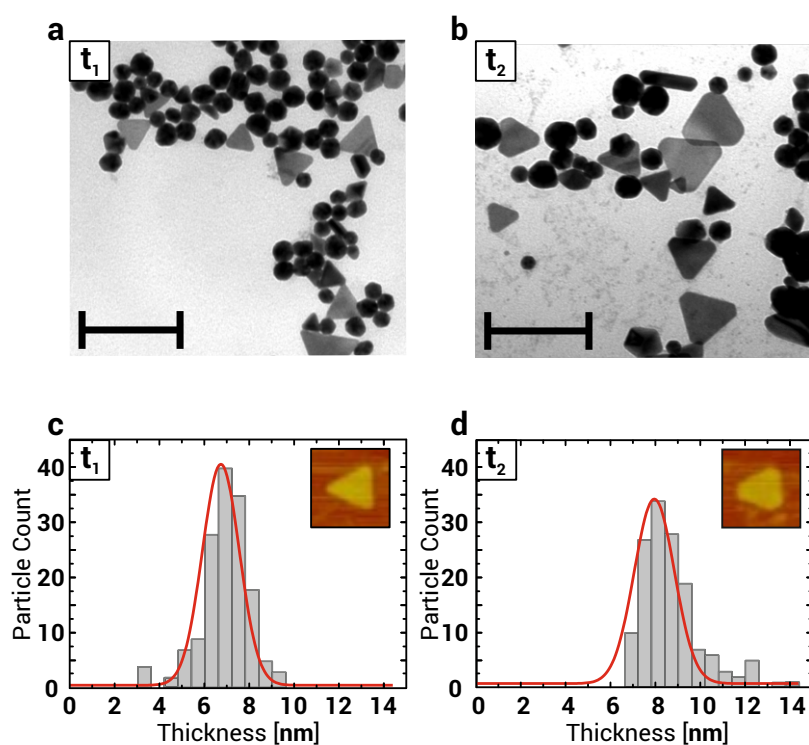


Figure 4.2 – Transmission electron microscope images and AFM analysis of the nanoparticles at synthesis times t_1 and t_2 . For both synthesis times t_1 (a) and t_2 (b) the nanoparticle morphologies are very polydisperse. Small and large spherical nanoparticles can be found among triangles, rods and hexagons making an assignment of a particular nanoparticle species to a spectral peak difficult. The scale bar is 100 nm. The statistical analysis of AFM images reveals an average thickness of the triangles of (6.8 ± 0.7) nm at t_1 (c) and (9 ± 1) nm at t_2 (d). The size of the inset is 150 nm

with side lengths of 60 nm to 100 nm and sharp tips. At t_2 they looked similar, however their tips appeared either rounded or clipped.

When looking closely at the TEM images, one can see that the triangular shaped particles show much lower contrast than the spherical ones, which is a sign for the triangles being very thin. The respective thickness of the triangles is crucial for their optical properties. Hence, a statistical analysis of a large quantity of sharp triangles at t_1 and truncated triangles at t_2 was performed using atomic force microscopy (AFM) (Figure 4.2c, d). This allowed to determine the average thickness of the triangles at t_1 and t_2 which was found to be (6.8 ± 0.7) nm and (9 ± 1) nm, respectively. This conformational change in the TEM and AFM pictures already gives a first hint that the triangles might be responsible for the temporal change of the NIR spectral peak. In order to prove this hypothesis an approach is needed that separates the particles by their plasmon resonance to assign spectral features to certain morphologies.

4.3 Strategy: Use optical force to sort particles by their plasmon resonance

As one can see from Equation 2.23 the scattering force depends linearly on the extinction cross section of the particle. Hence, the scattering force that acts on a nanoparticle in a focused laser beam depends directly on the particle morphology. Optical printing of single plasmonic nanoparticles, as introduced in Section 2.1.2, makes use of the strong scattering force acting on plasmonic particles, when hitting them with a focused laser beam at their resonance.²⁹ However, when the laser is detuned from the plasmon resonance, the scattering forces decreases rapidly and is not sufficient anymore to bind them onto a substrate.

Figure 4.3a shows the calculated extinction spectra of the three different gold nanoparticles found, namely a sphere, a truncated and a sharp triangle. Their plasmon resonances resemble the spectra found in Figure 4.1 (528 nm, 807 nm and 1011 nm). Due to the narrow spectral linewidth of both triangular particles, which stems from reduced interband damping,¹⁰⁷ the peaks of the extinction cross sections do not overlap significantly. This facilitates their selective excitation with a narrow spectral resolution by using lasers that are tuned to their respective resonances.

For successful optical printing, the optical force has to overcome the surface potential. This potential has two contributions, namely the attractive van der Waals force and an electrostatic force resulting from a polarity of the surface and the charge of the nanoparticles. Plasmonic nanoparticles are usually stabilized by putting charged molecules on their surface. Depending on the sign of charge and surface polarity, the electrostatic force can be either attractive or

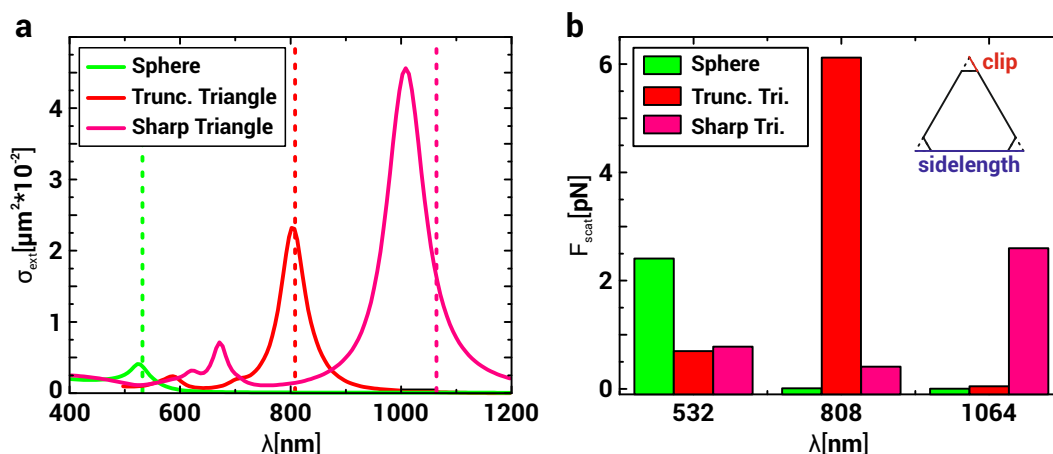


Figure 4.3 – Wavelength dependence of optical scattering forces for different plasmonic particles. (a) Extinction cross sections of a single gold sphere of 40 nm diameter, a triangle with truncated tips and a triangle with sharp tips. The thicknesses of the truncated and the sharp triangles were 8 nm and 7 nm, respectively. The side lengths were 80 nm and 100 nm, with the tips of the truncated triangle being clipped by 10 nm. The dashed lines represent the three different lasers that were applied to exert optical forces on the nanoparticles. (b) Optical scattering force calculated from Equation 2.23 acting on the three aforementioned particles at wavelengths 532 nm, 808 nm and 1064 nm and a laser power of 10 mW at a numerical aperture of 1. For each wavelength only one species of particles experiences a significant scattering force, which allows to tune the laser intensity so that only the resonant particle species gets printed onto a substrate.

repulsive. The potential therefore reads:

$$V_{\text{tot}} = V_{\text{vdW}} + V_{\text{E}}. \quad (4.1)$$

In order to avoid random deposition which occurs for a total attractive potential, hence $V_{\text{tot}} < 0$, one usually chooses the surface charges of substrate and particle to be of the same sign.²⁹ Hence, for a successful printing event, the optical force acting on the particle has to overcome V_{tot} . This leads to a threshold of a minimum optical force for optical printing.⁶⁶ The exact value depends on the size and charge of the particle as well as the substrate.

Within the framework of this thesis, printing was done from water solution onto a glass substrate. This interface exhibits a negative surface charge due to the dissociation of terminal silanol groups.¹⁴⁶ The particles considered in this chapter are covered by a layer of sulfur species¹⁴⁷ exhibiting an overall negative surface charge¹⁴⁸ *i.e.* $V_{\text{E}} > 0$. For this reason, the observed amount of random deposition is low, leading to very controllable printing conditions. Figure 4.3b shows the optical force acting on the three different particles for the laser wavelengths $\lambda_1 = 532$ nm, $\lambda_2 = 808$ nm and $\lambda_3 = 1064$ nm. An arbitrary laser power of 10 mW was assumed for all wavelengths for this calculation.

As one can see, in all three cases the forces exerted on the particles resonant to the respective laser line are considerably higher than on the off-resonant particles. Hence, by

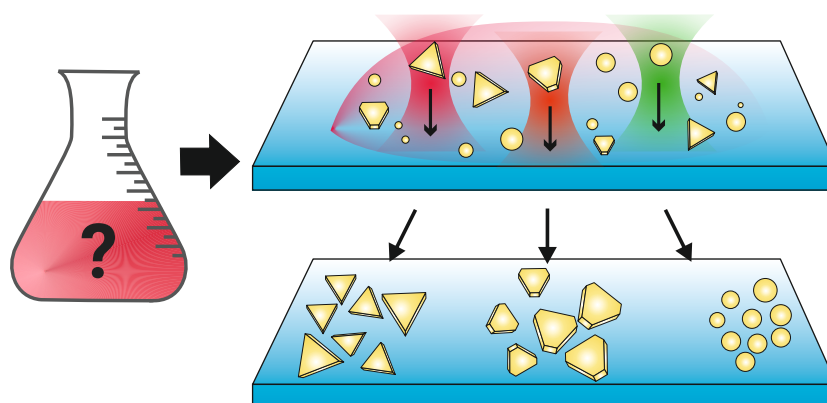


Figure 4.4 – Optical sorting of plasmonic nanoparticles. A droplet of a polydisperse solution of gold nanoparticles is put onto a glass substrate. Applying three different laser wavelengths allows to sort the particles by their plasmon resonance, exhibiting the morphology responsible for a peak in the bulk spectrum of the entire solution.

choosing the right laser wavelength and intensity, only one particle species experiences enough scattering force to eventually get deposited on the substrate. This means that particles are selectively printed with regards to their shape.

Figure 4.4 shows a sketch of the experimental approach. Assuming a polydisperse solution formed by the aforementioned particles, applying lasers of three different wavelengths allows to sort the particles by their resonances on a substrate. This approach can in principle be applied to any arbitrary polydisperse plasmonic particle solution if the resonances of the individual particles are sharp enough.

Other approaches have been published that also rely on exerting optical forces to sort different species of plasmonic nanoparticles in a solution in bulk¹⁴⁹ as well as for single nanoparticles.¹⁵⁰ However, those approaches lack the immediate deposition of the sorted particles on a substrate making a subsequent determination of the exact morphology impossible.

Applying the nanoparticle sorting to the synthesis in question

To realize the approach of sorting nanoparticles with optical forces, three lasers with the aforementioned wavelengths λ_1 , λ_2 and λ_3 were coupled into a dark field microscope (cf. Section 3.1.1). A diluted droplet of the nanoparticle solution was placed onto a glass cover slide. By using a water dipping objective, the lasers were focused onto the substrate and the printing events could be imaged in real time. This allowed to analyze the nanoparticle solution at any intersection between the $t_{1,2}$ and $\lambda_{1,2,3}$ lines as it is illustrated in Figure 4.1.

Figure 4.5a illustrates the result when sorting the synthesis arrested at $t = t_1$. Here, as expected and also as reported in literature, printing close to the peak in the green region using a laser at λ_1 yielded exclusively spherical nanoparticles (Figure 4.5b bottom row). Printing at λ_2 yielded only very few printing events requiring several minutes for every particle, which

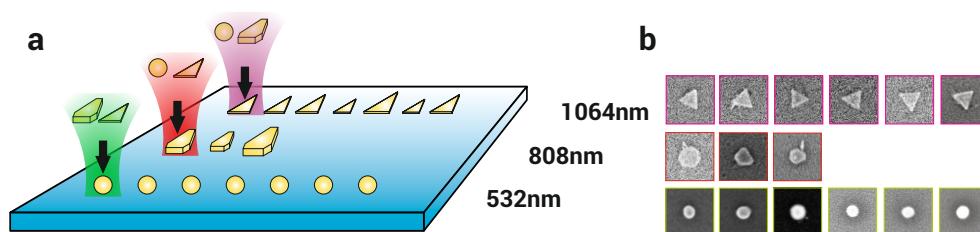


Figure 4.5 – Result of the nanoparticle sorting process for the synthesis arrested at t_1 . (a) Sketch of the sorting experiment. At 532 nm only spherical particles were printed, whereas at 1064 nm only sharp tipped triangular particles were found with side lengths of around 70 nm. At 808 nm only very few particles were printed that were either truncated or rounded triangles. (b) SEM pictures of the particles deposited *via* optical nanoparticle sorting. The size of the inset is 200 nm.

was expectable since the intensity in Figure 4.1 at the intersection between t_1 and λ_2 is very low. This indicates that the quantity of particles present in the solution here is very low. In the SEM, the printed particles were found to be truncated or rounded triangles (Figure 4.5b middle). Since λ_3 lied outside the range of the detector, the printing events could not be detected visually anymore. Hence, the sample was moved continuously in order to prevent unnecessary heating of the nanoparticles. Subsequent SEM analysis showed that all of the particles deposited in this region were sharp tipped triangles with an average side length of 70 nm (Figure 4.5b top).

When examining the sample arrested at t_2 , a different particle distribution was observed (Figure 4.6). Like at t_1 , only spherical nanoparticles were printed at λ_1 . However, analyzing at λ_2 revealed a large quantity of exclusively truncated and rounded triangles (Figure 4.6b). No particles were found at λ_3 , which is not surprising, since the overall extinction spectrum is almost zero there. It is important to point out that spherical particles were found at neither λ_2 nor λ_3 in both samples. Overall, this newly introduced approach proved to be highly specific, since at each wavelength only one particle species was printed. This could also be seen In the DFM, as only such particles were printed, where the plasmon resonance matched the incident laser wavelength.

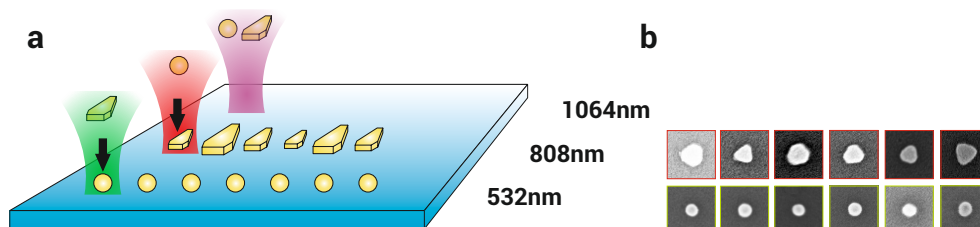


Figure 4.6 – Result of the nanoparticle sorting process for the synthesis arrested at t_2 . (a) Like in the sample of t_1 , only spherical particles were printed at 532 nm. At 808 nm the particles printed were either truncated or rounded triangles. At 1064 nm no particles were found at all. (b) SEM pictures of the particles deposited *via* optical nanoparticle sorting. The box size is 200 nm.

4.4 Optical and numerical analysis

In order to fully understand the correlation between the optical properties and the morphology of the nanotriangles and to exclude any other contributions to the total UV-Vis spectrum (cf. Figure 4.1) a comprehensive analysis of the printed nanoparticles is required.

At this point, it has to be considered if the applied laser powers can potentially change the morphology of the nanoparticles. As mentioned earlier in Section 2.4, illuminating plasmonic nanoparticles with a laser always comes with significant heating due to the portion of light absorbed by the particles. Hence, the particle temperatures were calculated by finite element calculations using the absorption cross section calculated previously for sharp triangles at 1064 nm and 808 nm (Figure 4.7). Here, a laser power of 15 mW was assumed which was the maximum laser power applied during the experiments.

The calculations showed that the temperature reaches up to 245 °C for sharp and 65 °C for truncated triangles. Despite melting point depression (cf. Section 2.5), this is well below the melting temperature of gold nanostructures of comparable sizes.^{78,79} Experiments carried out with nanorods suggest that particles can be printed even at maximum temperatures close to the bulk melting point before observing deformations.³² Furthermore, experiments have shown that the morphology of nanorods changed only after one hour at 250 °C when heated thermally and that rods stayed stable up to 700 °C when heated by a femtosecond laser source.¹⁵¹ Hence,

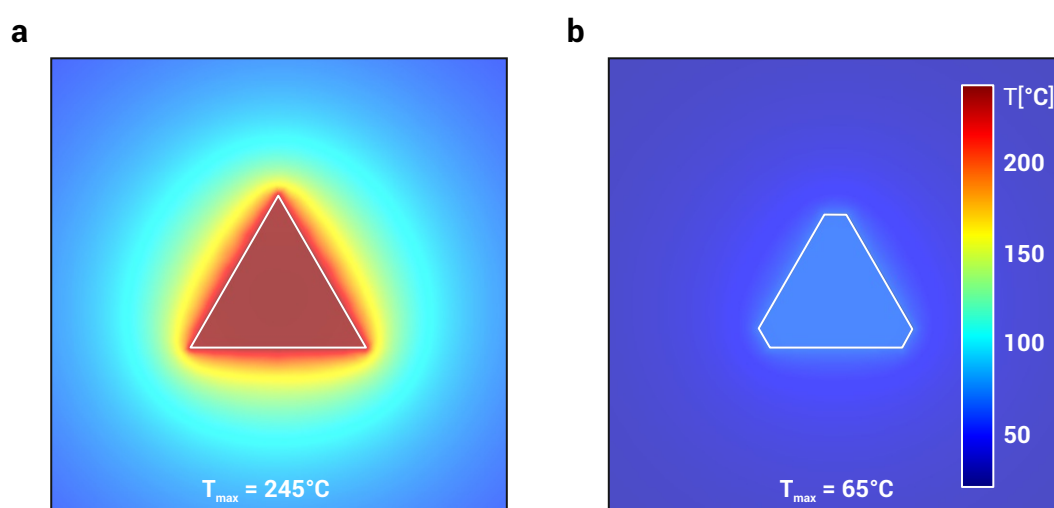


Figure 4.7 – Optically induced temperature increase during the printing process. Temperature distribution for a sharp (a) and a truncated triangle (b) when exposed to the laser power used for sorting the nanoparticles. The side length of both particles was chosen as 80 nm and the thicknesses were 7 nm for sharp and 9 nm for truncated triangles. The truncation was 10 nm. The sharp and the truncated triangles showed maximum temperatures of 245 °C and 65 °C, respectively, which are both well below the onset temperature, at which morphological changes are reported to occur.^{78,79}

one can conclude that the particle shapes remained unchanged by this approach due to the short exposure to the laser irradiation.

Optical properties of the printed particles

The optical analysis was performed *via* single particle scattering spectroscopy on the individually printed particles using the DFM (cf. Section 3.1.1). The results are shown in Figure 4.8. All of the spherical particles printed at t_1 and t_2 showed a peak at around 530 nm with a broadness of around 400 meV, which is comparable to the respective peak in the UV-Vis spectrum and very close to the printing wavelength of 532 nm. Both values are very typical for solid gold nanospheres.¹⁰⁷

On the other hand, the peak wavelengths of the truncated triangles were all lying between 750 nm and 800 nm, close to the printing wavelength of 808 nm. Their average linewidth was (187 ± 23) meV, which is much narrower compared to the case of spherical nanoparticles. This is in good agreement with the results reported by Raschke *et al.*,¹⁴³ who showed that the broad peak in the UV-Vis spectrum was due to inhomogeneous broadening. However, these properties were wrongly attributed to core-shell particles in this publication.

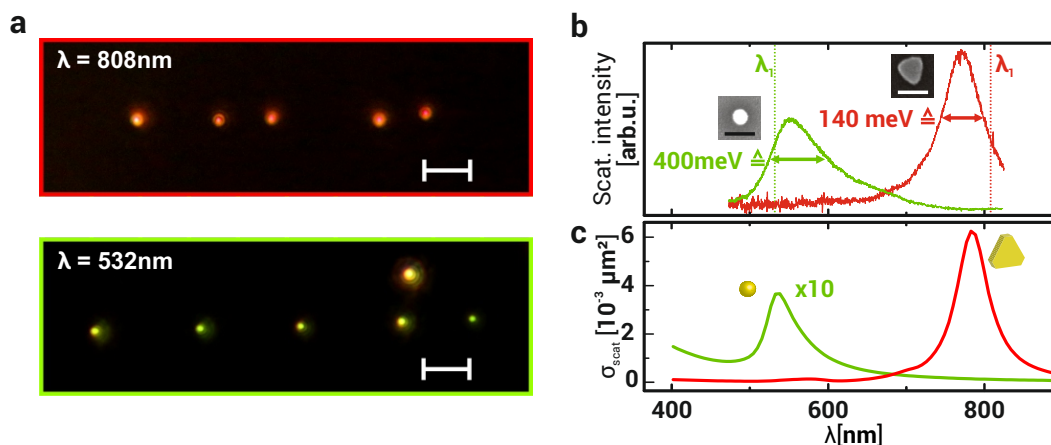


Figure 4.8 – Optical properties of particles printed from the synthesis at t_2 . (a) DFM pictures of particles printed from the synthesis at t_2 . At 808 nm only red nanoparticles and at 532 nm only green nanoparticles were printed. Since only particles were deposited where the plasmon resonance matched the printing wavelength, this showcases the selectivity of the nanoparticle sorting approach. The scale bars are 20 μm . (b) Single particle scattering spectra and SEM images of particles printed at 532 nm and 808 nm, respectively. The plasmon resonances matched the printing wavelengths very well. The linewidth of the triangular shaped particles was much narrower than for the solid gold spheres. The scale bars are 100 nm. (c) The calculated scattering cross sections of the particles found in the SEM were in good agreement with the measured spectra. The simulated structures were a sphere with a radius of 20 nm and a 9 nm thick triangle with a total side length of 80 nm, where the tips were truncated by 10 nm. To enhance visibility, the spectrum of the solid gold sphere was increased 10-fold.

Physically, the narrow linewidth can be explained with the reduced amount of interband damping that results from the redshift of the plasmon resonance, similar to what has been reported for gold nanorods.¹⁰⁷ Furthermore, Raschke *et al.*¹⁴³ pointed out the reduced amount of radiation damping due to the reduced volume of the nanoparticles compared to solid spherical nanoparticles. This is true for both core-shell as well as thin triangular nanoparticles.

Modelling the spectral properties of the synthesis

Using FDTD calculus (cf. Section 3.2.1) the spectra for gold particles with the physical dimensions obtained from SEM could be reproduced (Figure 4.8c). The thickness of the triangles was assumed to be the average thickness attained before in the AFM measurements (cf. Figure 4.2) for t_1 (7 nm) and t_2 (9 nm) for all calculations in the following. Most importantly, FDTD calculations allowed to compare the scattering of the individual particles quantitatively, which was crucial for investigating the temporal dynamics of the synthesis and excluding any other species of particles as contributions to the total spectrum.

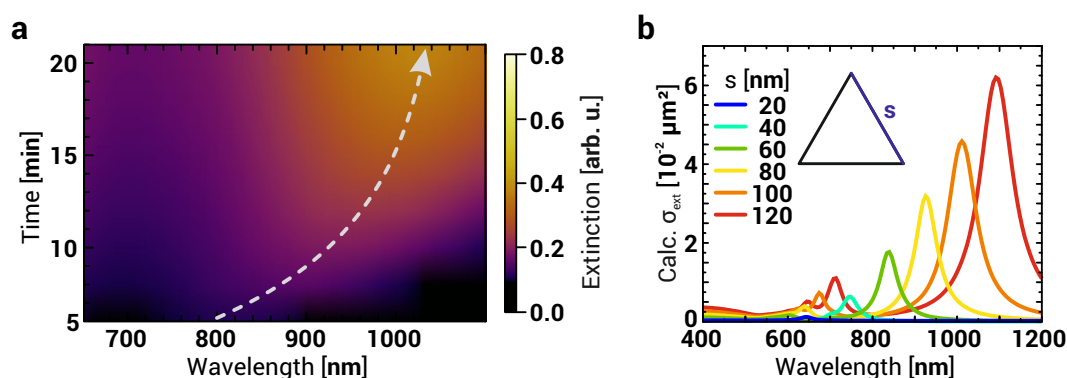


Figure 4.9 – Initial redshift of the synthesis. (a) Close-up of the NIR region during the first 20 min of the synthesis highlighting the initial redshift. The arrow is a guide to the eye. (b) Simulated spectra of triangles with increasing side lengths (s) showing a redshift as well as an increase in intensity with increasing side length s .

When looking closely at the NIR part of the spectrum within the first minutes, one could observe both a redshift and an increase in intensity of the spectral peak. A close-up of this part of the spectrum is shown in Figure 4.9a. In the beginning of the synthesis, a very weak peak at 820 nm that redshifted up to 1020 nm within 20 min was observed. At the same time, the peak underwent a 3.3-fold increase in intensity. Since the experimental data showed only sharp nanotriangles with the printing wavelength of 1064 nm at t_2 , this behavior could be attributed to the formation and growth of sharp triangles. To prove this assumption, FDTD calculations of sharp triangles of different side lengths (Figure 4.9b) were performed. The results show that increasing the side length of the triangles leads to both a redshift as well as an increase in intensity. A triangle with a side length of 20 nm has only a barely noticeable

peak at 640 nm. This explains why there was no measurable signal at the very beginning of the synthesis. The peak in the NIR first emerged after 5 min at 820 nm, which was where the plot starts. This corresponds to triangles with a side length of about 60 nm. The maximum redshift at 1020 nm corresponds to triangles with a side length of 100 nm. For all calculations, the thickness was assumed to be constant at 7 nm. Thickening of the triangles, which would lead to an increase in intensity, was neglected here. Hence, the increase in intensity in the simulations is about 2.6-fold, which is in good agreement with the measured increase of about 4-fold. The spectral shift as well as the broadening was also supported by TEM statistics obtained from samples arrested before and at the maximum red shift (Figure 4.10a). While the average side length shifted from 44 nm to 70 nm, the spread in side lengths also increased. This explains the increased width of the spectral peak at t_2 in the UV-Vis spectrum. Therefore, nanotriangles can fully explain the initial redshift of the synthesis.

TEM statistics also allow to weight the calculated spectra according to their relative appearance in the sample and thus calculate the expected spectrum for the particle distribution at t_1 (Figure 4.10b). At this time of the synthesis almost all triangles have sharp tips, hence different degrees of truncation were neglected here. As mentioned before, the relative appearance of spherical to triangular shaped particles was 3 : 1. Therefore, the extinction of the spheres, which were assumed to have homogeneous diameters of 40 nm, was weighted 3-fold compared to the total extinction from all of the triangles. Due to their small relative appearance and their very weak extinction cross section, triangles with side lengths smaller than 40 nm were

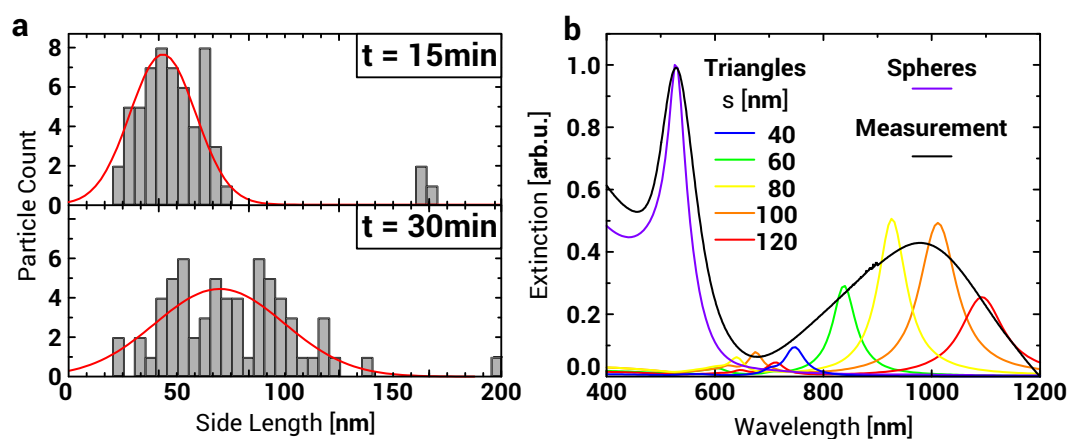


Figure 4.10 – Statistics of triangle size and simulated collective extinction spectrum. (a) TEM analysis of the triangle side length of a sample arrested before (top) and at (bottom) the maximum red shift exhibiting an increase in average side length as well as a broadening of the distribution over time. (b) Simulated collective extinction spectrum. The calculated extinction spectra of the different particle species were weighted according to their relative appearance in the TEM statistics. The ratio of spheres to triangles was 3 : 1. The distribution of triangular sizes was taken from $t = 30$ min. Other contributions than spheres or triangles were neglected. The black line depicts the actually measured extinction spectrum of the entire solution.

neglected. The individual cross sections were normalized to the 3-fold cross section of the spheres. The weighted cross sections were compared to the actual measured extinction spectrum of the entire particle dispersion (black line) obtained from UV-Vis spectroscopy. As one can see, the measurement coincided very well with the weighted simulated spectra. Also the intensity ratio between the green and the NIR peaks was in very good agreement. Hence, any other significant contributions to the NIR peak from core-shell structures or nanoparticle aggregates as suggested by other groups can be excluded. This proves Schwartzberg *et al.*¹³⁸ wrong, who claimed that the triangles are not contributing significantly to the spectrum.

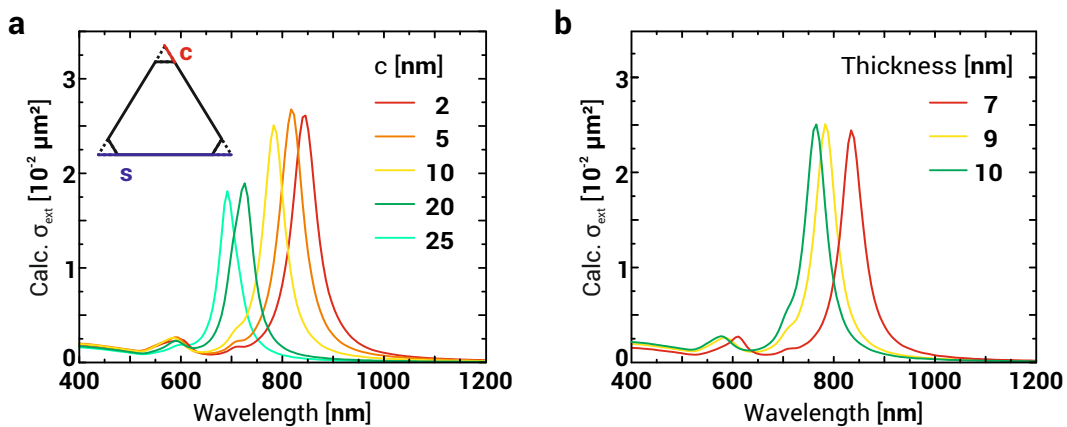


Figure 4.11 – Dependence of the plasmon resonance on the degree of truncation and the thickness of the triangles. (a) Blueshift of a nanotriangle due to increasing truncation of the tips. The thickness and side length s were set constant to 9 nm and 80 nm, respectively. The truncation c was varied from 2 nm to 25 nm leading to a blueshift of the plasmon resonance from 845 nm to 690 nm. (b) Blueshift of a truncated nanotriangle due to increasing thickness. Side length and truncation were set constant to 80 nm and 10 nm, respectively. The thickness was varied from 7 nm to 10 nm leading to a blueshift of the plasmon resonance from 834 nm to 765 nm.

Besides the initial redshift of the NIR peak, its subsequent blueshift is the most apparent feature of the spectral dynamics. Hence, the triangle model for the synthesis also has to sustain this observation. The triangles observed at t_2 were found to be thicker (cf. Figure 4.2d) and truncated at the tips compared to the triangles found at t_1 . No other significant changes could be observed in the TEM analysis. Therefore, it is reasonable to attribute the blueshift of the NIR peak to those morphological changes. In order to find proof for that, the spectra of triangles with different degrees of truncation and thicknesses were simulated. Figure 4.11a shows the simulation of truncated triangles with a thickness of 9 nm and a side length s of 80 nm, which were dimensions commonly found in the sample. Here, the term side length corresponds to the length of the entire side of the particle including the truncation, as it is depicted in the inset. The truncation length c was varied from 2 nm to 25 nm. As a result, the plasmon resonance shifted from 845 nm to 690 nm. Also, the extinction cross section decreased as the truncation increased. Both effects are in good agreement with the measured

data, as the NIR peak at t_2 was slightly less intense compared to t_1 . Furthermore, truncated triangles with a side length of 80 nm and a constant truncation of 10 nm were simulated. Here, the thickness was varied from 7 nm to 10 nm, which lead to a blueshift from 834 nm to 765 nm, while the intensity stayed almost constant albeit the increased volume of the particles. Hence, the observed truncation and thickening of the nanoparticles can explain the change of the spectral peak very well. Physically, the blueshift can be explained by a reduced concentration of charges in the corners during the plasmon oscillation. This on the other hand is caused by the truncation of the tips and thickening of the particles in total, as it is explained in Section 2.2.

Other properties reported for the nanoparticles produced with this synthesis were their polarization independence as well as their very good refractive index sensing behavior. Both were originally assigned to core shell particles.¹⁴³ Polarization dependent scattering spectra of a single truncated triangle showed no strong anisotropy (Figure 4.12a), a finding that was backed by polarization dependent simulations (Figure 4.12b). This is due to the main dipolar mode of the triangles being located in the three main corners, even for truncated triangles.¹⁵²

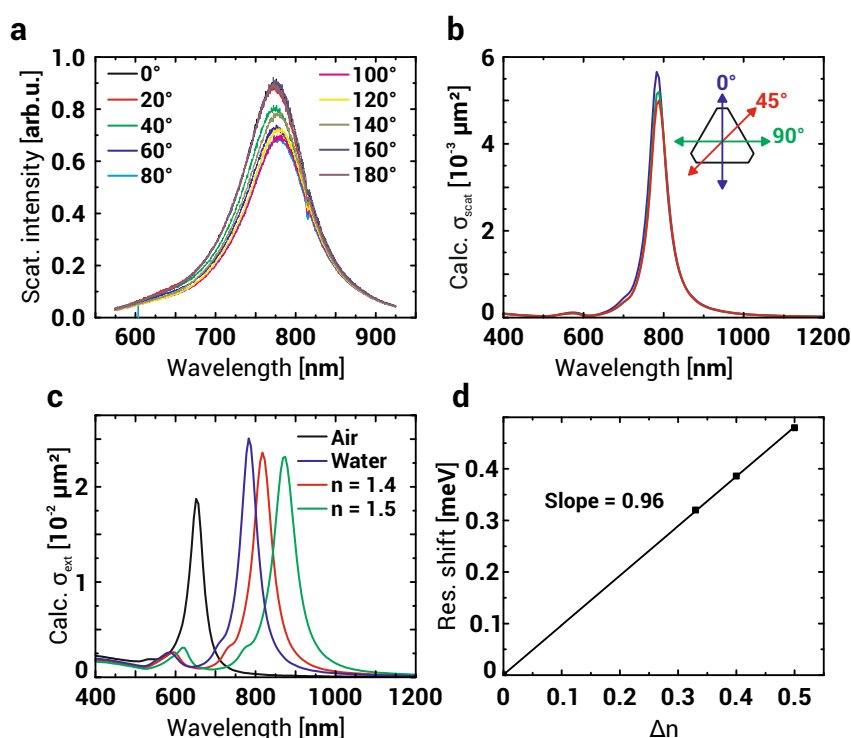


Figure 4.12 – Optical properties of truncated gold nanotriangles. (a) Polarization dependent spectra of a single truncated gold nanotriangle. (b) Polarization dependent simulations of a truncated triangle with a side length of 80 nm, a truncation of 10 nm and a thickness of 9 nm. (c) Simulations of the same particle as in (b) in different refractive index surroundings. A strong redshift of 96 meV per $\Delta n = 0.1$ was observed (d).

Hence, due to the symmetry of the triangle that feature a corner angle of 60° , the plasmon oscillation is the same every 60° . Therefore, the angular anisotropy is suppressed.

On the other hand, simulations of nanotriangles in different refractive indices show a strong influence on the plasmon peak. A triangle with a side length of 80 nm, a truncation of 10 nm and a thickness of 9 nm has its plasmon resonance at 652 nm in air (Figure 4.12c). The plasmon resonance of the same particle shifts to 784 nm when dispersed in water ($n = 1.33$) and to 818 nm and 872 nm in media of refractive indices 1.4 and 1.5, respectively. Hence, the specific redshift is 96 meV per $\Delta n = 0.1$ in the visible and NIR, which is even higher than the shift of 33 meV per $\Delta n = 0.1$ reported for the postulated nanoshells.¹⁴³ This difference can be explained by surface imperfections and the influence of the substrate, which were not taken into account here. Hence, nanotriangles feature both polarization isotropy and refractive index sensing behavior to the same extent as reported for the postulated nanoshells. Overall, the triangles explain all the optical properties that were reported in literature before, thus rendering the core-shell as well as the cluster hypotheses wrong.

Morphological mechanism of the triangle evolution

Although there were a lot of discussions on the optical properties and the morphological origin of the spectral peaks, no studies have investigated the mechanism of the morphological changes so far. In general, the morphology of synthesized nanoparticles is the result of two competitive phenomena: Fast growth far from thermal equilibrium that favors the formation of spikes and tips (kinetics) and slow surface diffusion processes, smoothing out those instabilities (thermodynamics).¹⁵³

These effects can be transferred to the observed transformation of the triangles, giving an intuitive model explaining the changes during the synthesis. In the first part of the synthesis, sharp triangular particles grow kinetically, leading to a redshift until $t = t_1$. Afterwards, two thermodynamically driven processes occur. On the one hand, previously nonreduced Au species and small nanoparticles present in the solution condense on the nanotriangle

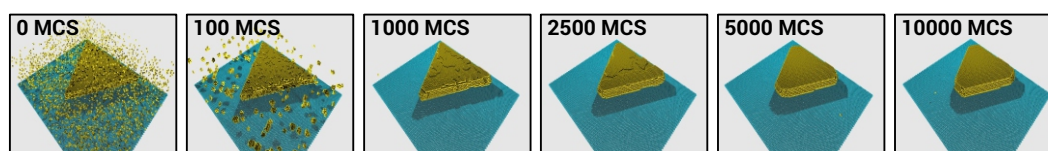


Figure 4.13 – Simulation of the evolution of a sharp, thin triangle to a truncated thicker triangle. The morphology of an initially sharp thin triangle is depicted after zero, 100, 1000, 2500, 5000 and 10000 Monte Carlo steps (MCS). The free gold atoms in the surrounding solution aggregated quickly forming bigger clusters that condensed on the triangles through an Ostwald ripening process within the first 1000 Monte Carlo steps, which lead to a thickening of the triangles. This was followed by surface diffusion of the atoms situated at the sharp tips to the bottom and top surface leading to a truncation of the triangles.

surfaces due to Ostwald ripening. On the other hand, intraparticle surface diffusion leads to migration of gold atoms from the tips to the top and bottom surfaces of the particle. These processes would lead to both a thickening and/or truncation of the triangles, which was the origin of the blueshift as proved previously (cf. Figure 4.11). A proof of this hypothesis was done through Monte Carlo simulations modelling the conformational changes a sharp gold nanotriangle experiences in the presence of excess gold (Figure 4.13).¹

In the initial state of the calculation, a sharp gold triangle was placed in a simulation volume with gold atoms occupying 1% of the available surrounding atomic sites. The simulation showed that the free gold atoms aggregated quickly forming larger clusters that condensed subsequently on the surfaces of the triangle. Since the top and bottom surfaces contribute most to the triangle surface, most gold clusters condensed there, leading to a thickening of the particle. This Ostwald ripening finished relatively quickly, leaving no free gold atoms left in the solution after 1000 Monte Carlo steps. Afterwards, the gold atoms situated at the tips slowly migrated to the top and bottom surfaces due to surface diffusion. This led to additional thickening as well as truncation of the triangles. Hence, the simulation confirms both initially made hypotheses.

Furthermore, this also supports the finding that after running the synthesis for a very long time, the NIR peak and the green peak merged into a single one (Figure 4.14a). Since also the

¹A simple kinetic model was applied, where atoms can diffuse between nearest neighbors in an fcc-lattice. The transition probability between two states c_1 and c_2 was defined according to transition state theory: $P(c_1 \rightarrow c_2) = \nu \cdot \exp[-E_{\text{act}}(c_1 \rightarrow c_2)/k_B T]$. The attempt frequency ν was set to 5×10^{12} Hz. For the activation energy $E_{\text{act}}(c_1 \rightarrow c_2)$, a linear model of the energy barrier with the first neighbor coordination number n_{fn} was chosen, hence: $E_{\text{act}} = E_b \cdot n_{\text{fn}}$.^{154,155} E_b was chosen to be 0.1 eV and the temperature was set to 300 K.

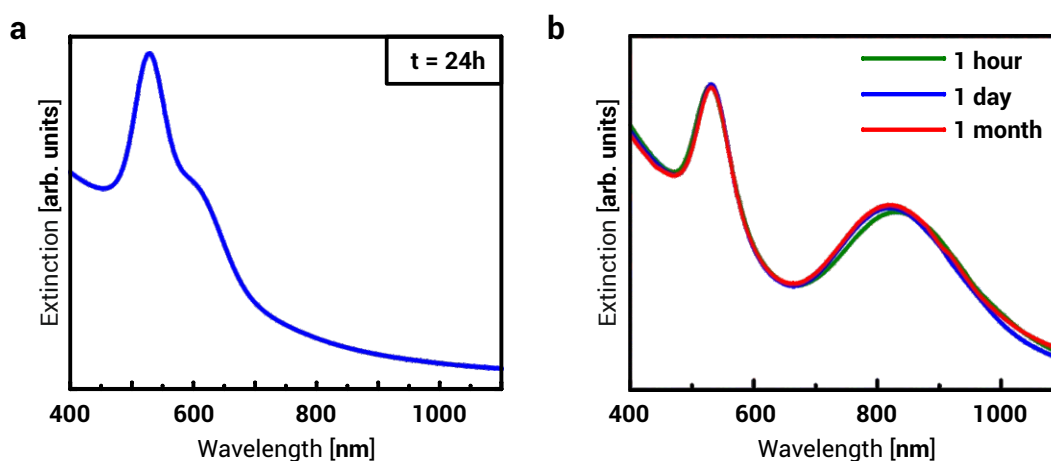


Figure 4.14 – Long term changes in the extinction spectrum of a non arrested solution and one arrested at t_2 . (a) UV-Vis spectrum after letting the synthesis run for 24 h. The two peaks almost merged into one, leaving only a slight shoulder on the red side of the peak. (b) UV-Vis spectra of a synthesis arrested at t_2 after one hour, one day and one month showing the good long term stability of the particles once arrested.

truncated triangles are thermodynamically unfavorable, surface diffusion let the triangles eventually converge to spherical particles. When the solution was arrested, the particles were stable for over a month Figure 4.14b. In a more recent study it has been shown that this is due to the formation of a thin layer of sulfur at the surface caused by the addition of Na_2S ,¹⁴⁷ inhibiting both further growth of the particles as well as surface diffusion.

Summary

A novel, all optical approach to sort and simultaneously pattern single plasmonic nanoparticles with regards to their plasmon resonance using optical forces was presented here. By applying lasers tuned to the spectral peaks of a polydisperse particle solution, up to three different species within one solution could be separated from each other. Due to the optical scattering force being directly proportional to the extinction cross section of a nanoparticle only particles with a resonance close to the applied laser wavelength were deposited on the substrate. This allowed to shed light on a previously controversial nanoparticle synthesis, namely the reduction of HAuCl_4 with Na_2S , which features an NIR peak in the extinction spectrum that first redshifts and subsequently blueshifts over time. Reports on the origin of this peak varied, assigning it to either nanoshells, nanotriangles or nanoparticle aggregates. By acquiring single particle spectra and SEM images of the very same particles, an unambiguous proof was found that this peak originates from triangular shaped particles. Using FDTD calculus and TEM statistics of the nanotriangle size distribution, the UV-Vis spectrum of the synthesis could be entirely reproduced, thus excluding any other significant contributions to the spectrum. Furthermore, all of the morphological and resulting spectral changes were successfully numerically modelled. In particular, it was found that sharp nanotriangles first grow kinetically in lateral direction up to a certain size yielding a redshift in the spectrum, until their thermodynamics become too unfavorable resulting in a thickening and truncation. Both of the latter effects result in a blueshift. This was confirmed by comparing measured data with electrodynamic and Monte Carlo simulations. Also other features, such as the very narrow homogeneous linewidth of the particles, their polarization independence, as well as their high sensibility to the refractive index environment could be attributed to the triangles.

In general this approach can potentially be applied to other polydisperse chemical nanoparticle syntheses or to investigate optical properties of a certain species of particles. Furthermore, this approach can also be of use for lithographic applications, since it allows the controlled patterning of different nanoparticle species within a single working process.

Chapter 5

Laser induced splitting of single gold nanorods into plasmonic dimers

As already discussed in the previous chapter, the printing of plasmonic nanoparticles involves significant heat generation. While in the former chapter it was found that heating was too low to change the particles' morphology, Babynina *et al.* have shown a deformation of gold nanorods (AuNRs) by printing them above a certain threshold.³² In particular, the nanorods could be bent and the bending angle could be controlled by the applied laser power. In their model the authors deemed hydrodynamic forces responsible for the bending. The nanorod becomes soft due to plasmonic heating and bends due to inhomogeneous viscous drag along its edges. Later research by Liaw *et al.*³³ showed that in addition to the hydrodynamic drag, the optical force acts stronger in the center than at the tips. This contributes roughly at the same magnitude to the bending moment exerted on the nanorod as the hydrodynamic forces. For both contributions, the anisotropy of the particle shape, a rod shape in this case, is crucial for the ability to reshape, since no reshaping would occur for a sphere.

Here, the topic of optothermal reshaping of gold nanorods is explored even further by showing the controlled splitting of a single plasmonic particle into two individual particles. A gold nanorod splits up into a dimer of two spherical particles while being deposited on a substrate in the same process. A combined electrodynamic and hydrodynamic model is proposed to explain the splitting mechanism that leads to the formation of dimers with subnanometer gap sizes. The results presented in this chapter are currently being prepared for publication as "*Splitting Gold Nanorods with Light*" by C.M. Maier, F. Schuknecht, V. Hintermayr and T. Lohmüller.

5.1 Context: Fabrication methods and applications of plasmonic dimers

Experimentally, creating a plasmonic dimer from two nanoparticles is challenging, but several approaches have been pursued to create such structures. On the one hand there are classical top down methods using focused ion beam¹⁵⁶ or electron beam lithography.^{157,158,159} On the other hand, bottom up approaches can be applied connecting individual nanoparticles with molecular linkers such as DNA origami¹⁶⁰ or proteins.¹⁶¹ Applying optical^{67,162} or mechanical forces¹⁶³ has also proven to be a promising approach. The latter has been exploited to bring the gap between two gold nanoparticles into the sub-nanometer regime,^{50,164} small enough for electron tunneling to occur as presented before in Section 2.3.¹⁶⁵ Another study has used the electron beam of a tunneling electron microscope to bring two previously deposited spherical particles closer together until tunneling started to take place and they eventually touched.^{166,167} Other approaches to enter this subnanometer regime use a plasmonic particle on a gold surface with a graphene layer¹⁶⁸ or single molecules¹⁶⁹ as a spacer.

As mentioned earlier in Section 2.3, the coupling of plasmonic nanoparticles leads to the formation of regions of extreme electric field enhancement. These can be used to enhance the signal in applications, like surface enhanced Raman scattering¹⁷⁰ or fluorescence enhancement.¹⁷¹ At these plasmonic hot-spots, hot electron induced chemistry could be demonstrated, since the strong electric fields lead to the extraction of high energetic electrons to a surface ligand.¹⁷² For these applications, classical electrodynamics would predict infinite enhancement or extraction factors, since the electric fields diverge for infinitesimally small gap distances. Quantum tunneling of electrons through the gap however provides a natural limit to the maximum achievable enhancement.¹⁵⁹

5.2 Optical splitting of gold nanorods into dimers and their optical properties

Cylindrically shaped gold nanorods are widely used in plasmonic nanoscience. They can be conveniently obtained through chemical synthesis in large quantities.¹⁷³ The nanorods used in this thesis have a diameter of 25 nm and a length of 137 nm (Nanopartz, USA, Figure 5.1 a). They feature a strong longitudinal plasmon mode at around 1064 nm (Figure 5.1 b). Albeit stable in solution for long periods of time, their anisotropic shape is naturally thermodynamically unstable. Hence, they can be seen to be frozen in a metastable state, only lacking the activation energy to undergo a morphological transformation. Link *et al.* have studied the shape transformation of gold nanorods in solution under pulsed laser irradiation. They found a

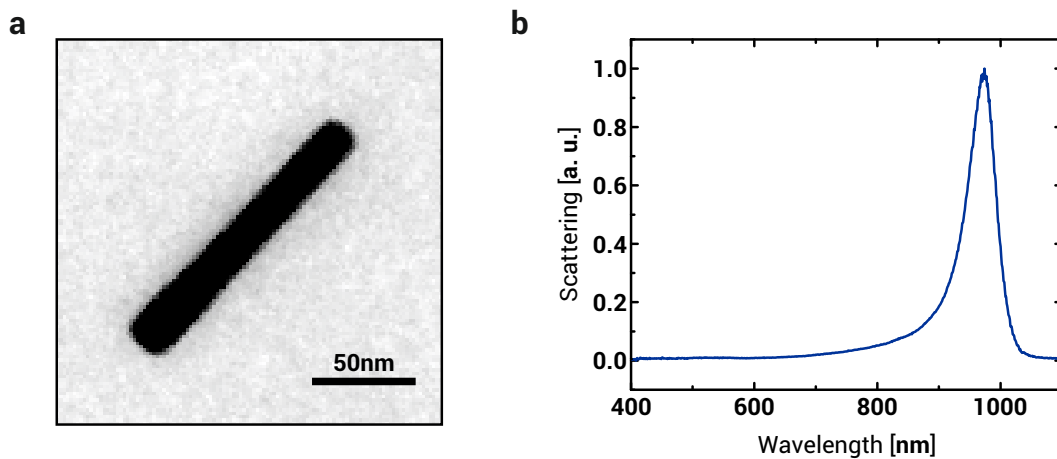


Figure 5.1 – Gold nanorods. Gold nanorods with a diameter of 25 nm and a length of 137 nm are used for the subsequent experiments. (a) TEM micrograph of the initial nanorod shape. They feature a strong longitudinal plasmon mode at around 1064 nm (b).

variety of particle shapes, such as spheres or pi-shaped particles.⁷³ In the work of Babynina *et al.*³² the reshaping was controlled by focusing the laser beam in a dark field microscope and manipulating the nanorods one by one. The energy dose a nanorod receives is thus tightly controlled. This led to the formation of the bent, V-shaped nanoantennas with controlled bending angle mentioned at the beginning of the chapter.

Here, the same experimental approach was used but with a much higher laser intensity. A droplet of the nanorod solution was put on a glass substrate and mounted on the microscope stage. A laser resonant to the longitudinal plasmon of the nanorod ($\lambda = 1064$ nm) was coupled into the microscope and focused on the substrate at a laser power of 100 mW (measured below the objective). Nanorods diffusing into the laser beam were then pushed onto the substrate (Figure 5.2a). When excited at their plasmon resonance, both a strong momentum transfer as well as strong plasmonic heating occur as it was already explained in the previous chapters. In

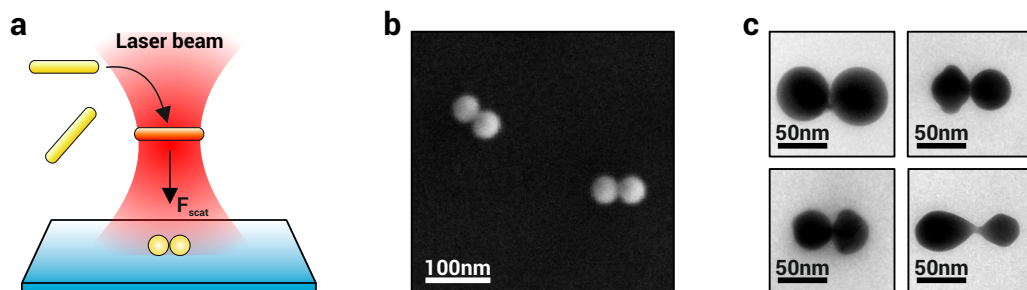


Figure 5.2 – Optical splitting of gold nanorods into spherical dimers. (a) Gold nanorods resonant to the incident laser wavelength ($\lambda = 1064$ nm) diffusing into the laser beam were optically printed onto a glass substrate at high laser powers ($P = 100$ mW). During the process, the rod was split, as it could be seen in SEM (b) and TEM images (c). Structures which were not completely split were also found, which suggests that the dimers were formed through reshaping of a single gold nanorod (lower right).

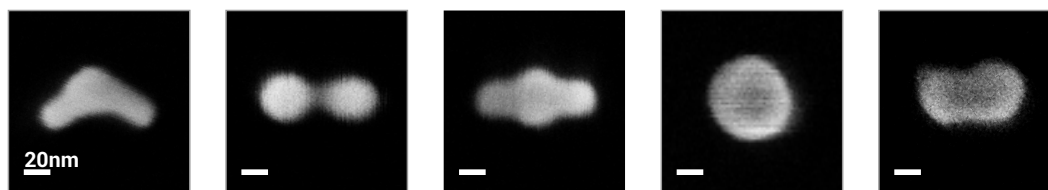


Figure 5.3 – Non dimer structures. Bent nanorods, non-separated dimers, pi-shaped particles and single spheres were also found in SEM analysis.

order to avoid unwanted heating after printing as well as to increase the interaction volume of the nanorod, the laser was focused about $1\ \mu\text{m}$ above the substrate. Subsequent SEM analysis showed dimers consisting of two equally sized spheres (Figure 5.2b). They were too close together to measure a gap distance using TEM imaging (Figure 5.2c). Amongst other side products, particles that were not entirely separated but featured two spherically shaped ends were also found, suggesting that the dimers were indeed formed through splitting of a nanorod (Figure 5.2c bottom right). Other side products such as bent nanorods, pi-shaped particles or single spheres were also observed (Figure 5.3).

By comparing the volume of the initial AuNR and the dimer, an important proof for the hypothesis that dimers were formed by splitting a single nanorod in half could be found. A statistical analysis of the dimers' sphere diameter revealed an average diameter of $40.8\ \text{nm}$ (Figure 5.4a). This yields a volume of $71.1 \times 10^3\ \text{nm}^3$ compared to the volume of the initial nanorod of $67.3 \times 10^3\ \text{nm}^3$. The difference of $\approx 5\%$ can be explained by the dimers being slightly deformed into oblate spheroids due to the high momentum and heating involved when hitting the substrate.

When entering the laser beam, the electromagnetic field induces a torque on the rod, thus aligning the nanorod longitudinally to the laser polarization.¹⁷⁴ Indeed, the orientation of the dimers was found to depend on the laser polarization (Figure 5.4b). However the standard deviation was relatively large ($\sigma = 45^\circ$), which can be explained by the high temperatures and therefore the strong stochastic Brownian forces involved.

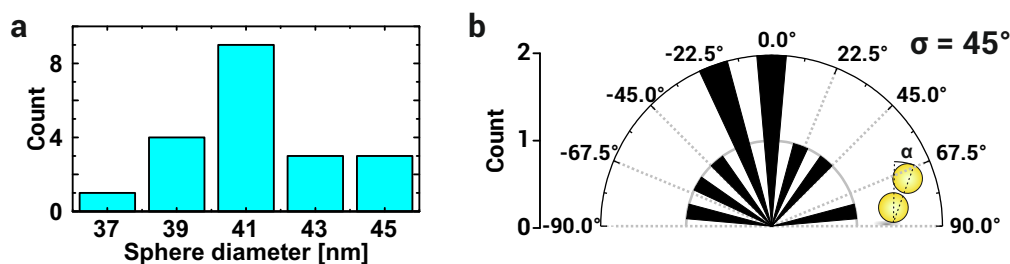


Figure 5.4 – Statistical analysis of the dimers. (a) Analysis of the dimer sphere diameter reveals an average sphere size of $40.8\ \text{nm}$. (b) Analysis of the orientation angle of the dimers with respect to the laser polarization. Indeed they aligned according to the laser polarization but the standard deviation was relatively large at $\sigma = 45^\circ$, which can be attributed to the strong Brownian forces.

Estimating the gap size

From the TEM images, it is not possible to tell whether the particles are actually separated and if so, by how much. Hence, the separation distance was estimated by recording the scattering spectra of individual dimers and comparing them to simulated spectra with different defined separation distances. The measured scattering spectra exhibited a strong peak at 637 nm to 672 nm and another shoulder/peak that could be approximated by fitting two Lorentzian peaks between 526 nm and 574 nm (Figure 5.5). The strongest peak at the highest wavelength could be identified as the longitudinal bonding plasmon of the lowest order (cf. Section 2.3). In accordance to theory, the strongest peak was the one with the strongest redshift (cf. Section 2.3). The other two peaks could be assigned to higher order modes, which only appear for very small gap distances.

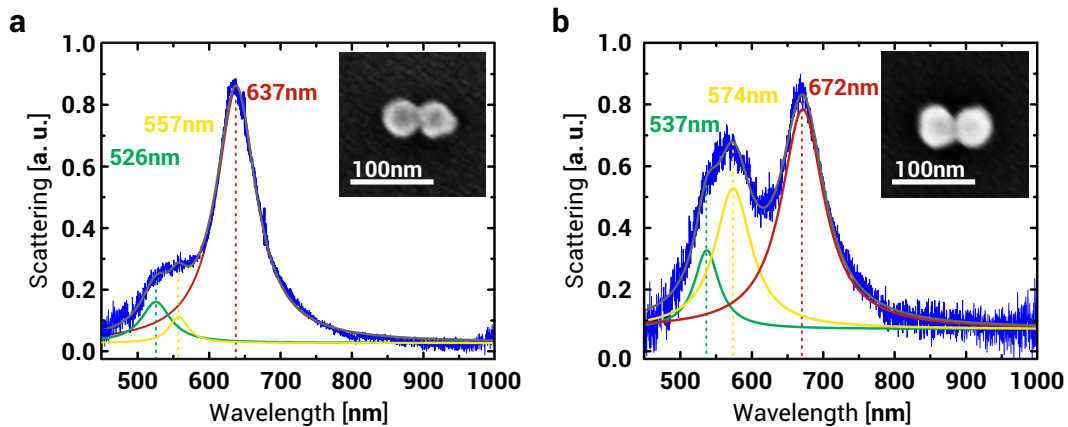


Figure 5.5 – Single particle scattering spectra of two individual dimers. The scattering spectra of the dimers exhibited several peaks between 526 nm and 672 nm and showed therefore a hybridization of the plasmon due to the occurrence of higher order modes. This behavior is characteristic for dimers with very small gap distances (cf. Section 2.3). The insets show SEM images of the dimers.

In comparison, the spectra of several dimers were calculated using FDTD (Figure 5.6). Two spherical gold nanoparticles ($d = 40$ nm) on a glass substrate were simulated with gap sizes ranging from 0.05 nm to 1 nm. Analogous to the experimentally recorded spectra, the surrounding medium was air. Nonlocal effects have been accounted for gaps smaller than 0.35 nm by the rescaling approach as described earlier in Section 2.3. The gap was rescaled by 1.06 \AA (2 atomic units), as suggested in literature.^{49,52} Due to the computational complexity no quantum tunneling was considered. In general, quantum tunneling leads to damping of the stronger peaks relative to the other peaks, since the amplitude of the electric field correlates with the peak height and therefore also the tunneling is the strongest here. Moreover, tunneling limits the redshift of the main plasmon mode, which diverges for decreasing gap sizes in classical electrodynamics. For gap sizes below 3 \AA it even leads to a blueshift as it reduces the maximum charge density within the particles (cf. Section 2.2).

A theoretical study involving a non-local quantum mechanical treatment has found the maximum wavelength for a dimer consisting of two 50 nm diameter spheres to be around 650 nm.⁵²

By comparing the measurements to the simulated spectra in Figure 5.6, a good agreement of the spectral peak distribution was found for gap sizes of 1 Å to 2 Å, which is already well in the quantum tunneling regime. Therefore, the exact determination of the gap size is difficult. However, one can conclude that the gap size was below 5 Å for two reasons. First, the spectral position of the strongest peak is above 600 nm. This corresponds to a gap size of about half a nanometer, where the corrected classical calculations are still trustworthy. A larger gap distance would lead to a peak below 600 nm.

More importantly however, the plasmon hybridization into three distinguishable modes, as observed in the measurements, appears only below gap sizes of less than half a nanometer.

Furthermore, the calculated spectrum for two connected particles with 1 Å overlap looks fundamentally different due to the appearance of a charge transfer plasmon mode around 820 nm (Figure 5.6 bottom). Hence, one can also deduce from the measured spectra that the particles are not connected but separated by a small gap. Structures formed *via* laser printing that exhibited a spectral peak in the NIR region of the spectrum were also observed as side products (Figure 5.7). This can be attributed to a not yet entirely separated dimer, as described previously.

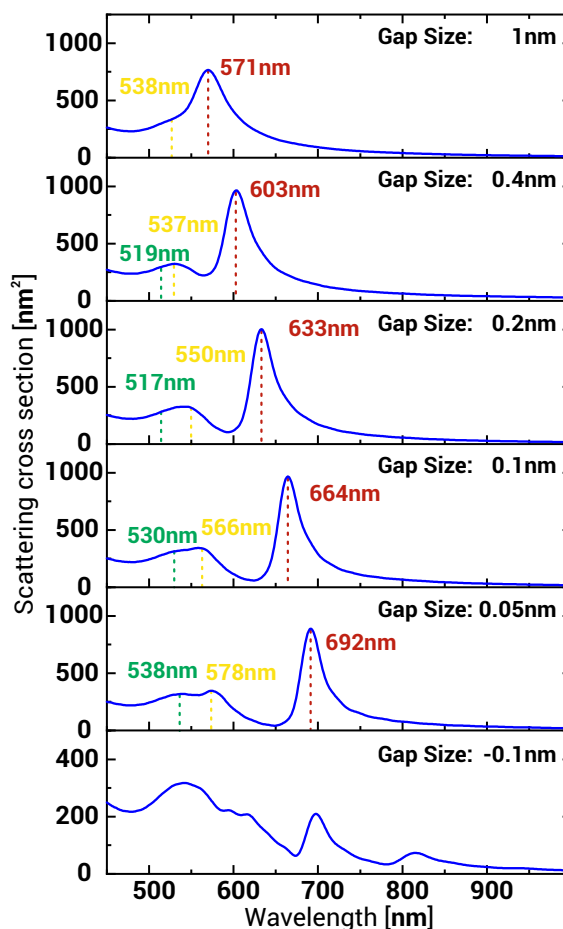


Figure 5.6 – Electrodynamic simulations of dimers with varying gap sizes. The simulations are used to correlate the occurring plasmon peaks seen in Figure 5.5 with the gap size.

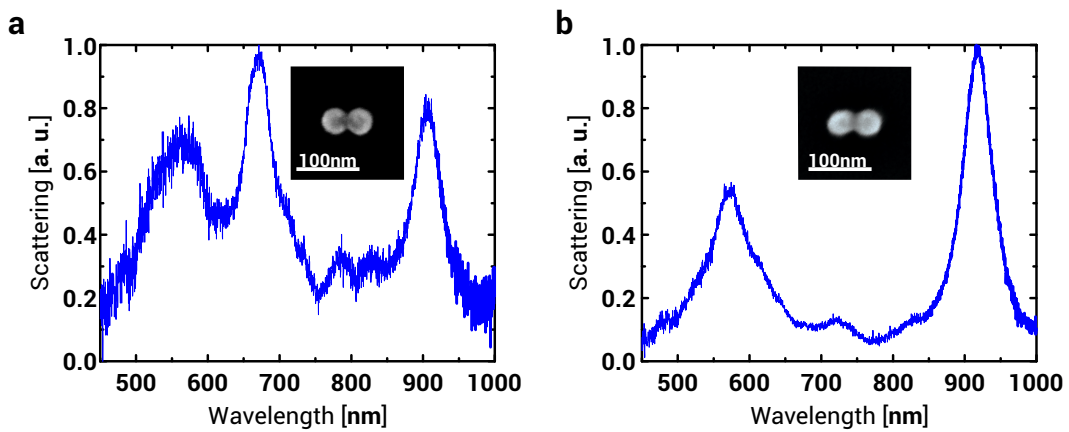


Figure 5.7 – Single particle scattering spectra of two interconnected dimers. The additional peak appearing in the NIR region was attributed as a charge transfer plasmon. The insets show SEM pictures of the respective particles.

5.3 Why do gold nanorods split?

Up to here, the question remains, *why* the gold nanorods split and form dimers in the process. As introduced in Section 2.5, splitting into chains of spherical particles has been reported for gold nanowires of large aspect ratios by heating them either optically or thermally.^{82,83} This behavior was attributed as an occurrence of Rayleigh-instability, a surface tension driven effect that leads to the breakup of a cylindrically shaped droplet into several spherical droplets.⁸⁴ Here, the aspect ratio of the particles is the critical parameter for the splitting to occur. Nichols found a minimum aspect ratio of 7.19 for a cylindrical droplet to break up into two spheres, independent of the material or other parameters.⁸⁶ Yet, the nanorods used in the present experiment only featured an aspect ratio of 5.5, hence additional effects have to be considered to explain the splitting. Assuming the heating was strong enough to melt the entire rod almost instantly (at least on hydrodynamic timescales), one can calculate the conformational dynamics of the nanorod by considering a cylindrical liquid droplet with the dimensions of the gold nanorod as a starting point. The relaxation of the droplet was modeled using COMSOL and indeed showed a convergence of the particle into a single sphere (Figure 5.8). In this simulation, any other external forces were neglected.

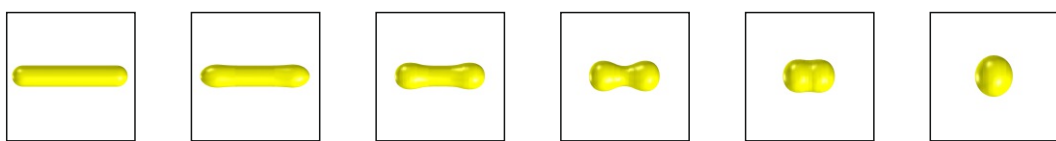


Figure 5.8 – Simulation of the relaxation of a droplet with the dimensions of the gold nanorod. The initially cylindrical droplet of aspect ratio 5.5 converged into a sphere undergoing a series of intermediate shapes resembling dumbbells.

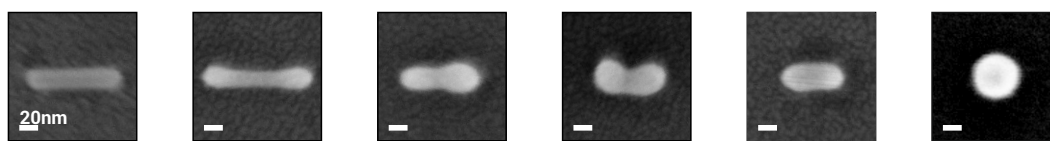


Figure 5.9 – Static heating of gold nanorods. Gold nanorods were deposited on a substrate and heated with a laser at the same laser power as in the splitting experiments. Fluidic forces were therefore excluded. The observed shapes resemble the intermediate steps calculated in Figure 5.8 very well.

In order to confirm this calculation experimentally, gold nanorods were placed on a glass substrate and heated with the same laser power density as used for the splitting experiments. In this configuration, any external flow or optical forces were excluded from the experiment by fixing the nanorods to the glass substrate. The shapes resembled the series of intermediate steps calculated previously (Figure 5.8) very well (Figure 5.9). Unlike the simulation, the conformational evolution did not necessarily proceed until the final shape, a sphere, but was frozen out in an intermediate step. This can be explained by considering that the nanorods are not always hit perfectly by the focused laser with regards to polarization and position. This is in contrast to the splitting experiments, where optical forces pulled the nanorod into the laser focus and aligned it according to its polarization, thus maximizing the interaction cross section. Therefore, in the static experiment, the intermediate shapes, albeit thermodynamically unstable, were frozen out due to the resonance shifting away from the incident laser wavelength. No dimers were found for this experimental configuration. External forces are thus crucial for the dimer formation process as the melting process alone did not provide the foundation for nanorod splitting.

Fluidic contributions

Babynina *et al.* proposed that hydrodynamic forces are the driving force for gold nanorod reshaping.³² Therefore, this contribution for the nanorod splitting was investigated as well. In this situation, hydrodynamic forces emerge as a counterforce to the optical forces due to the drag a particle experiences when propagating through a medium (water). Since nanorods are strongly non-isotropic, the drag does not act homogeneously on their surface. The pressure difference leads to the occurrence of a bending moment.^{32,33} The hydrodynamic contribution was calculated by solving the *Navier-Stokes* equation in three dimensions for the given geometry (cf. Section 2.1.3). Due to the lack of an analytic solution for this problem, the system was solved numerically using COMSOL Multiphysics (cf. Section 3.2.3). In its initial state, the rod experienced an enhanced hydrodynamic pressure at its tips (Figure 5.10a).³² For this simulation, the velocity was set to 0.18 m s^{-1} . This value was chosen such that the integrated total drag force was 73 pN, the magnitude of the optical force calculated for the nanorod (cf. Section 5.3) at the applied laser power (100 mW). This condition therefore assumes force equilibrium.

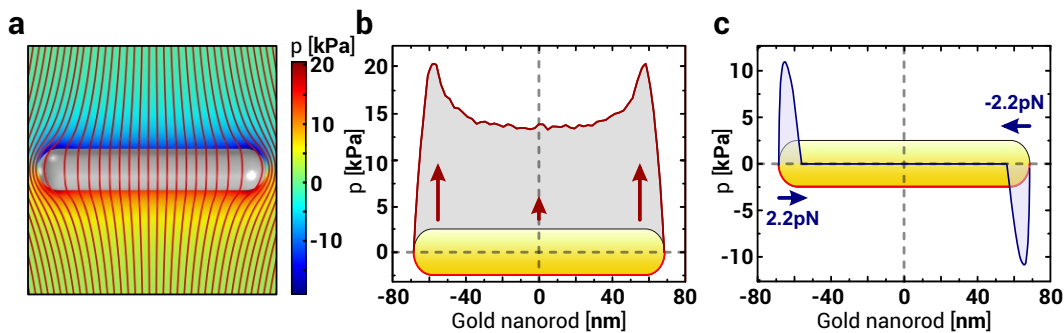


Figure 5.10 – Flow around a gold nanorod. (a) Flow map around a gold nanorod of dimensions 137×25 nm travelling at 0.18 m s^{-1} . (b) Pressure acting on the surface of the nanorod along its direction of propagation (downwards) reveals the pressure maximum at the nanorod tips that leads to a bending moment. (c) Pressure acting on the surface of the nanorod along its longitudinal axis. Here, a contribution pushing the tips of the nanorod to the center was observed. In both cases, the pressure was evaluated along the red line at the nanorod surface.

The temperature of the nanorod in the simulations was set to the bulk melting point of gold (1337 K) to account for the heating of the particle. Due to the simulation being a 3D vector calculation, the pressure contributions acting in the three different directions in space could be obtained.

In the following, the direction along the propagation of the nanorod will be referred to as z -direction and along the longitudinal axis as y -direction. Since a nanorod is rotational symmetric along its transversal axis (*i.e.* x -direction), no deformation moments were induced along this axis. Therefore, this spatial direction will be omitted in the following. The pressure in z -direction along the surface of the nanorod showed an enhanced pressure at the nanorod tips responsible for bending of the nanorods (Figure 5.10b). An evaluation of the pressure in y -direction revealed a contribution pushing the ends of the nanorods together (Figure 5.10c). This results from the curvature of the nanorod at its tips that allows a momentum transfer in y -direction. For the rest of the nanorod, the surface vector and thus also the pressure in y -direction were zero. This opposes the observation of the gold nanorod splitting up. Hence, from a fluidic standpoint, the hydrodynamics acting around a gold nanorod propagating in water cannot explain the splitting of the nanorod when printed at high laser intensities.

However, from the previous static melting experiment (Figure 5.9) and the corresponding simulations (Figure 5.8) it can be seen that the shape of the nanorod changed when irradiated at 100 mW. In particular, the gold nanorod transformed into a dumbbell-shaped particle before converging to a sphere. Therefore, in the following the hydrodynamics around a dumbbell-shaped particle of the same volume propagating at the same velocity as the nanorod (0.18 m s^{-1}) is considered (Figure 5.11a).

The pressure distribution acting in z -direction showed a stronger pressure at the tips of the dumbbell, as it was the case for the straight nanorod (Figure 5.11b). The behavior was slightly

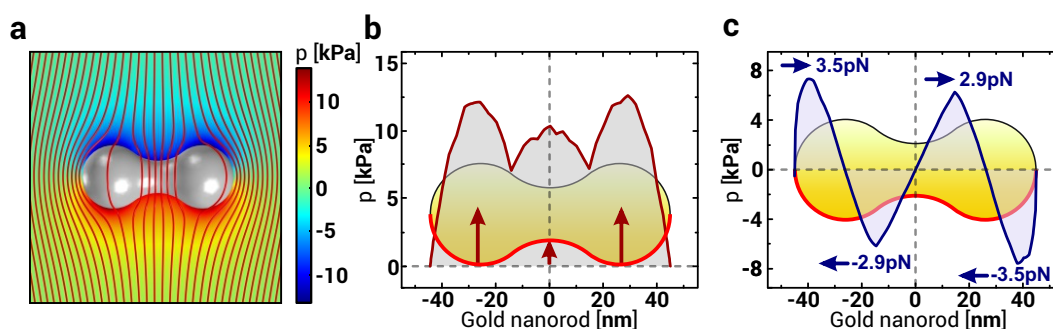


Figure 5.11 – Flow around a dumbbell-shaped particle. (a) Pressure profile around a particle shaped like a dumbbell as seen in Figure 5.8 and Figure 5.9. (b) Evaluating the pressure at the particle surface with regards to the z -normal direction revealed a stronger drag force at the tips than in the middle, as it was the case for the straight nanorod. (c) The pressure acting along the longitudinal axis of the particle looked more complex. A contribution at the tips of the particle pushed the two halves of the dumbbell together, whereas at the center of the particle, the pressure pushed the dumbbell apart. In both cases, the pressure was evaluated along the red line at the nanorod surface.

more complex, as the pressure also increased in the middle of the particle, but remained higher at the tips. Hence, a hydrodynamic bending moment is also present in this case. Along the y -direction, the behavior is even more complex. While a net force pushed the tips to the center of the particle, the pressure acting at the center of the particle pushed the two parts apart at the same time (Figure 5.11b). By integrating the pressure in y -direction along the dumbbell, the forces were obtained for the different surface domains. In particular, forces of 3.5 pN push the ends of the tips to the center and forces of 2.9 pN push the center of the particle apart.

Hence, the increased pressure in the middle section and at the tips of the particle in combination with the hydrodynamic bending moment was responsible for the particle deformation. This could eventually have led to a shape as it is shown in Figure 5.12. Here, the pressure in the

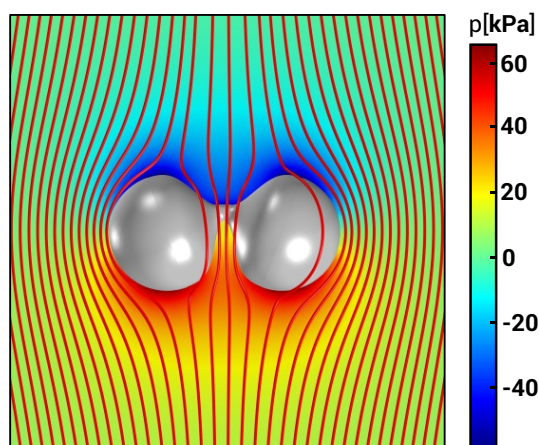


Figure 5.12 – Flow and pressure profile around a deformed dumbbell-shaped particle. The increased deformation leads to an increased hydrodynamic pressure acting on the surface of the particle, potentially favoring a splitting.

middle led to a thinner middle section, while the pressure at the tips compressed the entire particle in y -direction. The bending moment caused a tilt of the two spherical ends. For a shape like this, the pressure rose compared to the dumbbell. The integrated force acting on the center section of the particle increased to 14 pN, while the force acting on the tips rose to 13.3 pN. It is important to mention that this shape is purely hypothetical. However, an increased deformation of the particle leads to stronger forces acting on the particle, which would favor a splitting of the particle into a dimer.

Optical contributions

The optical force acting on a plasmonic nanoparticle under laser irradiation is a result of the coupling of the incident electromagnetic field to the internal field of a polarized particle. Hence, the force acting on a particle can be determined directly from the electric and magnetic fields inside the particle.

The formalism to relate the electromagnetic field to the mechanical force, the Maxwell stress tensor, was introduced in Section 3.2.2 as Equation 3.18 and Equation 3.19. Plasmonic nanoparticles are known for their high polarizability. This polarization leads to the inhomogeneity of the fields inside a particle. Hence, the optical force does not act isotropically over the nanorod. For the nanorods, spatially resolved E - and B -field maps were obtained through FDTD calculus (cf. Section 3.2.1). In particular, the direction of the force was of interest, which was obtained by separating the contributions of the fields in all three spatial directions. As an example, Figure 5.13 shows the distributions of the z - and y -contributions of $\Re[E]$. As for the hydrodynamic drag, the x -direction was omitted since it does not contribute to the optical load due to the particle's symmetry.

The E - and B -field maps were used as an input for the optical load calculations as published by Liaw *et al.*³³ The distributions for z - and y -direction are highly anisotropic. In z -direction, the field and the optical force were strongest in the middle of the rod (Figure 5.14a). This contributes significantly to the bending of the nanorod at lower laser powers.³³ Integrating over the entire nanorod yielded the total force in z -direction of 73 pN, which was used as a basis for the hydrodynamic calculations in the previous section. Evaluating the y -component

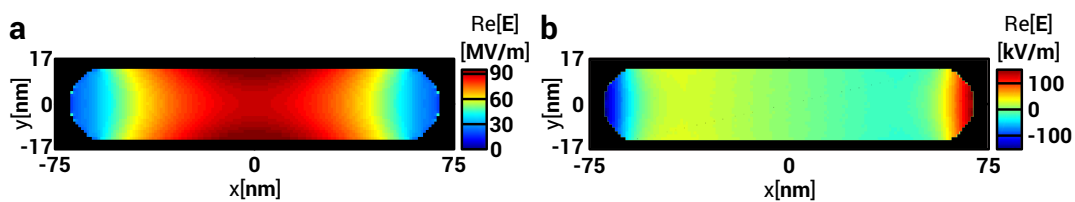


Figure 5.13 – Real part of the electric field inside a gold nanorod excited at 1064 nm with 100 mW at an NA of 1.0 in the xy -plane. (a) z -component of $\Re[E]$. (b) y -component of $\Re[E]$.

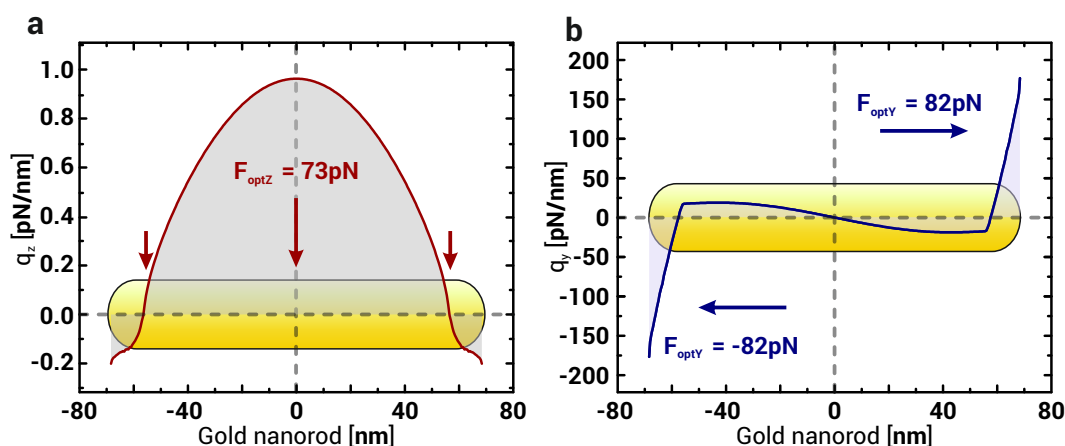


Figure 5.14 – Optical load on a gold nanorod. (a) Distribution of the optical load along a gold nanorod in z -direction. The optical force acts mainly in the middle of the nanorod, which favors a bending of the particle.³³ Integrating over the entire nanorod yields a total force of 73 pN. (b) Optical load in y -direction featuring a strong contribution which pulls on the tips of the nanorod (82 pN).

of the fields yielded a strong contribution at the tips of nanorod, whereas only weak fields appear in the center (Figure 5.13b). The direction of the fields led to a force of 82 pN pulling on both ends of the nanorod (Figure 5.14b), which cancel out through symmetry and thus do not contribute to the total force acting on the nanorod. However, this force aligns the nanorod with the laser polarization. Moreover this force pulls on the ends of the particles which favors a splitting of the nanorod.

The E -field distribution of dumbbell-shaped particles exhibited a more complex behavior. The magnitude of the z -component of $\Re[E]$ was much higher in the center than at the two ends of the dumbbell (Figure 5.15a). The major contribution of the scattering force acted in the center (Figure 5.16a). The total force was lower than for the straight nanorod (4.1 pN), due to the resonance of the nanoparticle shifting away from the incident laser wavelength of 1064 nm. However, a bending moment on the particle is still induced, which would favor a deformation as described previously.

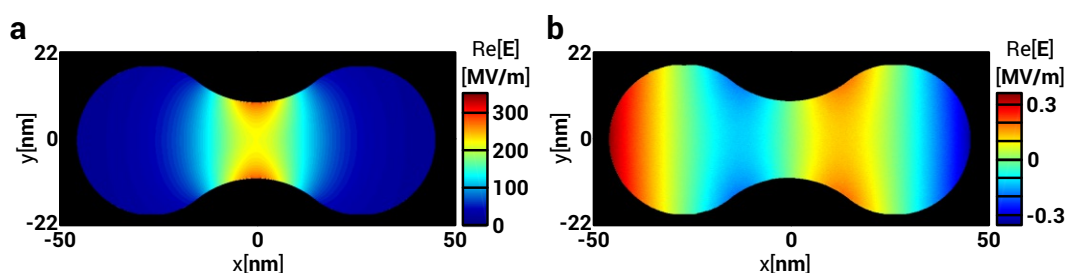


Figure 5.15 – Real part of the electric field inside a dumbbell-shaped gold particle excited at 1064 nm with 100 mW at an NA of 1.0 in the xy -plane. (a) z -component of $\Re[E]$. (b) y -component of $\Re[E]$.

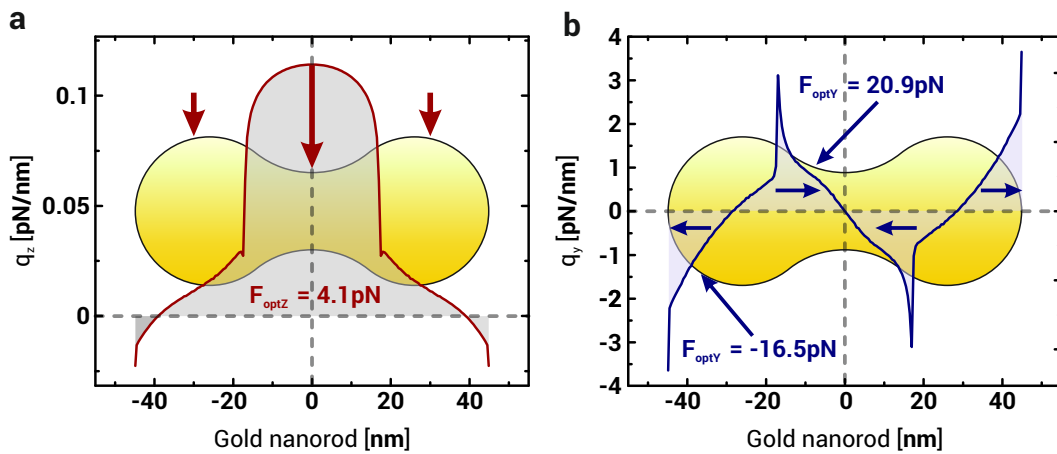


Figure 5.16 – Optical load on a dumbbell-shaped gold nanoparticle. (a) Distribution of the optical load in z -direction. The optical force acts mainly in the middle of the particle, favoring bending of the particle. Integrating over the entire nanorod yielded a total force of 1.3 pN. (b) Optical load in y -direction featuring a strong contribution which pulls on the tips of the nanorod (5.2 pN). However the center domains were both pulled to the middle of the particle.

The electric field in y -direction exhibits local maxima at the inner sides of the dumbbell spheres (Figure 5.15b). Furthermore, similar to the straight nanorod, the field was strong at the ends of the dumbbell. The other contributions of the Maxwell stress tensor could be divided into those domains. This leads to a complex behavior of the optical load on the particle (Figure 5.16b). A total force of 16.5 pN pulls on each end of the particle. However, in the center section, a net force of 20.9 pN pulls on each side towards the center of the particle.

Neither surface tension driven deformation nor hydrodynamic drag and optical load could explain the splitting behavior completely on their own. Dimer formation is thus a complex interaction of these effects. Surface tension led to a deformation of the particle upon laser irradiation. This increased the surfaces of attack for the fluidic flow around the particle. In particular, surfaces were formed that induced hydrodynamic strain forces. A further deformation of the nanoparticle would lead to an increase of these strain forces. However, with a magnitude of a few piconewton, these forces are too weak to cause the splitting alone. The optical contribution was much stronger for the case of the straight rod. In particular in z -direction, the total force acting on the nanorod was 73 pN, which has been shown to be enough to reshape a gold nanorod.³² In y -direction, the force pulling on the ends of the nanorod was 82 pN. However once transformed into a dumbbell, a strong contribution acting towards the center of the particle appeared. At the same time, there was still a contribution pulling on the ends of the particle and a bending moment. The different contributions capture the main points of the complex splitting process, which due to the interplay of the different contributions is not trivial.

Summary

This chapter introduces a completely new, all-optical laser driven approach of forming plasmonic nanodimers with subnanometer gaps by splitting a gold nanorod into two equally sized spherical particles. Single particle spectra were compared to electrodynamical simulations to estimate the interparticle distance. According to the spectra, the gap size is in the subnanometer range, a regime difficult to obtain with other methods. A model was devised to explain these observations considering an interplay of surface tension driven deformation, hydrodynamic drag forces and inhomogeneous optical forces acting on the nanorod.

The approach presented here facilitates the fabrication of dimers with subnanometer gap distances in a simple one-step procedure. This is useful for applications that rely on strong field enhancement like single molecule Raman spectroscopy or hot electron injection driven chemical reactions.

Chapter 6

DNA delivery into cells using optical and thermophoretic forces on Janus nanopens

Up to now, only repulsive forces acting on nanoparticles were discussed, leading to particle deposition on a substrate. These repulsive forces dominate when plasmonic particles are hit at or close to their plasmon resonance. However, when exposed to irradiation sufficiently far away from the plasmon resonance, both scattering and absorption are small compared to the gradient force. This allows to use tightly focused laser beams as optical tweezers. Another dimension emerges in case of anisotropy of the particle composition, thus creating a Janus particle. When compiled from a metallic and a dielectric part, another force, namely thermophoresis, emerges. Here, the light absorption from the metallic side leads to a temperature gradient over the particle. As described previously for micron sized particles,⁹ a thermophoretic force acting inversely to the temperature gradient leads to a vertical displacement of a particle in an optical trap.

Here, a new nanoparticle species, Janus nanoparticles or nanopens, is introduced consisting of a plasmonic gold tip and a dielectric alumina shaft. For the first time, controlled self-thermophoresis of a nanoparticle in an optical trap is shown here. This principle is applied to position nanopens on the surface of a living cell. By functionalizing the nanopens with DNA they could be used as a biomolecular shuttle. When injecting them with a laser resonant to their plasmon it was shown that the DNA survives the injection process due to an anisotropic temperature distribution. This paves the way for numerous biomolecular delivery applications. The results presented in this chapter have been published in *Nano Letters* in 2018 as "*Optical and Thermophoretic Control of Janus Nanopen Injection into Living Cells*" by C.M. Maier, M.A. Huergo, S. Milosevic, C. Pernpeintner, M. Li, D.P. Singh, D. Walker, P. Fischer, J. Feldmann and T. Lohmüller.¹⁷⁵

6.1 Context: Gold nanoparticles for biotechnological applications

Over the years, gold nanoparticles have found applications in many biology-related fields due to their high biocompatibility.¹⁷⁶ For instance, gold nanoshells are currently being investigated as a future tool for photo-thermal cancer treatment.¹⁷⁷ In a different application, the rapid temperature increase that is inherent to all plasmonic nanoparticles makes it possible to melt DNA that is attached to the particle surface within microseconds, forming the basis for laser induced polymerase chain reaction, which is much faster than conventional approaches.¹⁷⁸

This makes gold nanoparticles in combination with their bright appearance in dark-field microscopy very good probes for *in-situ* investigation of biological samples. Their strong spectral sensitivity to their dielectric environment allows biosensing by observing spectral shifts¹⁷⁹ as described previously in this thesis (Chapter 4). On the other hand, they can be functionalized with a multitude of different molecules on their surface, facilitating their usage as molecular delivery shuttles.¹⁸⁰ For this purpose, gold nanoparticles have to be brought into the biological system of interest, such as a cell.

Cells are surrounded by their cell membrane, a thin 5 nm to 10 nm thick layer that protects them from their environment. It consists mostly of a lipid-protein assembly held together by noncovalent bonds (Figure 6.1). One of its main functions is to contain the cell and prohibit the intrusion of foreign objects or molecules. Therefore, bringing a particle into a cell is no trivial task.

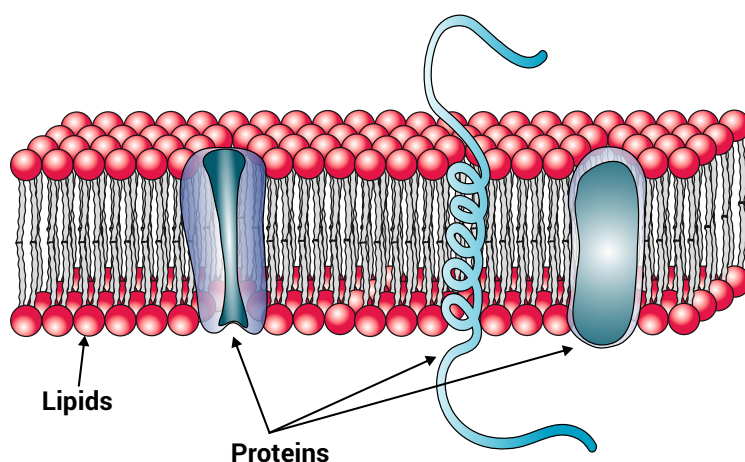


Figure 6.1 – Cell membrane. The cell membrane consists of a mixture of lipids and proteins forming a thin layer that protects the cell from the environment.

Whereas objects like sodium or calcium ions or water molecules can and shall migrate through the membrane through special channels, it imposes a strong barrier for larger objects like nanoparticles. In order to deliver gold nanoparticles into living cells, approaches were

developed that relied on endocytosis of the particles into the cells.¹⁷⁶ However, neither the number nor the position of the delivered particles could be controlled.

It was shown by Urban *et al.* that the local heating and optical force from gold nanoparticles could be used to induce local phase transitions in the phospholipid membrane of unilamellar vesicles.¹⁸¹ Further studies showed that even a controlled injection of single particles into vesicles was possible.⁶⁹ This paved the way for using plasmonic particles as a handle for cell membrane manipulation. More recent studies have shown the potential of plasmonic particles for targeted optical manipulation of the membrane properties creating pores¹⁸² or increasing the permeability for ions or molecules.⁷¹

Li *et al.* were first to report a single step injection of gold nanoparticles into a living cell using a continuous wave (CW)-laser.⁸ A gold nanoparticle was printed on the cell membrane and then injected into the cell by increasing the laser intensity until a hot steam nanobubble formed around the particle, rupturing the membrane and facilitating the intrusion of the gold nanoparticle at the same spot *via* optical forces (Figure 6.2). Perforating the cell membrane with pulsed laser beams has been used before as a method to transfer gold nanoparticles or DNA into living cells.^{183,184,185} However, the high peak intensities involved there pose a threat to cell viability. By using a CW-laser that has much lower peak intensities, Li *et al.* were able to achieve a cell survival rate of over 70%, thus proving the applicability of their approach for potential future targeted delivery applications.

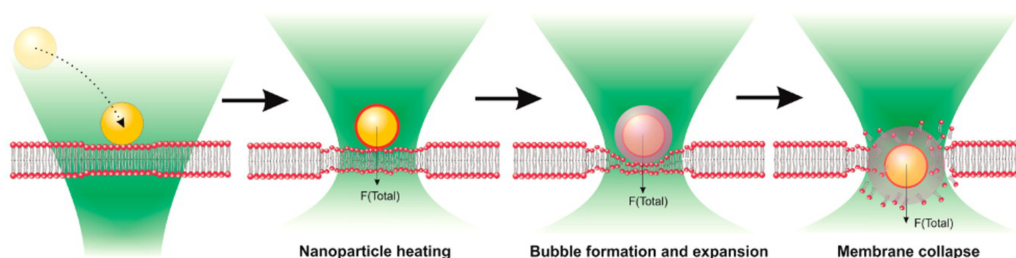


Figure 6.2 – Injection of a gold nanoparticle into a living cell. The gold nanoparticle is placed on the cell membrane *via* optical printing (left). Subsequently the particle is heated up until a nanobubble is formed (middle), which eventually leads to the membrane collapse and nanoparticle injection. Figure adopted from Li *et al.*⁸

The temperature required to form a nanobubble around a nanoparticle is the spinoidal decomposition temperature of water, which is reported to be around 320 °C.¹⁸⁶ This is a problem for biomolecules such as DNA or proteins attached to the surface of nanoparticles, since those usually already decompose or denature at much lower temperatures.^{187,188} In the following, this issue is tackled by using Janus nanoparticles that exhibit an internal temperature gradient when excited with a laser.

6.2 Optical properties of Janus nanopens

The nanoparticles introduced in this chapter, Janus nanopens (JNPs), featuring a plasmonic spherical tip connected to a dielectric shaft are a new species of nanostructures. The particles were prepared by a collaboration from the group of Prof. Peer Fischer at the Max-Planck-Institute for Intelligent Systems in Stuttgart using glancing angle deposition as described previously.¹⁸⁹ Briefly, gold nanoparticles were first deposited in a hexagonal array using block copolymer micellar nanolithography^{190,191} on a silicon wafer. Subsequent shadow-growth physical-vapor deposition was used to increase the size of the gold nanoparticle to the desired diameter (here 80 nm). To increase the adhesion of the alumina shaft, a layer of about 5 nm titanium was then deposited onto the gold particles. Afterwards the Al_2O_3 was deposited on top growing shafts of a length of about 500 nm. The columnar shape was achieved by simultaneously rotating the sample under a distinct angle. When rotation speed, tilting angle and growth rate were aligned correctly to each other, axisymmetric deposition and therefore column formation was achieved. A single three inch wafer contained about 10^{11} nanoparticles, thus providing enough particles to allow working in colloidal solutions.

The particles were put into solutions by ultrasonication of the wafer in ultrapure water that led to a release of the individual JNPs (Figure 6.3a). Using the material sensitive ESB detector in the SEM (cf. Section 3.1.4) for imaging of the particles, the heterogeneity of the particle could be highlighted (Figure 6.3b).

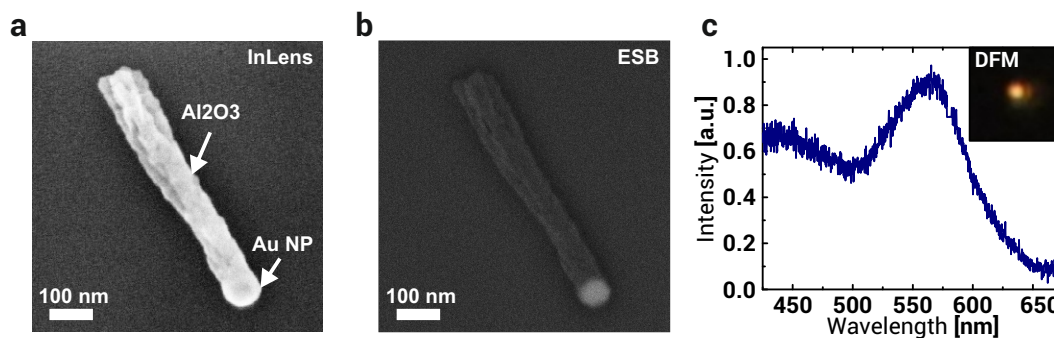


Figure 6.3 – Properties of Janus nanoparticles. SEM image of a JNP using the InLens (a) and ESB detectors (b). Single particle spectrum of the same JNP showing its resonance position at ~ 560 nm (c). Hence, the JNPs appeared similar to conventional spherical nanoparticles in the DFM (inset).

The scattering spectrum of nanopens is very similar to the one of a single gold nanoparticle of the same diameter. This can be explained as the gold tip couples much stronger to an incident light wave than the alumina shaft and therefore dominates the optical response. Janus nanoparticles have their scattering maximum at ~ 560 nm in air on a glass substrate, which was determined using dark field spectroscopy. The resonance peak is slightly redshifted compared to the one of a spherical gold nanoparticle of the same diameter due to the increased

refractive index of the alumina shaft (~ 1.67)¹⁹² compared to water (~ 1.33) (Figure 6.3c). The dominance of the plasmonic scattering makes the particle appear like a spherical gold nanoparticle in the DFM (Figure 6.3c inset). This observation was quantified by calculating the scattering cross section of a JNP (Figure 6.4a) and comparing it with the cross section of the shaft without the gold tip (Figure 6.4b). Indeed, the magnitude of the shaft's scattering cross section in the visible regime was more than two magnitudes lower than the scattering cross section of the entire nanopen. Only for shorter wavelengths, the spectrum rose but stayed significantly lower than the scattering of the entire JNP. Furthermore, Figure 6.4a shows a small polarization dependence of the nanopen scattering. Whereas the peak wavelength stayed almost the same, the magnitude of the scattered light was higher for a polarization along the nanopen due to the refractive index anisotropy on one side of the nanopen. This was confirmed by polarization dependent single particle scattering spectra. The amplitude of the plasmon peak fluctuated in a sinusoidal manner, which meets the expectations for a rod shaped geometry (Figure 6.4c).

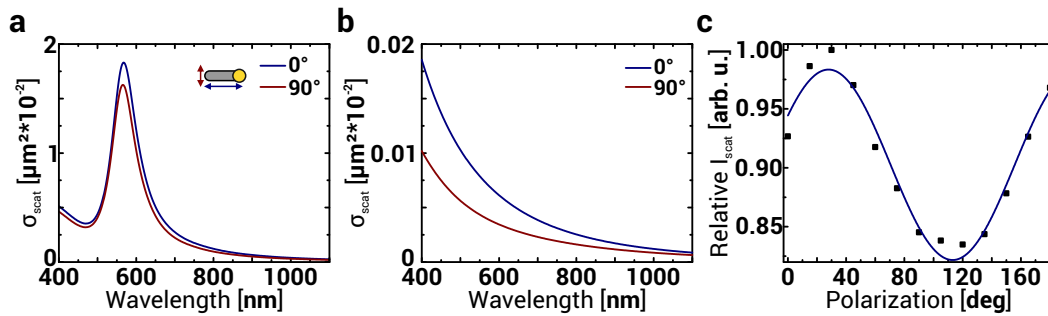


Figure 6.4 – Polarization dependent scattering of JNPs. FDTD calculations of the JNP (a) and the alumina shaft (b). The wavelength of the nanopen plasmon resonance was not polarization dependent, whereas the intensity was slightly lower for an excitation perpendicular to the nanopen axis. The scattering of the alumina shaft was more than one order of magnitude smaller than the total nanopen scattering and therefore negligible. (c) Measured polarization dependence of the JNP scattering intensity showing a sinusoidal behavior.

Optical forces acting on JNPs

Both the gold nanoparticle tip and the alumina shaft contribute to the total force once the particle is exposed to a focused laser beam. As discussed in Section 2.1.2, the way plasmonic nanoparticles interact with light depends strongly on the wavelength. Close to the resonance, repulsive forces dominate, whereas redshifted from the resonance, the forces become attractive. The dielectric alumina shaft on the other hand is subject to an attractive force field throughout the visible and NIR spectrum, due to the negligible absorption. Using the T-Matrix approach (cf. Section 3.2.2), the optical forces acting on both the shaft and the gold nanoparticle tip were calculated. Due to the dielectric character of alumina, no electron transfer and hence

no spreading of the plasmon into the shaft was assumed. Hence, the total force acting on the JNPs is the sum of the contributions from tip and shaft (Figure 6.5).

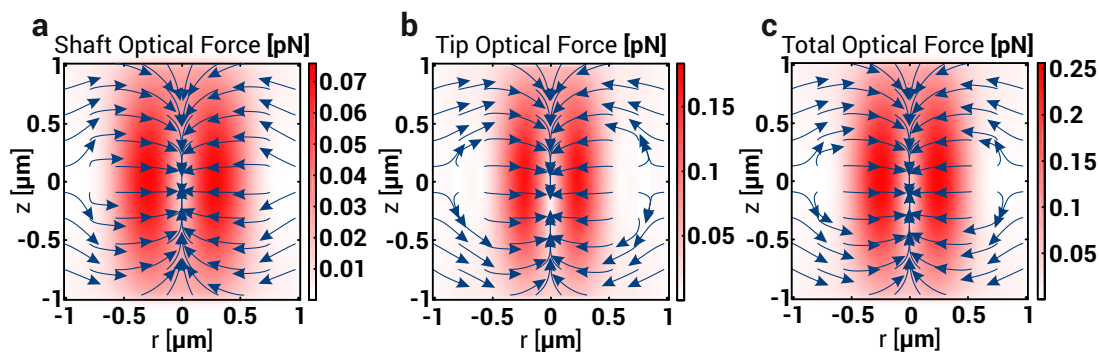


Figure 6.5 – Optical trapping of Janus nanoparticles. (a) Both the gold tip as well as the alumina shaft (b) are subject to an attractive force field when exposed to a 1064 nm focused laser beam. Summing up both force fields yielded the total force field the nanopen was exposed to (c). Here, the spatial shift between tip and shaft was taken into account. The force fields were calculated using the T-Matrix method (cf. Section 3.2.2). A laser power of 14 mW and an NA of 1.0 were assumed. The alumina shaft had a length of 500 nm and, like the gold nanoparticle, a diameter of 80 nm.

Due to the attractive contributions to the force field from both shaft and tip, the total trapping force acting on a JNP was stronger than for a conventional gold nanoparticle. Comparing the maximum force in Figure 6.5a and c, it follows that the shaft increased the total tweezing force at the same laser power by 43%, which enhances optical trapping.

To experimentally quantify the improved tweezing properties, the spatial displacement of a JNP in an optical trap was measured and compared to a normal spherical gold particle (AuNP) of the same diameter (Figure 6.6). This was done by recording a video with 5000 frames using a high framerate CCD detector (Andor iXON Ultra 897, Andor Technology Ltd., UK). The exact lateral position of the particle was determined with subnanometer precision by fitting a Gaussian in both x - and y -direction over the intensity distribution that represents the particle. For the case of the JNP it has to be taken into account that the measured position represents the one of the plasmonic tip. By plotting a histogram of the spatial distribution, the standard deviation of the displacement was determined by fitting a Gaussian curve (Figure 6.6a, c).

The nanopen was assumed to be vertical in the trap with the plasmonic tip pointing away from the light source. This alignment is energetically most favorable since it is streamlined with the incoming photon flux. For micron sized particles in an optical trap the same alignment was reported.⁹ The lateral standard deviation σ of the nanopen in the trap was found to be 40 nm (Figure 6.6a), which was significantly less than for the gold nanoparticle with 58 nm (Figure 6.6c). The 2D histograms visualize the enhanced confinement of the JNP compared to the gold nanoparticle (Figure 6.6b,d). From σ one can deduce the trap stiffness κ , which

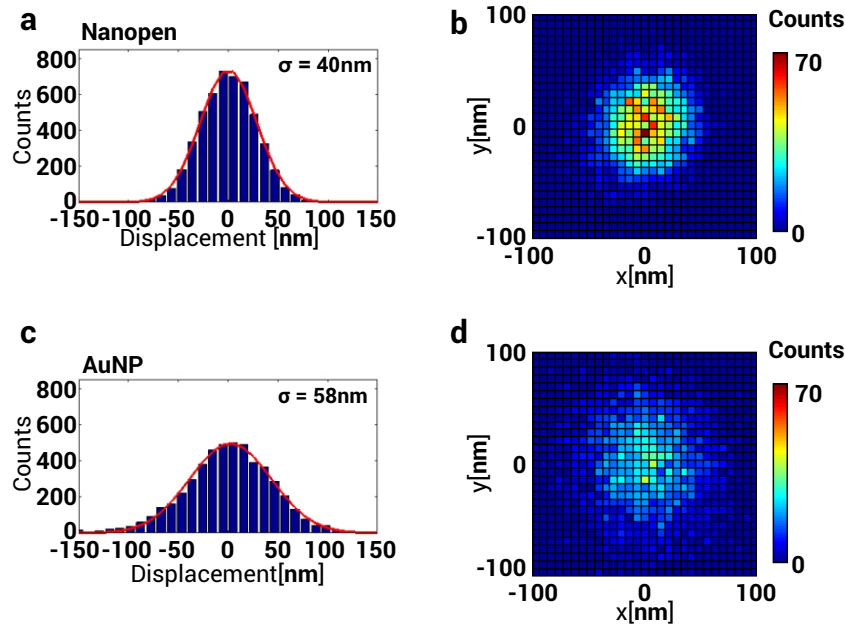


Figure 6.6 – Lateral confinement of trapped JNPs and gold nanoparticles. (a) 1D histogram of a trapped JNP from a series of 5000 frames showing a standard deviation of 40 nm. (b) 2D histogram of the same dataset visualizing the high spatial confinement of the nanopen. (c) 1D histogram of a trapped gold nanoparticle with a diameter of 80 nm from a series of 5000 frames showing a standard deviation of 58 nm. The 2D histogram of the same data set (d) shows that the AuNP was much less confined than the nanopen. Both particles were trapped at a laser power of 43 mW and with an $NA = 1$.

is a common parameter to quantify the quality of an optical trap.²¹ Here, the restoring force in an optical trap is considered as a Hookean spring. Then the linear relationship holds

$$F_{\text{trap}}(t) = \kappa \cdot x(t). \quad (6.1)$$

Hence, the restoring force increases linearly with the deflection of the particle $x(t)$. Several methods to determine the trap stiffness have been published. Dienerowitz *et al.* gave a comprehensive overview on this topic.²¹ Within the framework of this thesis, one of the more intuitive approaches, namely the equipartition theorem, was used.^{193,194}

In this approach, the particle is assumed small and the trapping potential harmonic, which is the case for trapped nanoparticles. Then the motion of the particle can be described using the Ornstein-Uhlenbeck modification of the Langevin equation:¹⁹⁵

$$m\ddot{x}(t) = -\kappa x(t) - \gamma\dot{x} + \xi(t). \quad (6.2)$$

Here, κ is the linear spring constant that can be identified as the trap stiffness (cf. Equation 6.1). $\xi(t)$ is a Gaussian noise term and γ the viscous damping constant of the medium. For the case of low Reynolds numbers as it is the case here due to the small length scales and

velocities involved,⁹⁵ the inertia term $m\ddot{x}(t)$ can be neglected, yielding the *overdamped Langevin equation*:

$$\dot{x} = -\frac{\kappa}{\gamma}x(t) + \xi(t). \quad (6.3)$$

Deriving a positional distribution $W(x)$ in a harmonic potential $V(x) = \kappa x^2/2$ then yields:

$$W(x) = A \cdot \exp\left(\frac{V(x)}{k_B T}\right) = A \cdot \exp\left(\frac{\kappa x^2}{2k_B T}\right). \quad (6.4)$$

This resembles the Gaussian distribution that is fitted in Figure 6.6a and c, where the standard deviation σ is identified. The trap stiffness was obtained through:

$$\kappa = \frac{k_B T}{\sigma^2} \quad (6.5)$$

The trap stiffnesses calculated for the gold nanoparticle and the nanopen were respectively $1.4 \mu\text{Nm}^{-1}$ and $2.8 \mu\text{Nm}^{-1}$ when averaging over x - and y -direction. Hence, the alumina shaft attached to the particle led to a doubling of the trap stiffness at the same laser power, which is a major advantage for power sensitive manipulation experiments. This is even more than twice as much as it would be expected from the 43% increase in trapping force calculated in Figure 6.5. A possible explanation for this could be thermal dissipation effects which were not considered here. For the calculation of the trap stiffness, heating of the particle was neglected assuming the particle at room temperature (293 K). In an optical trap plasmonic nanoparticles heat up, which reduces the trap stiffness.²⁷ The JNP would stay slightly colder than the gold nanoparticle due to additional heat dissipation from the non-heated shaft, thus reducing the measured trap stiffness of the gold nanoparticle.

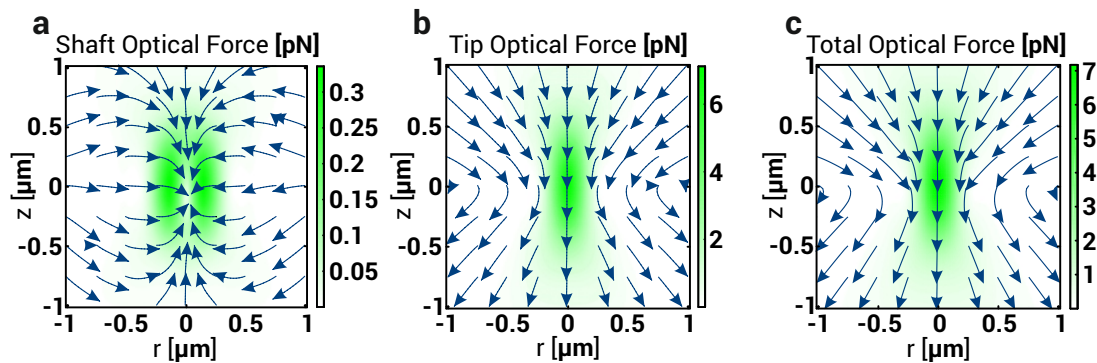


Figure 6.7 – Optical forces on Janus nanoparticles at resonance. (a) The optical force field acting on the alumina shaft at $\lambda = 532 \text{ nm}$ was attractive in contrast to the field for the gold nanoparticle tip, which was repulsive (b). However, the repulsive force field outweighs the attractive one, which is why the total force field (c) was repulsive. The assumed laser power was 6.84 mW .

When considering the JNP exposed to a focused laser beam with a wavelength close to its plasmon resonance, the behavior was differently. Calculations showed an attractive force field for the contribution of the shaft (Figure 6.7a) and a repulsive force field for the tip (Figure 6.7b). However, the attractive contribution of the shaft was more than one magnitude weaker and hence negligible. The resulting force field (Figure 6.7c) was therefore strongly repulsive. Thus, very much like conventional gold nanoparticles (Section 2.1.2), JNPs can be both trapped and printed depending on the incident laser wavelength.

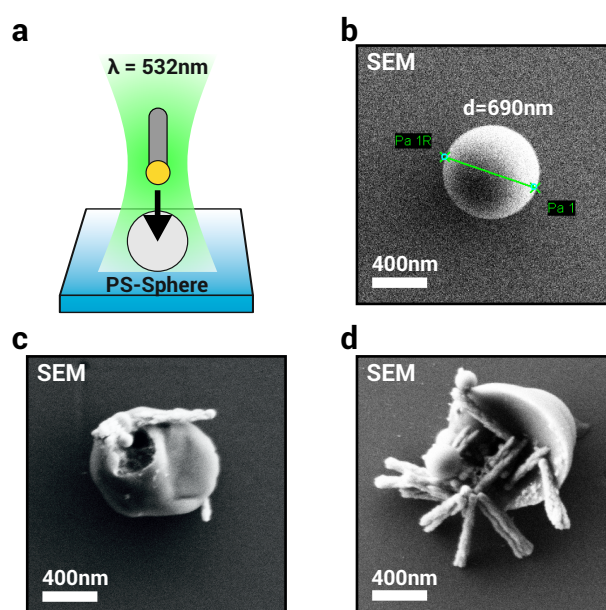


Figure 6.8 – Targeting submicron sized particles *via* optical printing. (a) The polystyrene (PS) beads with a diameter of 690 nm (b) were targeted by printing a JNP onto them using a 532 nm laser. Both single (c) and multiple (d) JNPs could be printed onto a single PS sphere proving the high spatial control when printing single JNPs.

An experiment targeting 690 nm polystyrene (PS) beads illustrates the high level of spatial control when printing nanopens (Figure 6.8). This is crucial for targeted molecular delivery approaches on biological cells, as cell organelles can have sizes below one micron. The PS beads were deposited on the glass substrate *via* drop casting. A solution containing the JNPs was then put onto the substrate. By focusing the 532 nm laser beam onto the PS beads, JNPs were deposited directly on top of them. Deposition of a single (Figure 6.8c) and multiple nanopens (Figure 6.8d) proved an easy task. This demonstrates the very good spatial control for printing JNPs. Hence, targeting submicron sized objects by printing nanopens is possible.

6.3 Moving JNPs within an optical trap by plasmonic heating induced thermophoresis

Up to this point only optical forces acting on the nanopen have been considered. However, as explained in Section 2.4, optical forces acting on plasmonic nanoparticles always come with a significant amount of heating due to light absorption (Figure 6.9a). For laser light with a wavelength of 1064 nm, a JNP is far from its plasmon resonance, however the absorption cross section is not zero but $2 \times 10^{-4} \mu\text{m}^2$ (Figure 6.9b). This leads to a heating power density of $5.4 \times 10^{15} \text{ mW/m}^3$ at a laser power of 14 mW. On this basis, a spatially resolved temperature increase with a maximum value of $\Delta T = 3 \text{ K}$ could be calculated according to Section 3.2.3. The shape of the JNP shaft in Figure 6.3a appears highly non-crystalline as crystalline Al_2O_3 (sapphire) would appear in a hexagonal crystal structure. Hence, material parameters for amorphous alumina were used for calculations. In contrast to sapphire, amorphous alumina has a more than 10-fold reduced thermal conductivity.¹⁹⁶ This leads to the temperature increase being highly confined to the gold nanoparticle tip (Figure 6.9b). The dielectric end of the nanopen on the other hand stayed at room temperature yielding a temperature gradient over the entire JNP of $4.6 \times 10^6 \text{ K m}^{-1}$.

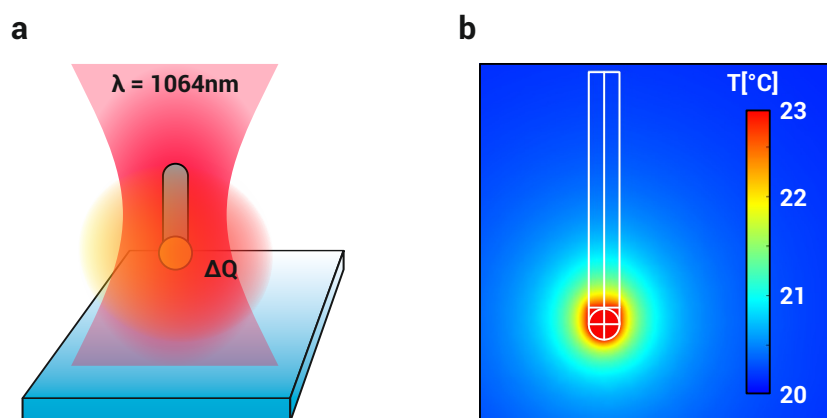


Figure 6.9 – Temperature distribution of a nanopen in an optical trap. (a) The gold tip of the JNP heated up in an optical tweezer due to the absorbed laser irradiation. (b) This leads to a temperature gradient along the JNP since only the tip heated up and the shaft did not. The temperature gradient was $4.6 \times 10^6 \text{ K m}^{-1}$ for an incident laser power of 14 mW and an NA of 1.0.

This leads to the emergence of a thermophoretic force as reported previously for micron sized particles.^{9,10,11} In those approaches, modelling the Janus particle absorption was difficult due to the grainy nature of the thin gold film. The magnitude of the thermophoretic force depends mainly on the temperature gradient. In the present work, a calculated temperature gradient for a Janus particle in an optical trap subject to thermophoresis was reported for the first time, making it possible to estimate the thermophoretic force quantitatively. Using

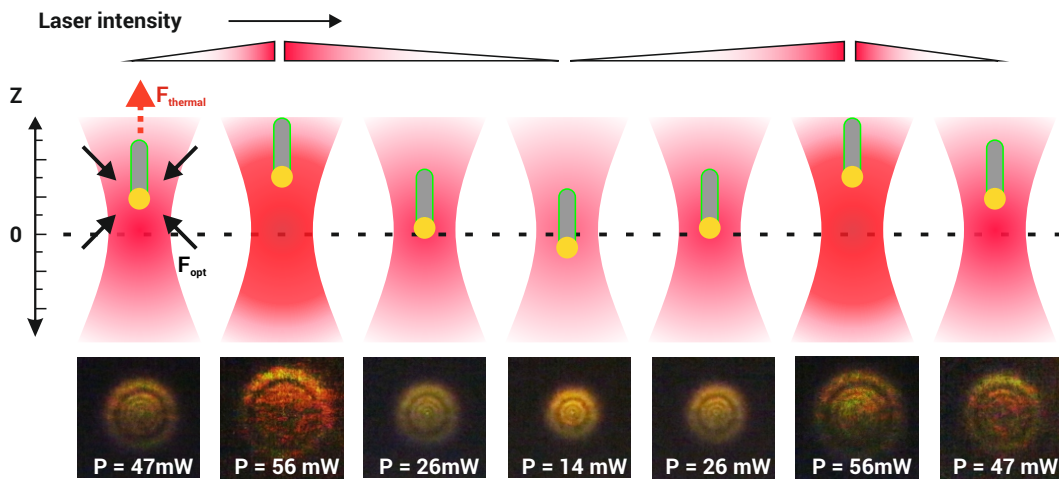


Figure 6.10 – Moving JNPs within an optical trap with plasmonic heating induced thermophoresis. An initially trapped JNP could be vertically moved inside an optical trap by increasing and decreasing the laser intensity. This led to an increase and decrease of their observed diffraction pattern diameter as shown in the DFM images in the lower panel.

the calculated temperature gradient and Equation 2.37 in combination with the *McNab-Meisen correction* (cf. Section 2.6), the thermophoretic force was calculated to be 3 pN. This is enough to push the particle out of the trapping position as the restoring force (the trapping force) is about one magnitude smaller.

Due to the enhanced scattering of the gold tip, the nanopens aligned with the gold tip pointing downwards when the laser was coupled from above. This is in accordance with the previous experiments on micron sized JNPs.⁹ This led to an upward motion when increasing the laser power due to an increase of the temperature gradient and hence the thermophoretic force (Figure 6.10). When lowering the laser power, the particle moved down again, rendering the entire process fully reversible.

This vertical movement could be observed in the microscope as a change in the diameter of the nanopen diffraction pattern (Figure 6.10 bottom). The further the nanopen moved up, the larger the diameter of the ring shaped pattern became. A calibration curve according to Speidel *et al.*¹⁹⁷ was recorded in order to translate changes in diameter to a movement along the optical axis (Figure 6.11).

For this calibration, the JNPs were attached to a glass substrate. By vertically moving the stage in controlled steps of 2.52 μm the linear dependence of the diffraction ring diameter to the relative vertical position of $(0.046 \pm 0.001) \mu\text{m}/\text{pixel}$ was obtained, where d is the diameter in pixels of the camera. The outermost ring diameter was taken for all measurements. For very small vertical shifts, the diameter of the outermost ring became hard to determine, since the individual rings merged into each other. Hence for the manipulation experiments, the laser

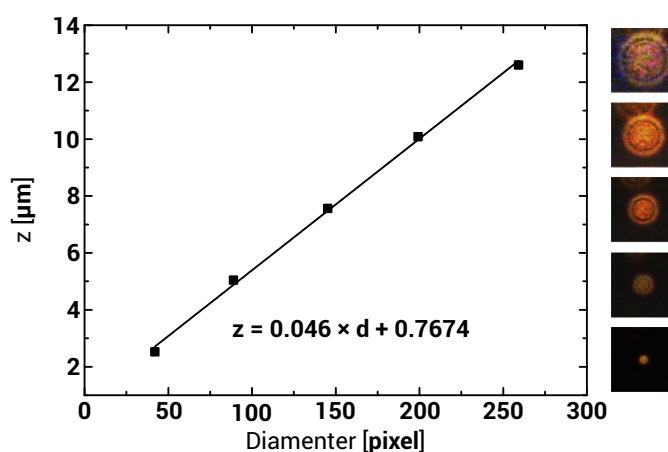


Figure 6.11 – Calibration of the JNP z -position versus the diameter of its diffraction rings. The z -position is determined by fixing JNPs on a substrate and moving the microscope stage in $2.52 \mu\text{m}$ steps upwards. The relation between z -position and diffraction ring diameter is determined by using a linear fit of the measured data. The corresponding dark field images are shown on the right side.

focus was shifted slightly above the focal plane of the microscope by prefocusing the laser beam with putting a lens with a focal length of 500 nm into its path.

This calibration allowed to quantify the vertical movement of the nanopen. The vertical position of an individual JNP could be tuned over a range of $4 \mu\text{m}$ by adjusting the laser power below the objective from 14 mW to 56 mW , while maintaining high positional control (Figure 6.12). The process was fully reversible and symmetric for upward and downward movements.

A hysteresis in the z -movement as it was reported for the micron sized Janus particles⁹ was not observed. This can be explained when considering the vertical beam profile published by Nedev *et al.*⁹ as it is shown in Figure 2.14. For the nanopen manipulation, the same laser

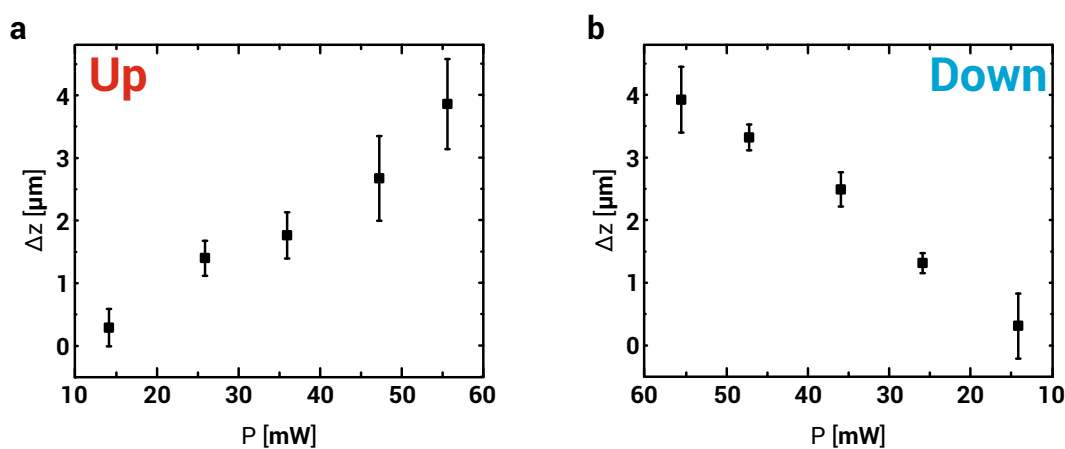


Figure 6.12 – Up- and downward movement of a nanopen in an optical trap. By tuning the laser power in a range of 14 mW to 56 mW , the nanopen was moved up- and downwards within a range of $4 \mu\text{m}$.

and objective combination was used and hence the beam profile looked exactly the same. Due to self interference, there was an intensity minimum around $4\ \mu\text{m}$ above the focal plane and a maximum at $6\ \mu\text{m}$. This is the reason for the hysteresis observed for micron sized Janus particles. The minimum had a height of about $1\ \mu\text{m}$. For the case of the nanopens this minimum could not be overcome, since they are only about half a micron in length. Hence, when moving the JNPs more than $4\ \mu\text{m}$ in z -direction, the laser intensity became too low to keep them inside the trap, which is in accordance with the experimental observation of a maximum lift of $4\ \mu\text{m}$. Therefore, the JNPs could not be moved into this higher order maximum and no hysteresis was observed.

As described in Section 2.6, the magnitude of the vertical movement also depends on the salinity of the surrounding medium due to thermo-osmotic and thermo-electric effects in the surrounding of the particle. Like Simoncelli *et al.* reported,¹⁰ the lift per mW laser power was reduced when the salinity was increased by adding (NaCl) to concentrations of 10 mM and 25 mM. However, damping of the thermophoretic force was much weaker, as the specific lift only decreased by a factor of 7.7% compared to 40% for the micron sized spherical Janus particles. This can be interpreted as the rod-shaped geometry disturbing the formation of screening layers around the particle, which would ideally be spherical. Hence, the nanopen geometry seems to be less susceptible to thermo-osmotic effects.

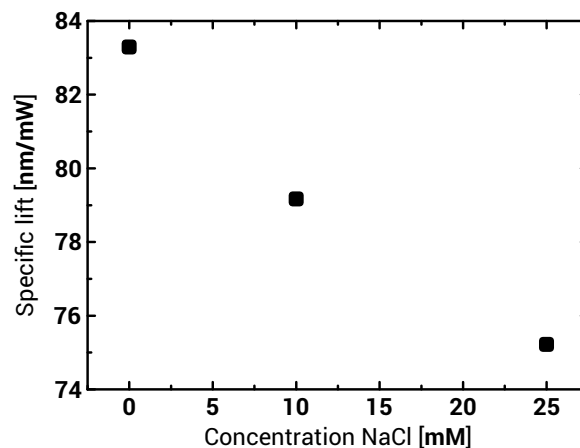


Figure 6.13 – Salinity dependence of the vertical movement magnitude. The average vertical displacement of a trapped JNP by increasing the laser power from 25 mW to 40 mW decreased when increasing the concentration of NaCl from 0 mM to 25 mM.

6.4 JNPs as carriers for the optical injection of biomolecules into cells

The foundation for the thermophoretic lift described in the previous section is the optically induced temperature gradient of JNPs in an optical trap. When using nanopens as a shuttle for biomolecules, this inhomogeneous temperature distribution comes into play as well. Here it is important that the temperature stays low enough to avoid the thermal degradation of biomolecules at least on one part of the particle. Hence in the following, the inhomogeneous heating of JNPs is investigated for the case of resonant laser illumination.

Inhomogeneous heating of JNPs under resonant laser illumination

As described in the previous section, the temperature increase of the nanopen in an optical trap was relatively moderate with just 3 K at 14 mW at the tip. However, under resonant illumination, the temperature increase was much stronger due to the drastically enhanced absorption cross section of the gold tip leading to a calculated temperature increase of 900 K at the tip when irradiated at 6.4 mW (Figure 6.14). Because of the relatively poor heat conductivity of the amorphous alumina, the dielectric end of the JNP only heated up to 88 °C. This results in a temperature gradient of $1.7 \times 10^9 \text{ K m}^{-1}$.

In order to experimentally prove the inhomogeneous heating of JNPs under resonant laser illumination, a control experiment was devised, curing a polymer precursor *via* plasmonic heating analogous to an approach previously published by Fedoruk *et al.*⁷ Here, a glass cover slide was decorated with JNPs through drop-casting, which were then covered with a layer

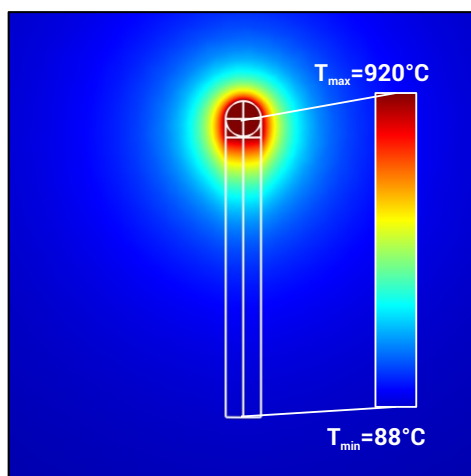


Figure 6.14 – Calculated temperature distribution around a JNP heated with a 532 nm laser at 6.8 mW. The gold tip heated up to 920 °C while the dielectric end stays relatively cold with 88 °C resulting in a temperature gradient of $1.7 \times 10^9 \text{ K m}^{-1}$.

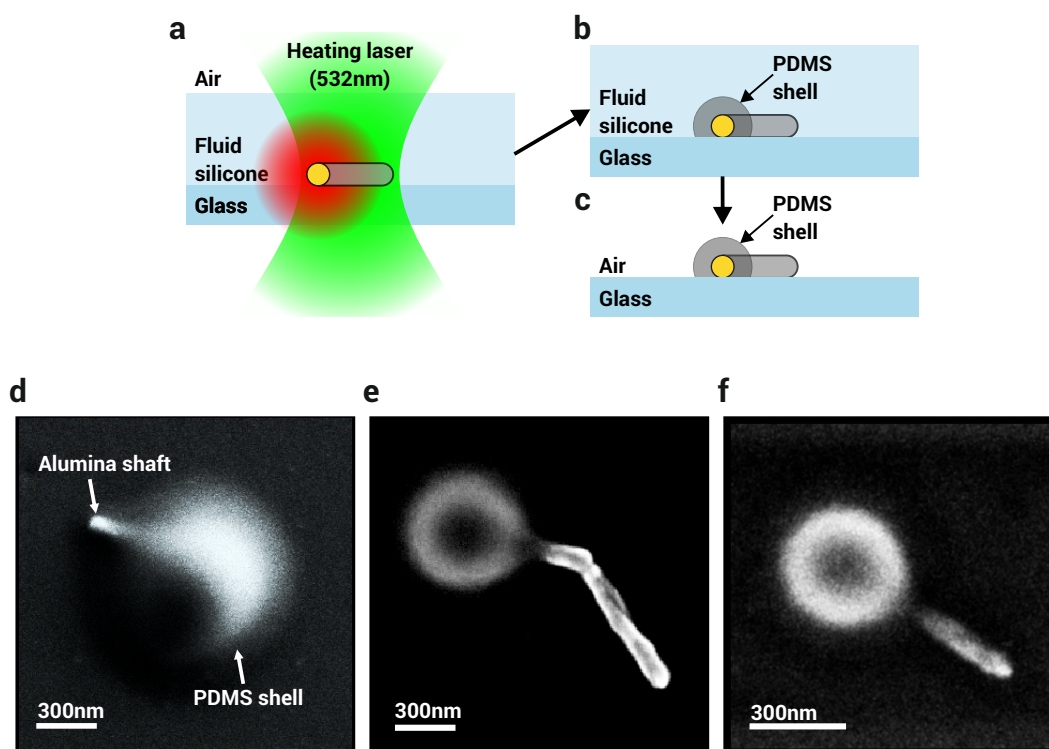


Figure 6.15 – Inhomogeneous heating of JNPs. (a) JNPs were placed on a substrate and covered with a heat curable silicon precursor. (b) Irradiating with a laser resonant to the plasmon led to local curing of the precursor. (c) The structure was developed leaving it exposed to air, allowing SEM analysis (d-f). It can be seen that the alumina shaft stuck out of the PDMS hemisphere. Hence, the heat source was localized at the plasmonic tip.

of a heat curable Polydimethylsiloxane (PDMS) precursor mixture (Sylgard 184, Dow Corning, USA) *via* spin coating. The polymer precursor is transparent and hence the JNPs could be detected in the DFM and targeted with a resonant focused laser beam (Figure 6.15a). This led to plasmonic heating at the gold tip and subsequent thermal curing of the PDMS precursor (Figure 6.15b). Afterwards, the structure was developed by rinsing away the excess precursor solution using an organic nonpolar solvent like Hexane (Figure 6.15c). SEM microscopy of the treated JNPs revealed a PDMS shell centered around the plasmonic tip, while the alumina shaft was sticking out of the PDMS shell (Figure 6.15d-f). Since Fedoruk *et al.* demonstrated a linear dependence of the shell size on the incident laser power, the size of the PDMS shell can be seen as a nanoscale map of the heat power density that was experienced by the nanopen. Hence, this proof of principle experiment shows that the strong temperature increase is localized to the plasmonic tip of the particle whereas the dielectric shaft stays relatively cold.

Delivery of DNA into living cells by JNP injection

As described before, the approach by Li *et al.* would destroy a biomolecular functionalization attached to the particles. Therefore, injecting JNPs instead of solid gold nanoparticles provides

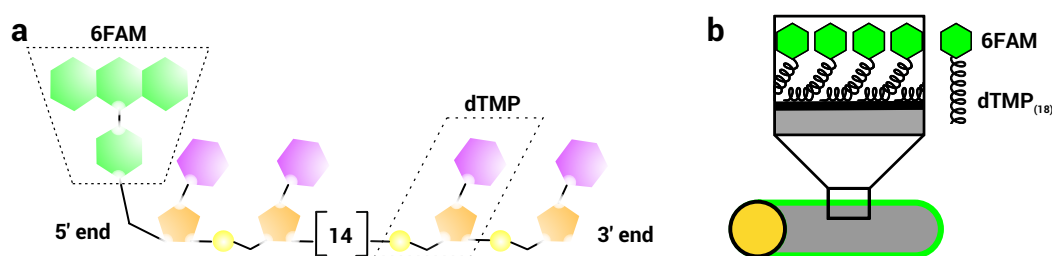


Figure 6.16 – Functionalization of JNPs with fluorescently labelled ssDNA. (a) The dye functionalized DNA molecule chosen for the functionalization. It features a 6-Carboxyfluorescein (6-FAM) molecule at its 5' terminus, which facilitated detection in a fluorescence microscope, connected to a chain of 18 deoxythymidine monophosphate (dTMP) groups towards its 3' end. (b) The molecules bind covalently through the thymine and phosphate groups on the surface of the alumina covering the alumina shaft.

a workaround as the alumina shaft does not heat up from the laser irradiation directly and is only heated *via* heat conduction from the gold tip. Even when assuming a temperature of 500 °C, way above the aforementioned spinoidal decomposition temperature of water required for injecting nanoparticles (320 °C) at the gold nanoparticle tip, the dielectric end of the nanopen only heated up to 57 °C. This is still low enough for many biomolecules to avoid denaturation.

Hence, this paved the way to use JNPs as a shuttle to deliver biomolecules into cells. As a proof of principle, a fluorescently labelled single stranded DNA, namely 5'-6-FAM-dTMP₍₁₈₎ 3' was chosen as a model molecule. It consists of a chain of 18 deoxythymidine monophosphate (dTMP) groups connected to the dye 6-Carboxyfluorescein (6-FAM), which allowed the detection of the molecule in a fluorescence microscope emitting at 517 nm (Figure 6.16a).

The dTMP terminus binds covalently through its thymine and phosphate polar groups to the alumina. Moreover, this surface binding remains stable even for temperatures above 100 °C.¹⁹⁸ To functionalize the nanopens, they were incubated for 3 h at 30 °C in a 2 mM 5'-6-FAM-dTMP₍₁₈₎ 3' solution while still attached to the silicon wafer. Subsequent washing with

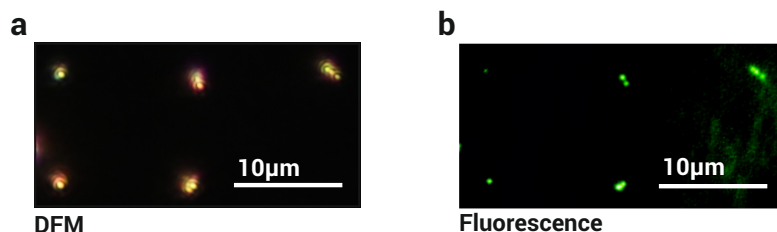


Figure 6.17 – Microscopy of ssDNA functionalized nanopens. (a) DFM image of a pattern of JNPs obtained by printing showing 1, 2, and 3 (1st row) as well as 1 and 2 (2nd row) nanopens at each spot. (b) Epi-fluorescence image of the same pattern. With both microscopical methods the number of particles at each spot could be resolved.

ultrapure water removed excess DNA from the solution. Afterwards they were sonicated in ultrapure water to disperse them in solution as described previously.

The fluorescent label on the ssDNA made the JNPs directly visible in an Epi-fluorescence microscope (cf. Section 3.1.2) unless the ssDNA is stripped off or destroyed. This is showcased in Figure 6.17, where a pattern of JNPs was printed onto a substrate and imaged *via* DFM and Epi-fluorescence microscopy using a 532 nm laser. The pattern that featured sites with 1, 2 and 3 JNPs printed next to each other could be completely resolved with both imaging techniques. Since the fluorescence signal stems from the ssDNA, Epi-fluorescence microscopy provides proof of the viability of the ssDNA injection process.

Using the thermophoretic elevator effect described previously, the JNPs could gently be positioned on top of living Chinese Hamster Ovary (CHO) cells (Figure 6.18a, see Section 3.3 for details on cell growth and handling). Compared to the placement of gold nanoparticles reported by Li *et al.*, who optically printed the particles onto the cell membrane, this process involved less heat production and was therefore less harmful for the cell membrane. In a second step a green 532 nm laser was used to create a bubble around the JNP (Figure 6.18b), which can be seen as a white flash around the JNP. It quickly formed and collapsed after turning the laser on and off, respectively. A threshold of 6.8 mW as a minimum incident laser power to achieve sufficient plasmonic heating for the creation of a hot vapor bubble

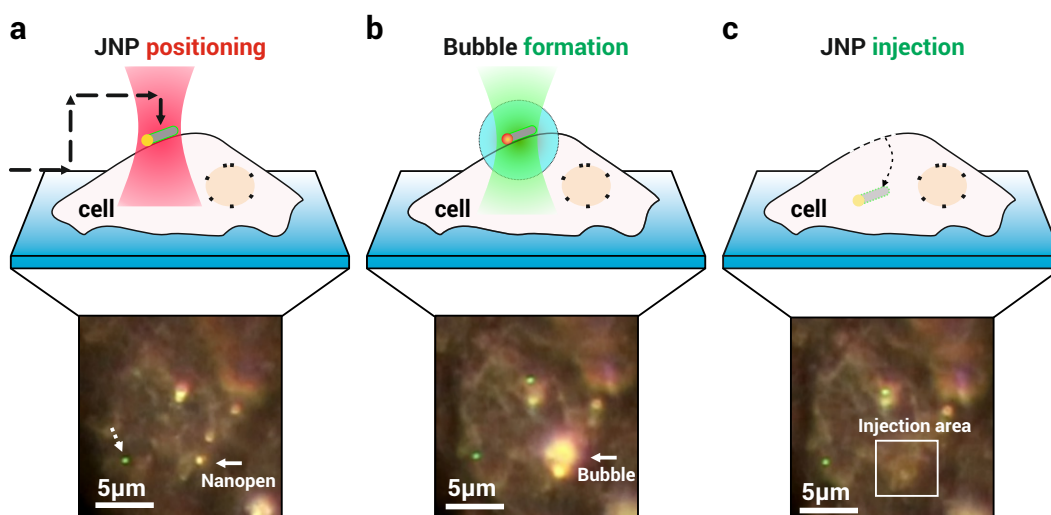


Figure 6.18 – Optical injection of nanopens into living cells. (a) JNPs were first lifted on top of the cell by elevating them in *z*-direction and softly deposited on the cell surface using a 1064 nm laser. (b) Subsequently the nanopens were irradiated with a focused 532 nm laser triggering a bubble formation and a localized cell membrane rupture that led to the injection of the particle (c). The panels below a-c show live dark field microscopy images of the positioned JNP, the bubble and the injection area. It can be seen that the particle travelled out of the focal plane, thus proving a successful injection. The green spot marked in the first DFM image was an internal reflection of the laser and does not correspond to a JNP.

was found. Through the expansion of the bubble, a small, transient hole was punctured in the cell membrane. The scattering force which acted simultaneously on the nanopen then pushed it through this hole, thus successfully completing the injection process (Figure 6.18c).

The entire sequence was monitored in real time *via* dark field microscopy. Here, the positioning using the thermophoretic elevator was another advantage since it allows the focal position to be kept constant. Hence, the cell could be observed at the same focal plane throughout the entire positioning process. During the injection the nanopen moved out of focus immediately. It could be relocated by lowering the focal plane of the microscope, which indicates that the JNP was inside the cell. Since the average pore size of the cytoskeleton meshwork within the cell is < 50 nm,¹⁹⁹ the nanopens did not diffuse freely inside the cell, but remained localized close to the injection sites.

In order to investigate the injection areas in more detail, the cells were chemically fixated to allow scanning electron microscopy (cf. Section 3.3). The images of the injection sites revealed that only very small holes slightly larger than the nanopens were formed (Figure 6.19). The vapor bubble acts as a thermal shield against the heating of the gold tip as the estimated temperature of the vapor bubble itself has been reported to be relatively low compared to the gold surface.⁷⁰ Hence, the spatial expansion of the temperature increase was minimized. This kept the thermally induced damage to both cell membrane and molecular functionalization of the JNP at a low level.

The nature of the injection site was found to depend strongly on the applied laser power. Figure 6.20 shows a comparison of two cells, one injected with a laser power of 14 mW and the other one at 50 mW. While the injection sites remained fairly small at the smaller laser power, the membrane holes became much larger when injecting at high laser powers. The membrane holes were apparently too large for the cell to be closed again, which resulted in

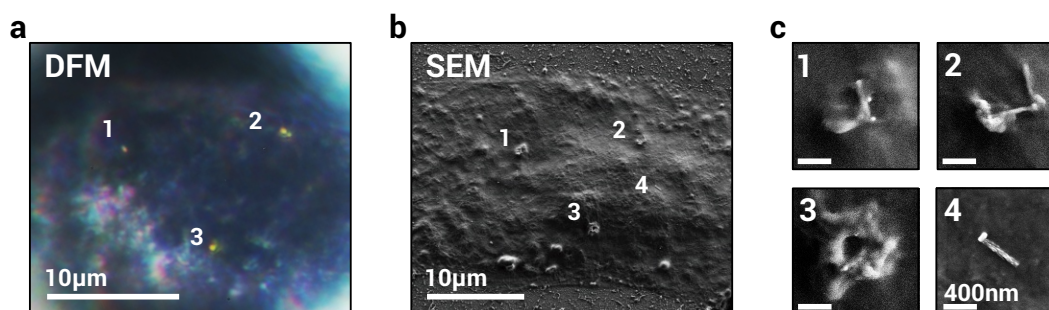


Figure 6.19 – Scanning electron microscopy of injected cells. DFM (a) and SEM (b) images of a cell injected with three JNPs. (c) The close ups 1-3 show that the membrane damage sites were very localized around the JNPs. Close up 4 shows a noninjected JNP lying on top of the membrane that is not visible in the DFM image since it was not in the same focal plane as the injected particles.

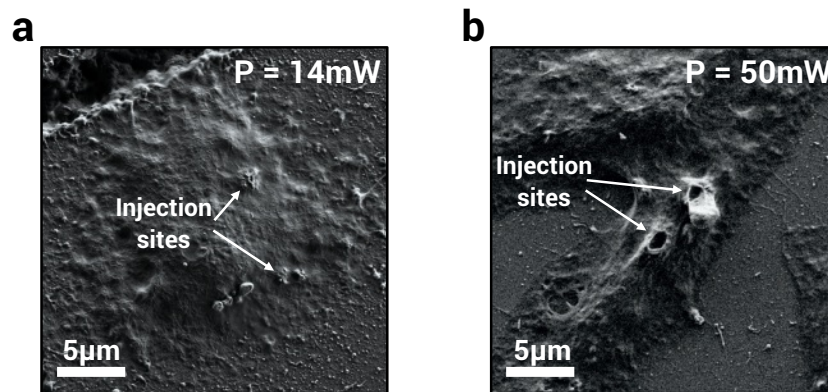


Figure 6.20 – Comparison of nanopen injection at different laser powers. (a) The JNP injection at 14 mW led to small injection sites. (b) Increasing the laser power to 50 mW however led to much larger membrane openings due to the formation of larger vapor bubbles.

the death of the cell. Thus a careful handling of the laser injection power is crucial in order to keep the cell viability at a reasonable level.

In order to check the viability of the DNA functionalization, the injected cells were imaged using Epi-fluorescence microscopy (Figure 6.21) and correlated with their corresponding DFM images. The injected nanopens were still fluorescent, meaning that at least a significant part of the ssDNA survived the injection process, thus proving that the fully optical localized delivery of DNA into living cells was successful. In order to exclude auto-fluorescence effects of the cell being responsible for the fluorescent spots, a control injection experiment with non functionalized nanopens (Figure 6.22) was carried out. Here, no spots were visible in the fluorescence microscope. Hence, the spots in the previous images stem indeed from the labelled ssDNA that survived the injection process.

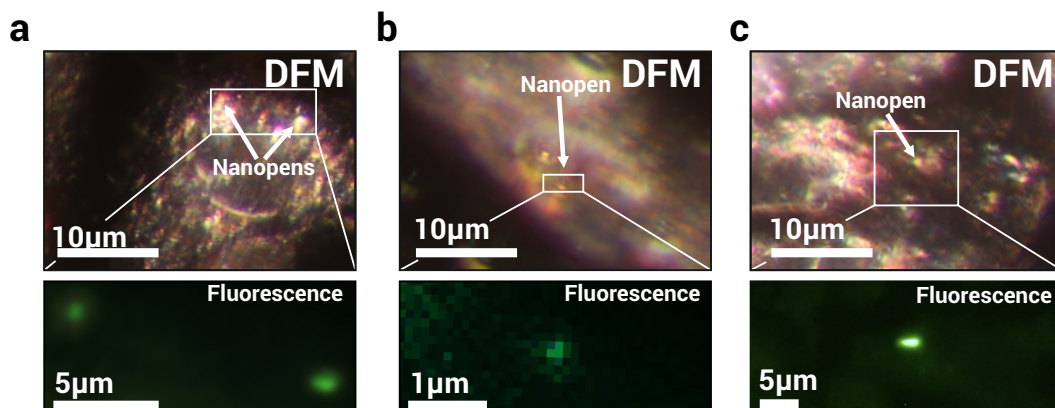


Figure 6.21 – Injection of ssDNA functionalized nanopens into living cells. (a-c) Three examples of nanopens that were injected into living cells in the dark field microscope. The pens were still visible as fluorescent spots after the injection in the Epi-fluorescence microscope. Hence, the fluorescent ssDNA functionalization was still intact after the injection.

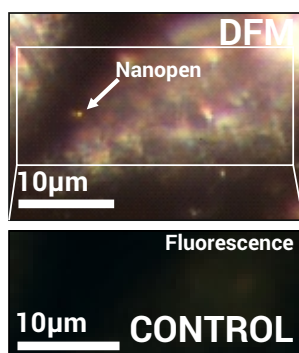


Figure 6.22 – Control experiment: Injection of non-fluorescent nanopens. Non-functionalized nanopens were injected into a living cell using the same approach as in the other experiments. Here, no fluorescence was visible at the injection sites, thus excluding enhanced self fluorescence at these spots.

To showcase the universality of the nanopen delivery approach, the experiment was repeated with an adenosine ssDNA sequence functionalized to the nanopens. It was labelled with a different dye, namely Eterneon 394/507 (E.N.). The entire sequence was 5'E.N.-dAMP₍₂₅₎3' (dAMP: 2'-deoxyadenosine-5'-monophosphate). The nanopens were functionalized and injected as previously with 5'6-FAM-dTMP₍₁₈₎3'. Polyadenine strands were chosen here since they play a key role as an anchor sequence in linking DNA to gold nanoparticles as well as quantum dots.²⁰⁰ Furthermore they form the complementary DNA base to the previously used thymine.

Also here, correlated DFM and fluorescence images exhibited a spot of enhanced fluorescence at the injection site (Figure 6.23), thus rendering the DNA delivery successful. The much higher background fluorescence can be explained by the excitation wavelength being at 394 nm where the cells exhibit a stronger autofluorescence compared to 6-FAM which absorbs at 495 nm.

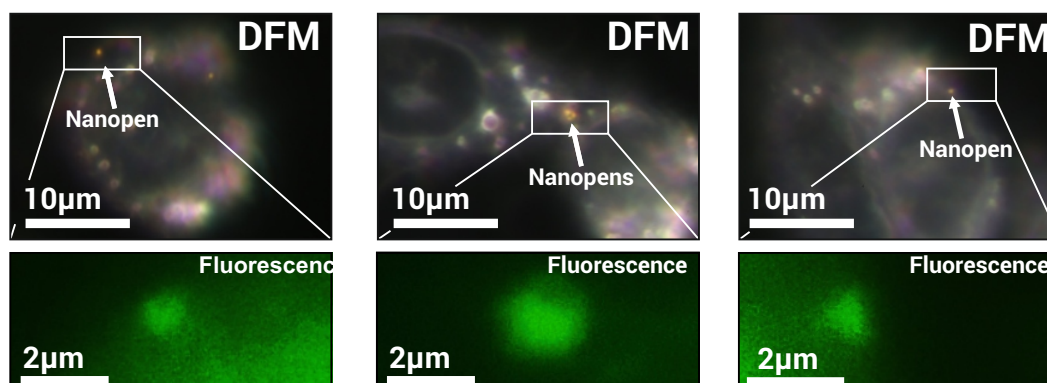


Figure 6.23 – Injection of nanopens functionalized with 5'E.N.-dAMP₍₂₅₎3' into living cells. To showcase the universal applicability of JNPs, several nanopens functionalized with a different ssDNA sequence, namely 5'E.N.-dAMP₍₂₅₎3', were injected into living CHO cells.

Summary

This chapter introduces a new material, namely plasmonic Janus nanoparticles or nanopens. They feature a plasmonic tip with a spherical 80 nm gold particle which is connected to a dielectric shaft made from amorphous aluminum oxide of the same diameter. Those two ends interact fundamentally different with light, with the plasmonic part strongly absorbing and scattering light. The dielectric shaft on the other hand only diffracts light and has a negligible absorption. The level of control in optical tweezers was even better than for conventional spherical particles due to the additional attractive force from the alumina shaft.

The localization of the light absorption on the plasmonic tip in combination with the relatively poor thermal conductivity of amorphous alumina lead to the build-up of a thermal gradient along the structure for both resonant and off-resonant illumination. Here, this property was exploited for two applications. First, the principle of thermophoretic elevation of a nanoscopic particle in an optical trap was shown for the first time. The particle position could be tuned over a range of about 4 μm along the propagation axis of the laser in an optical tweezers setup. This was applied to gently place the nanopens onto living cells as a preparation to inject the JNPs for biomolecular delivery. Here, the localization of the heating on the plasmonic tip was exploited again by functionalizing the dielectric shaft with a fluorescent ssDNA sequence. This overcomes the problem that the strong heating during an optical cell injection would destroy most biomolecules when using purely metallic particles. Fluorescence microscopy revealed that using this approach, the ssDNA survived the treatment, thus rendering the method as a potential shuttle mechanism for directed molecular delivery into single living cells. This paves the way for applications such as cell transfection, personalized medicine or drug delivery.

Chapter 7

Conclusion: Applying forces on anisotropic plasmonic nanoparticles for nanotechnological applications

The subject of this thesis was the analysis of a multitude of optically induced forces interacting with anisotropic plasmonic nanoparticles. On the one hand, the particles are subject to directly induced optical forces that occur due to the momentum transfer from incident photons. On the other hand, there are several secondary forces that occur due to fluidic interaction or heating of the particles. This is of course not an extensive list of all the forces that can act on plasmonic nanoparticles. Other contributions, which have not been part of this analysis are, for example, van der Waals or electrophoretic forces. Nevertheless, this thesis focused on disentangling and understanding how different force contributions act on plasmonic nanoparticles. This allowed their use as tools for nanotechnological applications. In this respect, a series of experiments were conducted and analyzed.

In Chapter 4 optical forces were applied to sort plasmonic particles by their plasmon resonances using repulsive scattering forces. This was realized by applying lasers of different wavelengths to a dispersion of nanoparticles with various geometries. It was found that only the particles, whose plasmonic resonance matched the incident laser beam were printed onto a glass substrate. This allowed to elucidate the origin of the peak in the NIR that appears during the reduction of Au(III) with sulfide species, a synthesis that has been a matter of debate for decades among different groups, proclaiming nanoshells, nanotriangles or nanoparticle clusters being the origin of said peak. Using the newly developed laser sorting approach, it was successfully shown that it originates from nanotriangles. Computational simulations fully explained that the spectral dynamics of the peaks stem from an initial growth and subsequent truncation and thickening of the triangles. Hence, using this approach, an end could be put

to this discussion. Furthermore, this technique could easily be employed to other syntheses or polydisperse systems in the future.

In Chapter 5, it was shown how a gold nanorod can be split up by applying a focused laser beam resonant to its longitudinal plasmon mode. The resulting structures were dimers consisting of two equally sized spheres with a distance in the subnanometer regime, as it could be seen from their optical properties. A model was employed explaining the split-up with a combination of fluidic and inhomogeneous optical forces while undergoing a surface tension driven deformation. This was the first time a controlled optically induced split-up of nanoparticles at the single nanoparticle scale was reported. This approach presents an all optical method for the fabrication of dimers with subnanometer gap distances, which is usually no easy feat. It might therefore become of interest for applications that rely on strong electric fields such a Raman or fluorescence enhancement or hot electron injection driven chemical reactions.

In Chapter 6, in addition to the morphology, also an anisotropic material composition of the particles is examined. This is achieved by introducing a new material, so-called Janus nanoparticles (JNPs) or nanopens, consisting of a plasmonic gold tip and a dielectric shaft. With a diameter of only 80 nm, they behave optically much like conventional gold nanoparticles as the tip dominates their optical response. However, the dielectric shaft led to the occurrence of a thermophoretic force that stemmed from the induced temperature gradient over the particle. Within an optical trap, it was shown that this leads to an elevation behavior with increasing laser powers. This effect was employed to place nanopens on top of living cells, where they were injected using a resonant laser. When functionalized with DNA molecules, JNPs were successfully applied as biomolecular shuttles. It was shown that the molecules to be delivered did not get destroyed at the alumina shaft. This paves the way for applications like cell transfection, sensing, drug delivery or personalized medicine.

In summary, this thesis investigates how optically induced forces interact with anisotropic particles. Anisotropy leads to a strong wavelength dependence of the optical force field. Furthermore, optical forces do not act homogeneously on anisotropic particles, which can lead to their deformation. Moreover, it has been shown that also the interaction with the medium gives a significant contribution. On the one hand, hydrodynamic drag forces acting on particles when they are optically pushed through the surrounding fluid can induce morphological changes. On the other hand, when anisotropy is extended to the material composition of the particles, temperature gradients can occur that lead to an additional thermophoretic force away from the heat source. In all experiments the forces acting on the particles were harnessed for nanotechnological applications. In particular, nanoparticles were sorted by their plasmon resonance, plasmonic dimers with subnanometer gap sizes were formed and

biomolecules were injected into cells. This showcases the immense potential of anisotropic nanoparticles for applications in a variety of fields including chemistry, materials science and biotechnology.

Bibliography

- [1] A. Ashkin. “Acceleration and Trapping of Particles by Radiation Pressure”. In: *Physical Review Letters* 24 (4 Jan. 1970), pp. 156–159. DOI: 10.1103/PhysRevLett.24.156.
- [2] A. Ashkin et al. “Observation of a Single-Beam Gradient Force Optical Trap for Dielectric Particles”. In: *Optics Letters* 11.5 (1986), pp. 288–290. DOI: 10.1364/Ol.11.000288.
- [3] A. Ashkin. “Forces of a Single-Beam Gradient Laser Trap on a Dielectric Sphere in the Ray Optics Regime”. In: *Biophysical Journal* 61.2 (1992), pp. 569–582. DOI: Doi10.1016/S0006-3495(92)81860-X.
- [4] A. Ashkin. “Optical trapping and manipulation of neutral particles using lasers”. In: *Proceedings of the National Academy of Sciences* 94.10 (1997), pp. 4853–4860.
- [5] K. Svoboda and S. M. Block. “Optical Trapping of Metallic Rayleigh Particles”. In: *Optics Letters* 19.13 (1994), pp. 930–932. DOI: Doi10.1364/Ol.19.000930.
- [6] A. S. Urban et al. “Optical trapping and manipulation of plasmonic nanoparticles: fundamentals, applications, and perspectives”. In: *Nanoscale* 6.9 (2014), pp. 4458–74. DOI: 10.1039/c3nr06617g.
- [7] M. Fedoruk et al. “Nanolithography by Plasmonic Heating and Optical Manipulation of Gold Nanoparticles”. In: *ACS Nano* 7.9 (2013), pp. 7648–7653. DOI: 10.1021/nm402124p.
- [8] M. Li, T. Lohmüller, and J. Feldmann. “Optical Injection of Gold Nanoparticles into Living Cells”. In: *Nano Letters* 15.1 (2015), pp. 770–775. DOI: 10.1021/nl504497m.
- [9] S. Nedev et al. “An Optically Controlled Microscale Elevator Using Plasmonic Janus Particles”. In: *ACS Photonics* 2.4 (2015), pp. 491–496. DOI: 10.1021/ph500371z.
- [10] S. Simoncelli et al. “Combined Optical and Chemical Control of a Microsized Photofueled Janus Particle”. In: *Small* 12.21 (2016), pp. 2854–2858. DOI: 10.1002/smll.201503712.
- [11] S. Simoncelli et al. “Stretching and Heating Single DNA Molecules with Optically Trapped Gold–Silica Janus Particles”. In: *ACS Photonics* 4.11 (2017), pp. 2843–2851. DOI: 10.1021/acsp Photonics.7b00839.

- [12] Matthew Pelton and Garnett W. Bryant. *Introduction to metal-nanoparticle plasmonics*. Vol. 5. John Wiley & Sons, 2013.
- [13] R. L. Olmon et al. “Optical dielectric function of gold”. In: *Physical Review B* 86.23 (2012). DOI: 10.1103/PhysRevB.86.235147.
- [14] S. A. Maier. *Plasmonics: Fundamentals and Applications*. Springer Science & Business Media, 2007.
- [15] P. B. Johnson and R. W. Christy. “Optical Constants of the Noble Metals”. In: *Physical Review B* 6.12 (1972), pp. 4370–4379. DOI: 10.1103/PhysRevB.6.4370.
- [16] A. Vial et al. “Improved analytical fit of gold dispersion: Application to the modeling of extinction spectra with a finite-difference time-domain method”. In: *Physical Review B* 71.8 (2005). DOI: 10.1103/PhysRevB.71.085416.
- [17] C. F. Bohren. “How can a particle absorb more than the light incident on it?” In: *American Journal of Physics* 51.4 (1983), pp. 323–327. DOI: 10.1119/1.13262.
- [18] P. Bharadwaj, B. Deutsch, and L. Novotny. “Optical Antennas”. In: *Advances in Optics and Photonics* 1.3 (2009), pp. 438–483. DOI: 10.1364/AOP.1.000438.
- [19] V. Myroshnychenko et al. “Modelling the optical response of gold nanoparticles”. In: *Chemical Society Reviews* 37.9 (2008), pp. 1792–1805. DOI: 10.1039/b711486a.
- [20] G. Mie. “Beiträge zur Optik trüber Medien, speziell kolloidaler Metallösungen”. In: *Annalen der Physik* 330.3 (1908), pp. 377–445. DOI: 10.1002/andp.19083300302.
- [21] M. Dienerowitz, M. Mazilu, and K. Dholakia. “Optical manipulation of nanoparticles: a review”. In: *Journal of Nanophotonics* 2 (2008). DOI: 10.1117/1.2992045.
- [22] R. R. Agayan et al. “Optical trapping near resonance absorption”. In: *Applied Optics* 41.12 (2002), pp. 2318–2327. DOI: 10.1364/Ao.41.002318.
- [23] L. Novotny and B. Hecht. *Principles of nano-optics*. Cambridge university press, 2012.
- [24] A. Ashkin and J. M. Dziedzic. “Optical Trapping and Manipulation of Viruses and Bacteria”. In: *Science* 235.4795 (1987), pp. 1517–1520. DOI: DOI10.1126/science.3547653.
- [25] P. M. Hansen et al. “Expanding the optical trapping range of gold nanoparticles”. In: *Nano Letters* 5.10 (2005), pp. 1937–1942. DOI: 10.1021/nl051289r.
- [26] M. Pelton et al. “Optical trapping and alignment of single gold nanorods by using plasmon resonances”. In: *Optics Letters* 31.13 (2006), pp. 2075–2077. DOI: Doi10.1364/OL.31.002075.
- [27] C. Zensen et al. “Pushing nanoparticles with light - A femtonewton resolved measurement of optical scattering forces”. In: *APL Photonics* 1.2 (2016). DOI: 10.1063/1.4945351.

- [28] A. Ohlinger et al. “Optically Trapped Gold Nanoparticle Enables Listening at the Microscale”. In: *Physical Review Letters* 108.1 (2012). DOI: 10.1103/PhysRevLett.108.018101.
- [29] A. S. Urban et al. “Laser Printing Single Gold Nanoparticles”. In: *Nano Letters* 10.12 (2010), pp. 4794–4798. DOI: 10.1021/nl1030425.
- [30] S. Nedev et al. “Optical Force Stamping Lithography”. In: *Nano Letters* 11.11 (2011), pp. 5066–5070. DOI: 10.1021/nl203214n.
- [31] J. Do et al. “Two-color laser printing of individual gold nanorods”. In: *Nano Letters* 13.9 (2013), pp. 4164–8. DOI: 10.1021/nl401788w.
- [32] A. Babynina et al. “Bending Gold Nanorods with Light”. In: *Nano Letters* 16.10 (2016), pp. 6485–6490. DOI: 10.1021/acs.nanolett.6b03029.
- [33] J. W. Liaw et al. “Plasmon-enhanced optical bending and heating on V-shaped deformation of gold nanorod”. In: *Applied Physics A - Materials Science & Processing* 124.1 (2018). DOI: 10.1007/s00339-017-1433-0.
- [34] G. G. Stokes. “On the theories of the internal friction of fluids in motion, and of the equilibrium and motion of elastic solids”. In: *Transactions of the Cambridge Philosophical Society* 8 (1880).
- [35] A. M. Jaffe. “The millennium grand challenge in mathematics”. In: *Notices of the AMS* 53.6 (2006).
- [36] M. Hu et al. “Gold nanostructures: engineering their plasmonic properties for biomedical applications”. In: *Chemical Society Reviews* 35.11 (2006), pp. 1084–1094. DOI: 10.1039/b517615h.
- [37] J. Aizpurua et al. “Optical properties of coupled metallic nanorods for field-enhanced spectroscopy”. In: *Physical Review B* 71.23 (2005). DOI: 10.1103/PhysRevB.71.235420.
- [38] A. M. Gobin et al. “Near-infrared resonant nanoshells for combined optical imaging and photothermal cancer therapy”. In: *Nano Letters* 7.7 (2007), pp. 1929–1934. DOI: 10.1021/nl070610y.
- [39] A. J. Blanch, M. Doblinger, and J. Rodriguez-Fernandez. “Simple and Rapid High-Yield Synthesis and Size Sorting of Multibranched Hollow Gold Nanoparticles with Highly Tunable NIR Plasmon Resonances”. In: *Small* 11.35 (2015), pp. 4550–9. DOI: 10.1002/smll.201500095.
- [40] Y. G. Sun and Y. N. Xia. “Shape-controlled synthesis of gold and silver nanoparticles”. In: *Science* 298.5601 (2002), pp. 2176–2179. DOI: 10.1126/science.1077229.

- [41] L. Scarabelli et al. “Monodisperse Gold Nanotriangles: Size Control, Large-Scale Self-Assembly and Performance in Surface-Enhanced Raman Scattering”. In: *ACS Nano* 8.6 (2014), pp. 5833–5842.
- [42] P. K. Jain, W. Huang, and M. A. El-Sayed. “On the Universal Scaling Behavior of the Distance Decay of Plasmon Coupling in Metal Nanoparticle Pairs: A Plasmon Ruler Equation”. In: *Nano Letters* 7.7 (2007), pp. 2080–2088. DOI: 10.1021/nl071008a.
- [43] P. Nordlander et al. “Plasmon Hybridization in Nanoparticle Dimers”. In: *Nano Letters* 4.5 (2004), pp. 899–903. DOI: 10.1021/nl049681c.
- [44] W. T. Simpson and D. L. Peterson. “Coupling Strength for Resonance Force Transfer of Electronic Energy in Van der Waals Solids”. In: *The Journal of Chemical Physics* 26.3 (1957), pp. 588–593. DOI: 10.1063/1.1743351.
- [45] C. Tabor, D. Van Haute, and M. A. El-Sayed. “Effect of Orientation on Plasmonic Coupling between Gold Nanorods”. In: *ACS Nano* 3.11 (2009), pp. 3670–3678. DOI: 10.1021/nn900779f.
- [46] R. Esteban et al. “Bridging quantum and classical plasmonics with a quantum-corrected model”. In: *Nature Communications* 3 (2012), p. 825. DOI: 10.1038/ncomms1806.
- [47] F. J. G. de Abajo. “Nonlocal Effects in the Plasmons of Strongly Interacting Nanoparticles, Dimers, and Waveguides”. In: *Journal of Physical Chemistry C* 112.46 (2008), pp. 17983–17987. DOI: 10.1021/jp807345h.
- [48] S. Raza et al. “Nonlocal optical response in metallic nanostructures”. In: *Journal of Physics - Condensed Matter* 27.18 (2015). DOI: 10.1088/0953-8984/27/18/183204.
- [49] T. V. Teperik et al. “Robust Subnanometric Plasmon Ruler by Rescaling of the Nonlocal Optical Response”. In: *Physical Review Letters* 110.26 (2013). DOI: ARTN26390110.1103/PhysRevLett.110.263901.
- [50] K. J. Savage et al. “Revealing the quantum regime in tunnelling plasmonics”. In: *Nature* 491.7425 (2012), pp. 574–577. DOI: 10.1038/nature11653.
- [51] W. Q. Zhu et al. “Quantum mechanical effects in plasmonic structures with subnanometre gaps”. In: *Nature Communications* 7 (2016). DOI: 10.1038/ncomms11495.
- [52] R. Esteban et al. “A classical treatment of optical tunneling in plasmonic gaps: extending the quantum corrected model to practical situations”. In: *Faraday Discussions* 178.0 (2015), pp. 151–183. DOI: 10.1039/C4FD00196F.
- [53] J. M. Pitarke, F. Flores, and P. M. Echenique. “Tunneling Spectroscopy - Surface Geometry and Interface Potential Effects”. In: *Surface Science* 234.1-2 (1990), pp. 1–16. DOI: 10.1016/0039-6028(90)90659-V.

- [54] A. O. Govorov and H. H. Richardson. “Generating heat with metal nanoparticles”. In: *Nano Today* 2.1 (2007), pp. 30–38. DOI: 10.1016/S1748-0132(07)70017-8.
- [55] V. P. Zhukov et al. “Corrected local-density approximation band structures, linear-response dielectric functions, and quasiparticle lifetimes in noble metals”. In: *Physical Review B* 64.19 (2001). DOI: 10.1103/PhysRevB.64.195122.
- [56] K. Puech et al. “Investigation of the Ultrafast Dephasing Time of Gold Nanoparticles Using Incoherent-Light”. In: *Chemical Physics Letters* 247.1-2 (1995), pp. 13–17. DOI: 10.1016/0009-2614(95)01196-1.
- [57] W. S. Fann et al. “Electron Thermalization in Gold”. In: *Physical Review B* 46.20 (1992), pp. 13592–13595. DOI: 10.1103/PhysRevB.46.13592.
- [58] C. K. Sun et al. “Femtosecond-Tunable Measurement of Electron Thermalization in Gold”. In: *Physical Review B* 50.20 (1994), pp. 15337–15348. DOI: 10.1103/PhysRevB.50.15337.
- [59] J. Hodak, I. Martini, and G. V. Hartland. “Ultrafast study of electron–phonon coupling in colloidal gold particles”. In: *Chemical Physics Letters* 284.1 (1998), pp. 135–141. DOI: 10.1016/S0009-2614(97)01369-9.
- [60] H. E. Elsayedali et al. “Femtosecond Thermoreflectivity and Thermotransmissivity of Polycrystalline and Single-Crystalline Gold-Films”. In: *Physical Review B* 43.5 (1991), pp. 4488–4491. DOI: 10.1103/PhysRevB.43.4488.
- [61] R. W. Schoenlein et al. “Femtosecond Studies of Nonequilibrium Electronic Processes in Metals”. In: *Physical Review Letters* 58.16 (1987), pp. 1680–1683. DOI: 10.1103/PhysRevLett.58.1680.
- [62] G. Baffou, R. Quidant, and C. Girard. “Heat generation in plasmonic nanostructures: Influence of morphology”. In: *Applied Physics Letters* 94.15 (2009), p. 153109. DOI: doi: <http://dx.doi.org/10.1063/1.3116645>.
- [63] M. Hu and G. V. Hartland. “Heat dissipation for Au particles in aqueous solution: Relaxation time versus size”. In: *Journal of Physical Chemistry B* 106.28 (2002), pp. 7029–7033. DOI: 10.1021/jp020581+.
- [64] J. S. Donner et al. “Plasmon-Assisted Optofluidics”. In: *ACS Nano* 5.7 (2011), pp. 5457–5462. DOI: 10.1021/nn200590u.
- [65] M. J. Guffey and N. F. Scherer. “All-Optical Patterning of Au Nanoparticles on Surfaces Using Optical Traps”. In: *Nano Letters* 10.11 (2010), pp. 4302–4308. DOI: 10.1021/nl904167t.

- [66] J. Gargiulo et al. "Accuracy and Mechanistic Details of Optical Printing of Single Au and Ag Nanoparticles". In: *ACS Nano* 11.10 (2017), pp. 9678–9688. DOI: 10.1021/acsnano.7b04136.
- [67] J. Gargiulo et al. "Connecting Metallic Nanoparticles by Optical Printing". In: *Nano Letters* 16.2 (2016), pp. 1224–1229. DOI: 10.1021/acs.nanolett.5b04542.
- [68] J. Gargiulo et al. "Understanding and Reducing Photothermal Forces for the Fabrication of Au Nanoparticle Dimers by Optical Printing". In: *Nano Letters* 17.9 (2017), pp. 5747–5755. DOI: 10.1021/acs.nanolett.7b02713.
- [69] A. S. Urban et al. "Single-Step Injection of Gold Nanoparticles through Phospholipid Membranes". In: *ACS Nano* 5.5 (2011), pp. 3585–3590. DOI: 10.1021/Nn201132a.
- [70] Z. Y. Fang et al. "Evolution of Light-Induced Vapor Generation at a Liquid-Immersed Metallic Nanoparticle". In: *Nano Letters* 13.4 (2013), pp. 1736–1742. DOI: 10.1021/nl4003238.
- [71] P. Urban et al. "Reversible control of current across lipid membranes by local heating". In: *Scientific Reports* 6 (2016), p. 22686. DOI: ARTN2268610.1038/srep22686.
- [72] M. Fedoruk, A. A. Lutich, and J. Feldmann. "Subdiffraction-limited milling by an optically driven single gold nanoparticle". In: *ACS Nano* 5.9 (2011), pp. 7377–82. DOI: 10.1021/nn2023045.
- [73] S. Link, Z. L. Wang, and M. A. El-Sayed. "How does a gold nanorod melt?" In: *Journal of Physical Chemistry B* 104.33 (2000), pp. 7867–7870. DOI: 10.1021/jp0011701.
- [74] C. J. DeSantis et al. "Laser-Induced Spectral Hole-Burning through a Broadband Distribution of Au Nanorods". In: *Journal of Physical Chemistry C* 120.37 (2016), pp. 20518–20524. DOI: 10.1021/acs.jpcc.5b08290.
- [75] S. Link et al. "How long does it take to melt a gold nanorod? A femtosecond pump-probe absorption spectroscopic study". In: *Chemical Physics Letters* 315.1-2 (1999), pp. 12–18. DOI: 10.1016/S0009-2614(99)01214-2.
- [76] K. Koga, T. Ikeshoji, and K. Sugawara. "Size- and temperature-dependent structural transitions in gold nanoparticles". In: *Physical Review Letters* 92.11 (2004). DOI: 10.1103/PhysRevLett.92.115507.
- [77] D. Werner et al. "Femtosecond Laser-Induced Size Reduction of Aqueous Gold Nanoparticles: In Situ and Pump-Probe Spectroscopy Investigations Revealing Coulomb Explosion". In: *The Journal of Physical Chemistry C* 115.17 (2011), pp. 8503–8512. DOI: 10.1021/jp112262u.

- [78] T. Castro et al. “Size-Dependent Melting Temperature of Individual Nanometer-Sized Metallic Clusters”. In: *Physical Review B* 42.13 (1990), pp. 8548–8556. DOI: 10.1103/PhysRevB.42.8548.
- [79] G. Schmid and B. Corain. “Nanoparticulated gold: Syntheses, structures, electronics, and reactivities”. In: *European Journal of Inorganic Chemistry* 17 (2003), pp. 3081–3098. DOI: 10.1002/ejic.200300187.
- [80] A. B. Taylor, A. M. Siddiquee, and J. W. M. Chon. “Below Melting Point Photothermal Reshaping of Single Gold Nanorods Driven by Surface Diffusion”. In: *ACS Nano* 8.12 (2014), pp. 12071–12079. DOI: 10.1021/nn5055283.
- [81] Y. Liu, E. N. Mills, and R. J. Composto. “Tuning optical properties of gold nanorods in polymer films through thermal reshaping”. In: *Journal of Materials Chemistry* 19.18 (2009), pp. 2704–2709. DOI: 10.1039/b901782h.
- [82] S. Karim et al. “Morphological evolution of Au nanowires controlled by Rayleigh instability”. In: *Nanotechnology* 17.24 (2006), p. 5954. DOI: 10.1088/0957-4484/17/24/009.
- [83] H. Oh, J. Lee, and M. Lee. “Transformation of silver nanowires into nanoparticles by Rayleigh instability: comparison between laser irradiation and heat treatment”. In: *Applied Surface Science* (2017). DOI: dx.doi.org/10.1016/j.apsusc.2017.08.102.
- [84] L. Rayleigh. “On The Instability Of Jets”. In: *Proceedings of the London Mathematical Society* s1-10.1 (1878), pp. 4–13. DOI: 10.1112/plms/s1-10.1.4.
- [85] J. A. F. Plateau. *Experimental and Theoretical Statics of Liquids Subject to Molecular Forces only*. Paris: Gauthier-Villars, 1873.
- [86] F. A. Nichols. “On the spheroidization of rod-shaped particles of finite length”. In: *Journal of Materials Science* 11.6 (1976), pp. 1077–1082. DOI: 10.1007/bf02396641.
- [87] A. Walther and A. H. E. Muller. “Janus Particles: Synthesis, Self-Assembly, Physical Properties, and Applications”. In: *Chemical Reviews* 113.7 (2013), pp. 5194–5261. DOI: 10.1021/cr300089t.
- [88] C. Casagrande et al. “Janus Beads - Realization and Behavior at Water Oil Interfaces”. In: *Europhysics Letters* 9.3 (1989), pp. 251–255. DOI: 10.1209/0295-5075/9/3/011.
- [89] R. Golestanian, T. B. Liverpool, and A. Ajdari. “Designing phoretic micro- and nano-swimmers”. In: *New Journal of Physics* 9 (2007). DOI: Artn126PiiS1367-2630(07)41698-610.1088/1367-2630/9/5/126.
- [90] W. Yang et al. “Using self-driven microswimmers for particle separation”. In: *Soft Matter* 8.19 (2012), pp. 5175–5179. DOI: 10.1039/c2sm07382j.

- [91] T. Bickel, A. Majee, and A. Wurger. “Flow pattern in the vicinity of self-propelling hot Janus particles”. In: *Physical Review E* 88.1 (2013). DOI: 10.1103/PhysRevE.88.012301.
- [92] H. R. Jiang, N. Yoshinaga, and M. Sano. “Active Motion of a Janus Particle by Self-Thermophoresis in a Defocused Laser Beam”. In: *Physical Review Letters* 105.26 (2010). DOI: 10.1103/PhysRevLett.105.268302.
- [93] S. Duhr and D. Braun. “Why molecules move along a temperature gradient”. In: *Proceedings of the National Academy of Sciences of the United States of America* 103.52 (2006), pp. 19678–19682. DOI: 10.1073/pnas.0603873103.
- [94] A. Einstein. “Über die von der molekularkinetischen Theorie der Wärme geforderte Bewegung von in ruhenden Flüssigkeiten suspendierten Teilchen”. In: *Annalen der Physik* 322.8 (1905), pp. 549–560. DOI: 10.1002/andp.19053220806.
- [95] J. E. Melzer and E. McLeod. “Fundamental Limits of Optical Tweezer Nanoparticle Manipulation Speeds”. In: *Acs Nano* 12.3 (2018), pp. 2440–2447. DOI: 10.1021/acsnano.7b07914.
- [96] E. E. Michaelides. “Brownian movement and thermophoresis of nanoparticles in liquids”. In: *International Journal of Heat and Mass Transfer* 81 (2015), pp. 179–187. DOI: 10.1016/j.ijheatmasstransfer.2014.10.019.
- [97] F. Zheng. “Thermophoresis of spherical and non-spherical particles: a review of theories and experiments”. In: *Advances in Colloid and Interface Science* 97.1-3 (2002), pp. 255–278. DOI: 10.1016/S0001-8686(01)00067-7.
- [98] B. E. Rapp. “Chapter 9 - Fluids”. In: *Microfluidics: Modelling, Mechanics and Mathematics*. Ed. by B. E. Rapp. Oxford: Elsevier, 2017, pp. 243–263. DOI: 10.1016/B978-1-4557-3141-1.50009-5.
- [99] Paul S. Epstein. “Zur Theorie des Radiometers”. In: *Zeitschrift für Physik* 54.7 (1929), pp. 537–563. DOI: 10.1007/bf01338485.
- [100] M. M. R. Williams. “Thermophoretic Forces Acting on a Spheroid”. In: *Journal of Physics D - Applied Physics* 19.9 (1986), pp. 1631–1642. DOI: 10.1088/0022-3727/19/9/009.
- [101] G. S. McNab and A. Meisen. “Thermophoresis in Liquids”. In: *Journal of Colloid and Interface Science* 44.2 (1973), pp. 339–346. DOI: 10.1016/0021-9797(73)90225-7.
- [102] B. Qian et al. “Harnessing thermal fluctuations for purposeful activities: the manipulation of single micro-swimmers by adaptive photon nudging”. In: *Chemical Science* 4.4 (2013), pp. 1420–1429. DOI: 10.1039/c2sc21263c.
- [103] A. P. Bregulla, H. Yang, and F. Cichos. “Stochastic Localization of Microswimmers by Photon Nudging”. In: *ACS Nano* 8.7 (2014), pp. 6542–6550. DOI: 10.1021/nn501568e.

- [104] E. Ruckenstein. “Can Phoretic Motions Be Treated as Interfacial-Tension Gradient Driven Phenomena?” In: *Journal of Colloid and Interface Science* 83.1 (1981), pp. 77–81. DOI: 10.1016/0021-9797(81)90011-4.
- [105] A. Würger. “Thermal non-equilibrium transport in colloids”. In: *Reports on Progress in Physics* 73.12 (2010). DOI: 10.1088/0034-4885/73/12/126601.
- [106] G. Guthrie, J. N. W., and V. Schomaker. “Theory of the Thermal Diffusion of Electrolytes in a Clusius Column”. In: *The Journal of Chemical Physics* 17.3 (1949), pp. 310–313. DOI: 10.1063/1.1747244.
- [107] C. Sonnichsen et al. “Drastic reduction of plasmon damping in gold nanorods”. In: *Physical Review Letters* 88.7 (2002). DOI: 10.1103/PhysRevLett.88.077402.
- [108] D. J. Griffiths and D. F. Schroeter. *Introduction to Quantum Mechanics*. 3rd ed. Cambridge University Press, 2018. DOI: 10.1017/9781316995433.
- [109] R. F. Egerton. “The Scanning Electron Microscope”. In: *Physical Principles of Electron Microscopy: An Introduction to TEM, SEM, and AEM*. Boston, MA: Springer US, 2005, pp. 125–153. DOI: 10.1007/0-387-26016-1_5.
- [110] B. J. Griffin. “A Comparison of Conventional Everhart-Thornley Style and In-Lens Secondary Electron Detectors-A Further Variable in Scanning Electron Microscopy”. In: *Scanning* 33.3 (2011), pp. 162–173. DOI: 10.1002/sca.20255.
- [111] T. E. Everhart and R. F. M. Thornley. “Wide-Band Detector for Micro-Microampere Low-Energy Electron Currents”. In: *Journal of Scientific Instruments* 37.7 (1960), pp. 246–248. DOI: 10.1088/0950-7671/37/7/307.
- [112] A. G. Cid, R. Rosenkranz, and E. Zschech. “Optimization of the SEM Working Conditions: EsB Detector at Low Voltage”. In: *Advanced Engineering Materials* 18.2 (2016), pp. 185–193. DOI: 10.1002/adem.201500161.
- [113] V. Myroshnychenko et al. “Modelling the optical response of gold nanoparticles”. In: *Chemical Society Reviews* 37.9 (2008), pp. 1792–1805. DOI: 10.1039/b711486a.
- [114] K. S. Yee. “Numerical Solution of Initial Boundary Value Problems Involving Maxwells Equations in Isotropic Media”. In: *IEEE Transactions on Antennas and Propagation* Ap14.3 (1966), pp. 302–307. DOI: 10.1109/TAP.1966.1138693.
- [115] M. Moskovits. “Surface-enhanced Raman spectroscopy: a brief retrospective”. In: *Journal of Raman Spectroscopy* 36.67 (2005), pp. 485–496. DOI: doi:10.1002/jrs.1362.
- [116] Z. L. Horvath and Z. Bor. “Focusing of truncated Gaussian beams”. In: *Optics Communications* 222.1-6 (2003), pp. 51–68. DOI: 10.1016/S0030-4018(03)01562-1.

- [117] H. Kuwata et al. “Resonant light scattering from metal nanoparticles: Practical analysis beyond Rayleigh approximation”. In: *Applied Physics Letters* 83.22 (2003), pp. 4625–4627. DOI: 10.1063/1.1630351.
- [118] P. C. Waterman. “Matrix formulation of electromagnetic scattering”. In: *Proceedings of the IEEE* 53.8 (1965), pp. 805–812. DOI: 10.1109/PROC.1965.4058.
- [119] P. C. Waterman. “Symmetry, Unitarity, and Geometry in Electromagnetic Scattering”. In: *Physical Review D* 3.4 (1971), pp. 825–839. DOI: 10.1103/PhysRevD.3.825.
- [120] M. I. Mishchenko, L. D. Travis, and D. W. Mackowski. “T-matrix computations of light scattering by nonspherical particles: A review”. In: *Journal of Quantitative Spectroscopy & Radiative Transfer* 55.5 (1996), pp. 535–575. DOI: 10.1016/0022-4073(96)00002-7.
- [121] M. I. Mishchenko, L. D. Travis, and D. W. Mackowski. “T-matrix computations of light scattering by nonspherical particles: A review”. In: *Journal of Quantitative Spectroscopy & Radiative Transfer* 55.5 (1996), pp. 535–575. DOI: 10.1016/0022-4073(96)00002-7.
- [122] T. A. Nieminen et al. “Optical tweezers computational toolbox”. In: *Journal of Optics A - Pure and Applied Optics* 9.8 (2007), S196–S203. DOI: 10.1088/1464-4258/9/8/S12.
- [123] T. A. Nieminen, H. Rubinsztein-Dunlop, and N. R. Heckenberg. “Multipole expansion of strongly focussed laser beams”. In: *Journal of Quantitative Spectroscopy & Radiative Transfer* 79 (2003), pp. 1005–1017. DOI: 10.1016/S0022-4073(02)00335-7.
- [124] T. A. Nieminen, H. Rubinsztein-Dunlop, and N. R. Heckenberg. “Calculation of the T-matrix: general considerations and application of the point-matching method”. In: *Journal of Quantitative Spectroscopy & Radiative Transfer* 79 (2003), pp. 1019–1029. DOI: 10.1016/S0022-4073(02)00336-9.
- [125] T. A. Nieminen et al. “Optical tweezers: Theory and modelling”. In: *Journal of Quantitative Spectroscopy & Radiative Transfer* 146 (2014), pp. 59–80. DOI: 10.1016/j.jqsrt.2014.04.003.
- [126] C. H. Choi et al. “Rapid and stable determination of rotation matrices between spherical harmonics by direct recursion”. In: *Journal of Chemical Physics* 111.19 (1999), pp. 8825–8831. DOI: 10.1063/1.480229.
- [127] G. Videen. “Light scattering from a sphere on or near a surface”. In: *Journal of the Optical Society of America A* 8.3 (Mar. 1991), pp. 483–489. DOI: 10.1364/JOSAA.8.000483.
- [128] Advanpix-LLC. *Multiprecision Computing Toolbox for MATLAB 4.4.5.12714* (2016). Computer Program. 2016.
- [129] D. J. Griffiths. *Introduction to electrodynamics; 4th ed.* Re-published by Cambridge University Press in 2017. Boston, MA: Pearson, 2013.

- [130] J. N. Reddy and D. K. Gartling. *The finite element method in heat transfer and fluid dynamics*. CRC press, 2010.
- [131] F. M. Wurm. “Production of recombinant protein therapeutics in cultivated mammalian cells”. In: *Nature Biotechnology* 22.11 (2004), pp. 1393–1398. DOI: 10.1038/nbt1026.
- [132] D. F. Bray, J. Bagu, and P. Koeqler. “Comparison of Hexamethyldisilazane (Hmds), Peldri-Ii, and Critical-Point Drying Methods for Scanning Electron-Microscopy of Biological Specimens”. In: *Microscopy Research and Technique* 26.6 (1993), pp. 489–495. DOI: 10.1002/jemt.1070260603.
- [133] M. Ana. Huergo et al. “Optical Nanoparticle Sorting Elucidates Synthesis of Plasmonic Nanotriangles”. In: *ACS Nano* (2016). DOI: 10.1021/acsnano.5b08095.
- [134] J. E. Park et al. “Golden Opportunities: Plasmonic Gold Nanostructures for Biomedical Applications based on the Second Near-Infrared Window”. In: *Small Methods* 1.3 (2017). DOI: 10.1002/smt.201600032.
- [135] H. S. Zhou et al. “Controlled Synthesis and Quantum-Size Effect in Gold-Coated Nanoparticles”. In: *Physical Review B* 50.16 (1994), pp. 12052–12056. DOI: 10.1103/PhysRevB.50.12052.
- [136] R. D. Averitt, D. Sarkar, and N. J. Halas. “Plasmon resonance shifts of Au-coated Au₂S nanoshells: Insight into multicomponent nanoparticle growth”. In: *Physical Review Letters* 78.22 (1997), pp. 4217–4220. DOI: 10.1103/PhysRevLett.78.4217.
- [137] T. J. Norman et al. “Near Infrared Optical Absorption of Gold Nanoparticle Aggregates”. In: *The Journal of Physical Chemistry B* 106.28 (2002), pp. 7005–7012. DOI: 10.1021/jp0204197.
- [138] A. M. Schwartzberg et al. “Reduction of H₂AuCl₄ by Na₂S revisited: The case for Au nanoparticle aggregates and against Au₂S/Au Core/Shell particles”. In: *The Journal of Physical Chemistry C* 111.25 (2007), pp. 8892–8901. DOI: 10.1021/jp067697g.
- [139] J. J. Diao and H. Chen. “Near infrared surface plasmon resonance of gold tabular nanostructures in the H₂AuCl₄-Na₂S reaction”. In: *The Journal of Chemical Physics* 124.11 (2006), p. 116103. DOI: 10.1063/1.2177661.
- [140] Y. Mikhlin et al. “Formation of gold and gold sulfide nanoparticles and mesoscale intermediate structures in the reactions of aqueous H₂AuCl₄ with sulfide and citrate ions”. In: *Physical Chemistry Chemical Physics* 11.26 (2009), pp. 5445–54. DOI: 10.1039/b823539b.

- [141] G. Zhang et al. “Tunability and stability of gold nanoparticles obtained from chloroauric acid and sodium thiosulfate reaction”. In: *Nanoscale Research Letters* 7.1 (2012), p. 337. DOI: 10.1186/1556-276X-7-337.
- [142] D. Patel et al. “A high yield, one-pot dialysis-based process for self-assembly of near infrared absorbing gold nanoparticles”. In: *Journal of Colloid and Interface Science* 441 (2015), pp. 10–16. DOI: 10.1016/j.jcis.2014.11.029.
- [143] G. Raschke et al. “Gold nanoshells improve single nanoparticle molecular sensors”. In: *Nano Letters* 4.10 (2004), pp. 1853–1857. DOI: 10.1021/nl049038q.
- [144] C. Guillon et al. “Coherent acoustic vibration of metal nanoshells”. In: *Nano Letters* 7.1 (2007), pp. 138–142. DOI: 10.1021/nl06238od.
- [145] A. M. Gobin et al. “Near-Infrared-Resonant Gold/Gold Sulfide Nanoparticles as a Photothermal Cancer Therapeutic Agent”. In: *Small* 6.6 (2010), pp. 745–752. DOI: 10.1002/smll.200901557.
- [146] S. H. Behrens and D. G. Grier. “The charge of glass and silica surfaces”. In: *Journal of Chemical Physics* 115.14 (2001), pp. 6716–6721. DOI: 10.1063/1.1404988.
- [147] M. A. Huergo et al. “New Insight into the Chemical Nature of the Plasmonic Nanostructures Synthesized by the Reduction of Au(III) with Sulfide Species”. In: *Langmuir* 33.27 (2017), pp. 6785–6793. DOI: 10.1021/acs.langmuir.7b01168.
- [148] X. H. Sun et al. “Targeted Cancer Therapy by Immunoconjugated Gold-Gold Sulfide Nanoparticles Using Protein G as a Cofactor”. In: *Annals of Biomedical Engineering* 40.10 (2012), pp. 2131–2139. DOI: 10.1007/s10439-012-0575-7.
- [149] M. Ploschner et al. “Bidirectional Optical Sorting of Gold Nanoparticles”. In: *Nano Letters* 12.4 (2012), pp. 1923–1927. DOI: 10.1021/nl204378r.
- [150] F. Nan and Z. J. Yan. “Sorting Metal Nanoparticles with Dynamic and Tunable Optical Driven Forces”. In: *Nano Letters* 18.7 (2018), pp. 4500–4505. DOI: 10.1021/acs.nanolett.8b01672.
- [151] H. Petrova et al. “On the temperature stability of gold nanorods: comparison between thermal and ultrafast laser-induced heating”. In: *Physical Chemistry Chemical Physics* 8.7 (2006), pp. 814–821. DOI: 10.1039/b514644e.
- [152] F. P. Schmidt et al. “Morphing a Plasmonic Nanodisk into a Nanotriangle”. In: *Nano Letters* 14.8 (2014), pp. 4810–4815. DOI: 10.1021/nl502027r.
- [153] A.-L. Barabási and H. E. Stanley. *Fractal Concepts in Surface Growth*. Apr. 1995, p. 386.

- [154] N. Combe, P. Jensen, and A. Pimpinelli. “Changing shapes in the nanoworld”. In: *Physical Review Letters* 85.1 (2000), pp. 110–113. DOI: 10.1103/PhysRevLett.85.110.
- [155] J. L. Iguain and L. J. Lewis. “Relaxation kinetics in two-dimensional structures”. In: *Physical Review B* 68.19 (2003). DOI: 10.1103/PhysRevB.68.195407.
- [156] D. Punj et al. “A plasmonic ‘antenna-in-box’ platform for enhanced single-molecule analysis at micromolar concentrations”. In: *Nature Nanotechnology* 8.7 (2013), pp. 512–516. DOI: 10.1038/Nnano.2013.98.
- [157] O. L. Muskens et al. “Strong enhancement of the radiative decay rate of emitters by single plasmonic nanoantennas”. In: *Nano Letters* 7.9 (2007), pp. 2871–2875. DOI: 10.1021/nl0715847.
- [158] W. Zhu et al. “Lithographically Fabricated Optical Antennas with Gaps Well Below 10 nm”. In: *Small* 7.13 (2011), pp. 1761–1766. DOI: 10.1002/smll.201100371.
- [159] W. Zhu and K. B. Crozier. “Quantum mechanical limit to plasmonic enhancement as observed by surface-enhanced Raman scattering”. In: *Nature Communications* 5 (2014), p. 5228. DOI: 10.1038/ncomms6228.
- [160] S. Simoncelli et al. “Quantitative Single-Molecule Surface Enhanced Raman Scattering by Optothermal Tuning of DNA Origami-Assembled Plasmonic Nanoantennas”. In: *ACS Nano* 10.11 (2016), pp. 9809–9815. DOI: 10.1021/acsnano.6b05276.
- [161] M. Ringler et al. “Shaping Emission Spectra of Fluorescent Molecules with Single Plasmonic Nanoresonators”. In: *Physical Review Letters* 100.20 (2008), p. 203002. DOI: 10.1103/PhysRevLett.100.203002.
- [162] A. S. Urban et al. “Shrink-to-Fit Plasmonic Nanostructures”. In: *Advanced Optical Materials* 1.2 (2013), pp. 123–127. DOI: 10.1002/adom.201200031.
- [163] A. Bek et al. “Fluorescence enhancement in hot spots of AFM-designed gold nanoparticle sandwiches”. In: *Nano Letters* 8.2 (2008), pp. 485–490. DOI: 10.1021/nl072602n.
- [164] K. J. Savage et al. “From microns to kissing contact: Dynamic positioning of two nano-systems”. In: *Applied Physics Letters* 99.5 (2011), p. 053110. DOI: 10.1063/1.3623437.
- [165] Jorge Zuloaga, Emil Prodan, and Peter Nordlander. “Quantum Description of the Plasmon Resonances of a Nanoparticle Dimer”. In: *Nano Letters* 9.2 (2009), pp. 887–891. DOI: 10.1021/nl803811g.
- [166] J. A. Scholl et al. “Observation of Quantum Tunneling between Two Plasmonic Nanoparticles”. In: *Nano Letters* 13.2 (2013), pp. 564–569. DOI: 10.1021/nl304078v.

- [167] S. Kadkhodazadeh et al. “Coexistence of classical and quantum plasmonics in large plasmonic structures with subnanometer gaps”. In: *Applied Physics Letters* 103.8 (2013), p. 083103. DOI: 10.1063/1.4819163.
- [168] J. Mertens et al. “Controlling Subnanometer Gaps in Plasmonic Dimers Using Graphene”. In: *Nano Letters* 13.11 (2013), pp. 5033–5038. DOI: 10.1021/nl4018463.
- [169] B. de Nijs et al. “Plasmonic tunnel junctions for single-molecule redox chemistry”. In: *Nature Communications* 8 (2017). DOI: 10.1038/s41467-017-00819-7.
- [170] K. Kneipp et al. “Surface-enhanced Raman Spectroscopy in single living cells using gold nanoparticles”. In: *Applied Spectroscopy* 56.2 (2002), pp. 150–154. DOI: 10.1366/0003702021954557.
- [171] M. B. Mohamed et al. “The ‘lightning’ gold nanorods: fluorescence enhancement of over a million compared to the gold metal”. In: *Chemical Physics Letters* 317.6 (2000), pp. 517–523. DOI: 10.1016/S0009-2614(99)01414-1.
- [172] E. Cortes et al. “Plasmonic hot electron transport drives nano-localized chemistry”. In: *Nature Communications* 8 (2017). DOI: 10.1038/ncomms14880.
- [173] N. R. Jana, L. Gearheart, and C. J. Murphy. “Wet Chemical Synthesis of High Aspect Ratio Cylindrical Gold Nanorods”. In: *The Journal of Physical Chemistry B* 105.19 (2001), pp. 4065–4067. DOI: 10.1021/jp0107964.
- [174] J. W. Liaw, Y. S. Chen, and M. K. Kuo. “Maxwell stress induced optical torque upon gold prolate nanospheroid”. In: *Applied Physics A: Materials Science & Processing* 122.3 (2016). DOI: 10.1007/s00339-016-9732-4.
- [175] C. M. Maier et al. “Optical and Thermophoretic Control of Janus Nanoparticle Injection into Living Cells”. In: *Nano Letters* 18.12 (2018), pp. 7935–7941. DOI: 10.1021/acs.nanolett.8b03885.
- [176] R. Shukla et al. “Biocompatibility of gold nanoparticles and their endocytotic fate inside the cellular compartment: A microscopic overview”. In: *Langmuir* 21.23 (2005), pp. 10644–10654. DOI: 10.1021/la0513712.
- [177] N. S. Abadeer and C. J. Murphy. “Recent Progress in Cancer Thermal Therapy Using Gold Nanoparticles”. In: *Journal of Physical Chemistry C* 120.9 (2016), pp. 4691–4716. DOI: 10.1021/acs.jpcc.5b11232.
- [178] J. Stehr et al. “Gold NanoStoves for microsecond DNA melting analysis”. In: *Nano Letters* 8.2 (2008), pp. 619–623. DOI: 10.1021/nl073028i.
- [179] S. W. Zeng et al. “A Review on Functionalized Gold Nanoparticles for Biosensing Applications”. In: *Plasmonics* 6.3 (2011), pp. 491–506. DOI: 10.1007/s11468-011-9228-1.

- [180] P. Ghosh et al. “Gold nanoparticles in delivery applications”. In: *Advanced Drug Delivery Reviews* 60.11 (2008), pp. 1307–1315. DOI: 10.1016/j.addr.2008.03.016.
- [181] A. S. Urban et al. “Controlled nanometric phase transitions of phospholipid membranes by plasmonic heating of single gold nanoparticles”. In: *Nano Letters* 9.8 (2009), pp. 2903–8. DOI: 10.1021/nl901201h.
- [182] M. Delcea et al. “Nanoplasmonics for Dual-Molecule Release through Nanopores in the Membrane of Red Blood Cells”. In: *ACS Nano* 6.5 (2012), pp. 4169–4180. DOI: 10.1021/nn3006619.
- [183] C. McDougall et al. “Targeted optical injection of gold nanoparticles into single mammalian cells”. In: *Journal of Biophotonics* 2.12 (2009), pp. 736–743. DOI: 10.1002/jbio.200910030.
- [184] W. Tao et al. “Direct Gene-Transfer into Human Cultured-Cells Facilitated by Laser Micropuncture of the Cell-Membrane”. In: *Proceedings of the National Academy of Sciences of the United States of America* 84.12 (1987), pp. 4180–4184. DOI: 10.1073/pnas.84.12.4180.
- [185] M. Tsukakoshi et al. “A Novel Method of DNA Transfection by Laser Microbeam Cell Surgery”. In: *Applied Physics B - Photophysics and Laser Chemistry* 35.3 (1984), pp. 135–140. DOI: 10.1007/Bf00697702.
- [186] M. T. Carlson, A. J. Green, and H. H. Richardson. “Superheating Water by CW Excitation of Gold Nanodots”. In: *Nano Letters* 12.3 (2012), pp. 1534–1537. DOI: 10.1021/nl2043503.
- [187] J. Marmur and P. Doty. “Determination of Base Composition of Deoxyribonucleic Acid from its Thermal Denaturation Temperature”. In: *Journal of Molecular Biology* 5.1 (1962), pp. 109–118. DOI: 10.1016/S0022-2836(62)80066-7.
- [188] G. N. Somero. “Proteins and Temperature”. In: *Annual Review of Physiology* 57 (1995), pp. 43–68. DOI: 10.1146/annurev.ph.57.030195.000355.
- [189] A. G. Mark et al. “Hybrid nanocolloids with programmed three-dimensional shape and material composition”. In: *Nature Materials* 12.9 (2013), pp. 802–807. DOI: 10.1038/Nmat3685.
- [190] J. P. Spatz et al. “Ordered deposition of inorganic clusters from micellar block copolymer films”. In: *Langmuir* 16.2 (2000), pp. 407–415. DOI: 10.1021/la990070n.
- [191] T. Lohmueller, E. Bock, and J. P. Spatz. “Synthesis of quasi-hexagonal ordered arrays of metallic nanoparticles with tuneable particle size”. In: *Advanced Materials* 20.12 (2008), pp. 2297–2302. DOI: 10.1002/adma.200702635.

- [192] R. Boidin et al. “Pulsed laser deposited alumina thin films”. In: *Ceramics International* 42.1 (2016), pp. 1177–1182. DOI: 10.1016/j.ceramint.2015.09.048.
- [193] W. P. Wong and K. Halvorsen. “The effect of integration time on fluctuation measurements: calibrating an optical trap in the presence of motion blur”. In: *Optics Express* 14.25 (2006), pp. 12517–12531. DOI: 10.1364/Oe.14.012517.
- [194] Y. Seol, A. E. Carpenter, and T. T. Perkins. “Gold nanoparticles: enhanced optical trapping and sensitivity coupled with significant heating”. In: *Optics Letters* 31.16 (2006), pp. 2429–2431. DOI: 10.1364/Ol.31.002429.
- [195] G. E. Uhlenbeck and L. S. Ornstein. “On the theory of the Brownian motion”. In: *Physical Review* 36.5 (1930), pp. 0823–0841. DOI: 10.1103/PhysRev.36.823.
- [196] S. M. Lee, D. G. Cahill, and T. H. Allen. “Thermal-Conductivity of Sputtered Oxide-Films”. In: *Physical Review B* 52.1 (1995), pp. 253–257. DOI: 10.1103/PhysRevB.52.253.
- [197] M. Speidel, A. Jonas, and E. L. Florin. “Three-dimensional tracking of fluorescent nanoparticles with subnanometer precision by use of off-focus imaging”. In: *Optics Letters* 28.2 (2003), pp. 69–71. DOI: 10.1364/Ol.28.000069.
- [198] T. Calais et al. “Role of Alumina Coatings for Selective and Controlled Bonding of DNA on Technologically Relevant Oxide Surfaces”. In: *Journal of Physical Chemistry C* 119.41 (2015), pp. 23527–23543. DOI: 10.1021/acs.jpcc.5b06820.
- [199] K. Lubyphelps, D. L. Taylor, and F. Lanni. “Probing the Structure of Cytoplasm”. In: *Journal of Cell Biology* 102.6 (1986), pp. 2015–2022. DOI: 10.1083/jcb.102.6.2015.
- [200] G. B. Yao et al. “Clicking DNA to gold nanoparticles: poly-adenine-mediated formation of monovalent DNA-gold nanoparticle conjugates with nearly quantitative yield”. In: *NPG Asia Materials* 7 (2015). DOI: 10.1038/am.2014.131.

Acknowledgments

A total of 5.5 years (including my master thesis in the same group) is a long time to look back. It was a time of many ups and downs, but I will remember it as a very positive span of my life where I learned a lot for science but also for life. All of that would not have been possible without the people surrounding me during all those years, to whom I want to say Thank You!

First and foremost, my thank goes to PD Dr. **Theobald Lohmüller**, my "Doktorvater". Being full of ideas and having an incredibly broad scope of knowledge he always challenged me to try out new things and not be satisfied with what was already obtained too quickly, thus bringing the level of my projects and in the end my thesis to new heights. I will always remember our fun (and sometimes also heated) but fruitful discussions in his office. He taught me a lot about scientific writing and presenting and together we always found a solution for the challenges I had.

Furthermore, I want to thank Prof. Dr. **Jochen Feldmann** for receiving me in his Photonics and Optoelectronics group as a PhD student. The challenges and the high level of discussions made me grow as a person as well as a scientist.

I appreciate the scientific contributions of Dr. **Ana Huergo**, for being a coauthor in three of my publications, Prof. Dr. **Alexander Urban** for his coauthorship in my first publication and my "mentor" Dr. **Michael Fedoruk** for his constant advise during and even after his and my time at the chair.

I am thankful for the administrative and emotional support from **Gerlinde Adam**. You play a big role for all us PhD students! Thank you also **Stefan Niedermaier**, **Katja Lyons** and **Talee Barghouti** for your helpful attitude and technical support during my time at the chair.

A very particular thank goes to my former Bachelor and Master students. I was blessed with very talented and motivated students, namely **Sara Milosevic**, **Wolf Knöller** and **Maximilian Maier** for Bachelor thesis and **Jakob Lenz**, **Felix Winterer**, **Christian Mühlbauer** and **Francis Schuknecht** for Master thesis. Working with you has both helped the advancement of my thesis as well as my personal development greatly. It was a really great experience to work with you!

I also want to thank all my hard-working proof readers Dr. **Verena Hintermayr**, **Felix Winterer**, Dr. **Aurora Manzi**, Dr. **Carla Pernpeintner**, **Patrick Urban**, Dr. **Bernhard Bohn**, **Stefanie Pritzl** and **Sara Milosevic**. Your work was really essential for finishing up this thesis.

A big thank you goes to the great colleagues I was blessed with at the PhOG. I was able to make many really good friends during my time at this chair. In particular I would like to mention Dr. **Verena Hintermayr**, **Felix Winterer**, Dr. **Aurora Manzi**, Dr. **Carla Pernpeintner**, **Florian Ehrat**, **Patrick Urban**, Dr. **Bernhard Bohn**, **Stefanie Pritzl**, **Alexander Richter**, Dr.

Ana Huergo, Sara Milosevic and Dr. **Adam Blanch**. Working together with good friends made the sometimes difficult times a lot better. I would also like to say thank you to my former office mates, among them Dr. **Jasmina Sichert**, Dr. **Anastasia Babynina**, Dr. **Miao Li**, Dr. **Yu Tong** and **Moritz Gramlich** as well as to the members of the former and current PhoG generation I still had the chance to get to know to, Dr. **Jackwon Do**, **Verena Baumann**, Dr. **Paul Kühler**, Dr. **Silke Kirchner**, **Nicola Kerschbaumer** **Simone Strohmaier** and **Sebastian Rieger** among others. You made it a really tough day for me when I left the chair!

Last but not least I would like to say thank you to my family and friends. In the first place I want to thank my two kids, **Rafaela** and **David**, whom I had the chance to see growing up in the first years of their lives during my time as a PhD student. Watching you grow up made up for many setbacks I had to experience scientifically. Another very big thank you goes to my wife, **Geovanna** for all her love and emotional support to sustain all the challenges I had to experience elsewhere. Moreover, I want to thank my parents **Anton** and **Anna Maria** as well as by brother **Tobias** and my sister **Verena** for always being supportive and great role models in so many aspects of life. Lastly, I also want to thank my closest friends from the "**Suppe**" for the great time we had together since our childhood up to this very day.